CR-137684

THE DEVELOPMENT OF EXPERIMENTAL TECHNIQUES FOR THE STUDY OF HELICOPTER ROTOR NOISE

Professor Sheila E. Widnall
Professor Wesley L. Harris

Ying-Chieh Albert Lee
and
Herman M. Drees

Massachusetts Institute of Technology
Department of Aeronautics and Astronautics
Fluid Dynamics Research Laboratory
Cambridge, Massachusetts 02139

Final Report

NAS2-7684

June 1973 to November 1974

AAMRDL/NASA Ames

Moffett Field, California

ABSTRACT

The theories, experiments and issues on helicopter rotor noise are reviewed. The features of 12 existing wind tunnels involved in noise studies are discussed. The acoustic characteristics of the MIT low noise open jet wind tunnel have been obtained by employing two different calibration techniques. One technique is to measure the decay of sound pressure with distance in the far field. The other technique is to utilize a speaker, which was calibrated, as a sound source. The sound pressure level (SPL) versus frequency was obtained in the wind tunnel chamber and compared with the corresponding calibrated values. The results of two different techniques agree with each other. Fiberglas board-block units were installed on the chamber interior. The free field was increased significantly after this treatment and the chamber cut-off frequency was reduced to 160 Hz from the original designed 250 Hz. The flow field characteristics of the rotor-tunnel configuration were studied by using flow visualization techniques. The influence of open-jet shear layer on the sound transmission were studied by using an Aeolian tone as the sound source. This influence is negligible in our tunnel operation range. A dynamometer system which was designed to measure the steady and low harmonics of the rotor thrust was developed. A theoretical Mach number scaling formula was developed which can be used to scale the rotational noise and blade slap noise data of model rotors to full scale helicopter rotors.

ACKNOWLEDGEMENTS

The authors wish to express their appreciation to Professors Richard Lyon, Norman Ham and Patrick Leehey for their valuable suggestions and help during the course of this effort.

Thanks are due Messrs. Allan Shaw, Fred Merlis and J. Macksteiner for technical advice and outstanding craftsmanship. The authors also thank Ms. Anne Clee for her skillful typing.

The work reported here was sponsored by the U. S. Army Air Mobility Research & Development Laboratory (AAMRDL), Ames Directorate under AAMRDL/NASA Contract NAS2-7684.

I. INTRODUCTION

Inherent in the operation of VTOL systems is the generation of noise due to unsteady aerodynamic events which occur as an unwanted consequence of the product lift and thrust. There have been many studies of helicopter noise and quieter vehicles have actually been built, but it is fair to say that the principle noise reduction technique is to reduce the rotor tip speed. One's ability to develop purely theoretical methods of noise prediction and control is hampered by a lack of theoretical methods for the prediction of unsteady aerodynamic forces on rotors -- especially for those aerodynamic phenomena which are particularly important for noise generation such as unsteady blade-vortex interaction.

While aerodynamic developments to predict the higher harmonic content of these unsteady aerodynamic forces on the blades may yet be fruitful, at this time, it would not be profitable to attempt a purely theoretical analysis to predict VTOL noise. Existing noise prediction methods can be classed as semi-empirical. On the other hand, our ability to understand, predict and control VTOL noise has been hampered by lack of experimental data on the aerodynamics and noise generation of a VTOL rotor in forward flight -- until now, this data was available largely from flight tests. [1]

---

[1] Some acoustic data has been obtained in the hard-walled 40' x 80' tunnel at Ames Research Center but due to tunnel noise and wall reflection, it is difficult to interpret. (See for example, Ref. 1) It is, however, useful to assess the effect of design changes.

Because of this situation, we began in 1969 to modify an existing conventional low-speed wind tunnel at MIT to develop a V/STOL noise facility consisting of an open jet tunnel operating within an anechoic chamber. This facility began full operation in December, 1971, and has already been successfully used in several aerodynamic noise studies. Beginning in June, 1973, under the support of AAMRDL/NASA Contract NAS2-7684, further development and calibration have been done to ensure accurate reproduction simultaneously of the essential features of both the aerodynamics and acoustics of VTOL systems. A dynamometer system has been developed to measure the steady thrust and some low harmonics of it for the model rotor system. A Mach number scaling formula has been derived for scaling the model rotor data to the real helicopter rotor situation.

II. STATE OF THE ART

i) A Review of Helicopter Noise -- Theory, Experiments and Issues

Aerodynamic noise from main rotors is usually grouped into three classifications: rotational noise, vortex noise, and blade slap.[2,3] Rotational noise can be defined as the noise a main rotor would produce in an inviscid fluid, including all harmonic orders of unsteady potential flow airloads. Vortex noise is often considered to be the additional noise radiated due to the turbulent flow on the blade sections and in the rotor plane (boundary-layer separation, vortex shedding and the operation of airfoils in a turbulent wake). A more precise definition would identify vortex noise as due to random vortex shedding from the airfoils and use the more general term broadband noise to describe noise due to operation in a turbulent inflow. We make this distinction here for reasons that will

become apparent. Blade slap is a characteristic impulsive sound which is produced when strong interaction occurs between a blade and a trailing vortex or when a blade tip experiences strong compressibility effects. Obviously, there is a smooth transition from rotational noise into the blade-slap condition, but the distinction is usually made. When blade slap occurs, it dominates all other noise sources.

There are several theoretical and experimental efforts[4-9] to model and predict the blade-slap phenomena which can be isolated as due to blade vortex interaction or due to compressibility effects on the advancing blade. In addition, several detailed experimental studies of the causes of vortex noise on fixed airfoil sections have been reported.[10-12]

Theoretical studies of rotor noise[13-17] begin by identifying the primary cause of noise as the unsteady lift (and drag) fluctuations which act over the rotor disk. The purely theoretical approach breaks down for we do not know the unsteady lift fluctuations nor do we yet have any hope of being able to predict them in the frequency range of interest for helicopter noise, typically above the 30th harmonic of the blade passage frequency. At this point, most helicopter noise theories employ existing experimental data to develop a semi-empirical prediction scheme. The development of semi-empirical prediction methods to predict noise as a function of thrust, number of blades, advance ratio, solidity, tilt angle of the rotor disk and other parameters is hampered by our lack of experimental data over a wide range of rotor geometry and operating conditions and our lack of understanding about the aerodynamic details of the noise generation mechanisms.

The most complete data on rotor noise is currently obtained from whirl tower tests which, of course, do not simulate high speed forward flight.

Up to this time, the experimental data about the effect of forward speed upon rotor noise on which current noise prediction methods are based is obtained largely from flight tests. The difficulties in obtaining valid noise data from flight tests which would add to our basic understanding of rotor noise mechanisms are considerable. For example, background noise, acoustic transmission, absorption and reflection characteristics of the test sight, and wind gusts make meaningful acoustic data difficult to obtain. In addition, it is difficult to measure the aerodynamic events on the vehicle simultaneously with the noise they radiate. The time varying character of the signal in a fly-over makes interpretation of the signal difficult. Directivity information is seldom obtained. Even if meaningful acoustic data on a known vehicle configuration and operating condition could be obtained, the constraints of flight tests make the variation of parameters over a wide range impossible. The range of RPM's over which the main rotor can be tested is very limited. It is not possible to turn off either the tail rotor or the engine to assess their effect separately and maintain a simulation of powered flight. The expense of flight tests reduces our ability to make design changes and determine their effect on system performance and radiated noise. If this situation existed in the design and operation of flight vehicles, it would be analogous to being unable to measure the aerodynamic characteristics of a vehicle until after it was built and flown; the effect of all design modification would be studied directly by flight tests on the full scale vehicle.

To obtain an understanding of the basic mechanisms of noise from V/STOL configurations, simultaneous aerodynamic and acoustic measurements in a controlled environment are essential. One obvious solution to these

problems is proper simulation of the vehicle and the important aerodynamic and acoustic interactions in a wind tunnel. Wind tunnel testing for performance and aerodynamic characteristics is a valuable and standard technique in aircraft design. Wind tunnel simulation and proper measurement of acoustic phenomena resulting from unsteady aerodynamic interaction is a more recent development.

A question which has been repeatedly discussed at technical meetings on helicopter noise and in the literature[18] is the relative contributions of vortex and rotational noise to the total noise of the rotor system in forward flight. While this question can easily be answered with proper experiments and data reduction techniques, it cannot easily be investigated using flight test measurements due to the non-stationarity of the acoustic signal from the helicopter as the vehicle flies past the microphone. Whirl towers give no information about this question since they cannot simulate forward flight. Such questions indicate a need for data from well-controlled experiments on which to base theoretical models.

Under a previous ARO program, we ran a preliminary set of experiments on rotational noise to explore these questions as well as to define the experimental techniques and to gain experience with the new model rotor system. The results of this preliminary set of experiments were presented in a paper, "Experimental Studies of Rotational Noise in Forward Flight," at the AHS Mid-East Symposium,[21] Essington, Pennsylvania, October, 1972, and communicated in an oral presentation at the Acoustical Society Meeting[26] in Miami, Florida, December, 1972.

In these experiments, we were able to extract the repeated transient waveform from the total signal. In addition, several interesting features of the broadband noise were observed as will be discussed below.

In that experiment, we used two blades on our model rotor with the

angle of attack equal to 5° (at the tip). The rotor shaft was vertical or tilted forward, and the blades were free to flap. Runs were made in hover, and at tunnel speeds of 15, 30 and 40 mph. Spectra of the acoustic signal were taken for both the total signal and the repeated transient signal (rotational noise). The time waveform of these two signals were photographed on an oscilloscope.

Several separate noise mechanisms were identified in that experimental investigation:

1. Low harmonic unsteady loading
2. High harmonic rotational noise due to blade-vortex interaction
3. Vortex noise
4. Broadband noise

The experimental results that we obtained in the hover condition demonstrated the difficulty of obtaining valid noise data in hover as contrasted with forward flight where we were able to obtain meaningful (repeatable, understandable) data. It is well known that the aerodynamic flow field of a rotor in hover is difficult to predict analytically and that, in this condition, the rotor wake is very unsteady and actually unstable.[19]

For the rotor in hover, a high broadband noise content would be expected due to turbulence and unsteadiness in the wake. Also, in the experimental situation, high broadband noise would be caused by reingestion due to the proximity of the floor and walls of the test section. This high level of broadband noise was clearly visible in all of the hover spectra. With forward speed, the level dropped significantly.

For the rotor in forward flight, one of the most striking features of the transient signals was the repeated occurrence of an impulsive noise, most likely due to blade-vortex interaction. Whenever a strong impulsive signature was obtained, the higher harmonic content of the total signal was determined by the higher harmonic content of the rotational noise spectrum. In these cases, the reduction of helicopter noise requires an understanding, modeling and control of the discrete unsteady aerodynamic interactions which, as indicated by the transient signal, occur at various azimuth locations around the rotor disk. In other cases, the broadband noise determined the levels in this range of frequencies.

In general, our results showed that with increasing tilt of the rotor disk, the higher-harmonic content of the rotational noise spectrum decreased, most likely due to the fact that there is less interaction between the blades and the vortex wake as the disk is tilted forward.

The rotational noise at the low harmonics of the blade-passage frequency was the same for both total and averaged signal indicating strong repeatability of the signal from each blade passage in forward flight as contrasted to hover. As would be expected, the level of the low harmonics increased with increasing forward speed due to an increasing asymmetry and unsteadiness in loading.

A distinctive feature of the broadband noise (we call it vortex noise) was the peak due to laminar vortex shedding near the blade tip (with perhaps some complications due to the three-dimensional nature of the flow near the tip). This peak increased, not entirely monotonically, with increasing forward speed and shifted slightly to higher frequencies.

The details of the unsteady aerodynamic mechanisms of the observed broadband noise generation in forward flight at somewhat lower frequencies are not completely understood. An examination of the total time waveform of the acoustic signals revealed "bursts" of broadband fluctuations which repeat at the same location of each blade passage. This may be due to local stall caused by a rapid change of inflow conditions with azimuth, or to stall on the retreating-blade side. With increasing tilt of the rotor disk forward, the mid-range broadband noise decreases somewhat although the effect is not as pronounced as for the rotational noise. Again, the cause is likely to be less interaction of the blades with the unsteady wake. The "vortex" noise peak is not significantly affected by rotor disk tilt.

Although the results of this study raise many questions that cannot be answered presently, we believe that these preliminary results demonstrate the utility of the experimental techniques to interpret and diagnose many of the aerodynamic mechanisms responsible for rotor noise.

ii) Review of Some Existing Facilities for Noise Studies

There exists several wind tunnel facilities which can be exploited in noise studies. Some are designed specifically for noise study, others are converted from conventional tunnels, and others are only conventional tunnels. The top speed, size, background noise and cut-off frequency are all different. A brief review on these facilities is outlined as follows:

(1) MIT Acoustics and Vibration Laboratory Anechoic Wind Tunnel

The facility is designed specifically for acoustic studies. It has an open circuit with an open/closed test section. The upstream settling chamber has a honeycomb section and several sets of screens. The test section

is 15" x 15" in dimension. The turbulence level in the test section is low. The top speed is 180 fps. The SPL of background noise is less than 85 db at frequencies above 200 Hz with 150 fps wind speed. The cut-off frequency is about 500 Hz.

(2) NSRDC Anechoic Wind Tunnel

This test facility is designed for experiments on noise. The test section is 8' x 8'. It has a closed circuit with an open test section. The test section is enclosed within an anechoic chamber. It can also be operated in a closed test section made with the walls acoustically treated. The maximum speed is 200 fps. The background noise SPL (1 Hz bandwidth) is less than 62 db below about 400 Hz and less than 35 db at 10 KHz at 200 fps top speed.

(3) BBN Anechoic Wind Tunnels

There are two acoustic wind tunnels at Bolt Beranek and Newman Inc. (BBN).

a) High speed wind tunnel

There are two nozzles available for this open-jet tunnel; 4' x 4' nozzle and 28" x 40" nozzle. The top speed of the free jet for the large and the small nozzle is 140 fps and 240 fps, respectively. It may operate in a closed loop or open in return flow path. The length of the test section is 30 feet. The overall SPL of background noise is 80 db at 140 fps for large jet and over 90 db at 240 fps for small jet. Interchangeable acoustic modes (anechoic or reverberant) are available. The walls and floor of the anechoic chamber are covered with 2 inch foam with cavities on the back. The cut-off frequency of this facility is under investigation presently.

b) Low speed wind tunnel

There are two open test sections available; a 16" x 16" cross section and 18 inch diameter round section. It has an open circuit with a 120 fps top speed. This facility has an acoustically treated inlet and outlet and a plywood chamber with cotton batting. The chamber cut-off frequency is 180 Hz.

(4) United Aircraft Acoustic Research Tunnel

Two open test sections are available; one with a circular nozzle -- exit area 10 $ft.^2$ and 9 to 1 contraction ratio, the other one with square nozzle -- exit area 4.5 $ft.^2$ and 17 to 1 contraction ratio. The tunnel is of the open circuit type with a honeycomb section and several screens with vortex generators fitted around the nozzle periphery. The top speed is 690 fps. The chamber cut-off frequency is 250 Hz.

(5) MIT Department of Aeronautics and Astronautics Wind Tunnel

This wind tunnel is of the closed return type and originally had 5' x 7 1/2' test section. It was converted to operate as an open-jet tunnel.[20] The test section is enclosed within a vibration-isolated anechoic chamber. Fiberglas wedges have been installed at the two vertical walls of turning and return sections. The turning vanes were also acoustically treated. Further development on this facility will be discussed in the next section.

(6) Pennsylvania State Department of Aerospace Engineering Tunnel

It is of the closed circuit type. The test section can be changed from open type to closed type or vice-versa. The top speed is 150 fps. The 4' x 5' test section is enclosed in an anechoic chamber. The endwalls are acoustically treated.

(7) RAE Low-Speed Wind Tunnel (England)

This facility has an open-jet test section with circular nozzle of 24 feet diameter which has spoilers fitted around its periphery. It is of closed return circuit type and 165 fps is the top speed. The test section is enclosed in an acoustically treated chamber. The background noise is between 105 db and 80 db at frequency below 600 Hz at 120 fps. The chamber cut-off frequency is 2 Khz.

(8) DFVLR Subsonic Wind Tunnel (Germany)

This tunnel has an open-jet test section with a rectangular nozzle of area 75 ft.^{2} It is of the closed circuit type and 260 fps is the top speed. The first diffuser and corner (upstream of the fan) are acoustically treated and are also fitted with a sound-absorbing splitter. The background noise SPL is 100 dbA at 260 fps.

(9) AAMRDL (Ames) Wind Tunnel

It is of the closed circuit type. The open test section is 7' x 10'. All walls, except the far wall of the anechoic chamber, are covered with Scot felt 10' x 3' x 2' panels which are made of high density foam. No acoustic calibration has been done at present. In recent blade-slap studies, it was observed that the first reflection from the wall occurred at about 10 db lower than the incidence waves. It is believed that the anechoic treatment absorbs most of the high frequency components of the incidence sound. This facility is adequate for blade-slap study.

(10) NASA Langley Wind Tunnel

This tunnel is not in full operation at present. The full calibrations are expected to be finished in 5 to 6 months. It has a closed circuit

with an open test section. There are two vertical open jet test sections available: a 4 ft. diameter round jet with a 125 fps top speed and a 1' x 2' rectangular cross section jet with a top speed of 210 fps. The horizontal test section is also available. The length of test section is 35 feet. The acoustic treatment of the anechoic chamber around the test section consists of 3 foot wedges. The cut-off frequency of the anechoically-treated test section is designed to be 100 Hz. The actual value is not yet determined.

(11) NASA Ames 40' x 80' Wind Tunnel

This is the world's largest subsonic wind tunnel. It is of the closed circuit type and it has a closed test section with a 340 fps top speed. This facility is acoustically untreated and requires correction for reverberation effects. The background noise SPL at 170 fps is less than 100 db at frequencies above 300 Hz.

(12) ONERA Large Subsonic/Sonic Wind Tunnel (France)

This tunnel has a closed circular test section of 26 feet diameter and a closed return section. The maximum wind speed is 1.02 Mach number. The background noise inside the settling chamber of 80 inches diameter is 100 db, at low frequencies falling to 80 db at 2 KHz at a test section speed of about 330 fps.

The facilities (11) and (12) are mainly for aerodynamic studies, but some noise studies have been conducted in these facilities. The reverberation effects are severe in most cases. Some corrections are usually necessary.

III. Determination of the Acoustic and Flow Characteristics of the FDL, MIT Wind Tunnel

A photograph of the model rotor in the open-jet test section is shown in Fig. 1. The dimensions of the test section are 5' x 7 1/2'; the top speed is 75 mph. The open-jet test section runs through an anechoic chamber of dimensions 24' x 12' x 12'. Modifications to the tunnel include mufflers to quiet the tunnel fan in the frequency range of interest.[20] The background noise in the test section measured with the tunnel running at top speed at several stages during the modification is shown in Fig. 2. The lowest curve, obtained with additional fiberglas block treatment in the anechoic chamber, is the present background noise.

For studies of aerodynamic noise, there are several advantages to a large open jet operating within an anechoic chamber as compared with a conventional hard-walled wind tunnel. Noise measurements can be made in the low-velocity region beyond the jet which reduces the problem of microphone "self-generated" wind noise. The absence of wall reflection in the anechoic environment makes possible detailed studies of the directivity of the sound field. This, combined with the ability to simulate the aerodynamics of the rotor in forward flight, makes it possible to obtain the directivity of rotor noise as a function of flight conditions.

There are also several disadvantages to an open-jet tunnel. Although, on balance, we believe that these effects are not a problem in our facility, this would have to be verified in the course of the current development. The presence of the turbulent shear layer at the edge of the jet can give rise to several problems. One is basic instability of the tunnel flow itself; in our tunnel, the jet was stabilized by means of a slotted cowl. The exact

suppression mechanism and the local flow pattern around the cowl were under investigation in the current program. Another problem is that the floor of the background noise is set by noise radiated from the free-jet shear layer; at our tunnel Mach numbers, this noise floor should be quite low. The presence of turbulence and non-uniform flow near the jet boundary will scatter and refract the sound field from a source in the free stream. This effect has been studied by using an Aeolian tone as the sound source.

i) Acoustic Measurements

The acoustic characteristics of the anechoic chamber of the FDL, MIT low noise open jet wind tunnel have been obtained. Two different techniques of calibration were employed and the results were compared.

The first technique is to measure the decay of sound pressure with distance in far field. If the free field conditions are obtained, the level of acoustic field decays 6 db per doubling distance. Any reflections from surfaces would be shown up as departures from "free field".

Both white noise and pulsed signals were used in utilizing the omni-directional speaker. The white noise source was used to measure the decay of the sound field in narrow frequency bands in all directions away from the source. The pulsed signals were used to identify any reflecting surfaces by means of time-until-any-return-pulse measurements. The comparison of the results of the white noise testing with the results of the pulsed signal testing can be used to substantiate each other. Of particular interest are reflections from interior tunnel walls since these are more difficult to treat. The speaker was mounted at five different locations; one at the rotor shaft tip and the other four at the end of the blade tip of our model rotor with the rotor blade at 0°, 90°, 180°, 270° azimuth positions measured

from aft of the centerline in the tunnel. The microphone was mounted at a sufficient number of locations to adequately map out the acoustical properties of the open tunnel. The test configuration and instrumentation set-up are shown in Fig. 3 and 4. Some typical results of the white noise testing are shown in Figs. 5 and 9. The abscissa h is the distance between the speaker and microphone. Some typical pulse-testing results are shown in Fig. 10. The horizontal scale is time axis, each grid represents 2 milliseconds. The vertical scale is the voltage axis. The lower trace is the pulse input to the speaker and the upper trace is the signal received by the microphone. The first spike is the incoming pulse signal. The time taken by the reflected signal to reach the microphone can be calculated and marked, as an arrow under each picture.

The other technique for calibrating the chamber of the wind tunnel was to utilize the speaker, which was calibrated in another anechoic chamber with known characteristics, as a sound source. The sound pressure versus frequency as then obtained in the wind tunnel chamber and compared with the corresponding calibrated values at chosen azimuths, elevations and distances. The anechoic chamber in the Department of Electrical Engineering, MIT, was used as a reference for this test. All surfaces of that anechoic chamber are treated with acoustic fiberglas wedges with a depth of approximately three feet. A wire mesh suspension was provided for access to the chamber, permitting the floor to be similarly treated. The background noise of that chamber was observed to be extremely low. The measure noise total SPL was 48 db. The highest SPL in the noise spectrum was 43 db at about 25 Hz.

The acoustic characteristics of the Department of Electrical Engineering, MIT, (EE) anechoic chamber were obtained by the white noise

testing technique. The results are shown in Fig. 11. At distances greater than 2 ft. from the edge of the fiberglas wedge, the acoustic data are seen to be reverberation-free. The microphone was mounted at various positions along a line normal to the surface of the speaker and through its center. The nearest microphone location was 2 feet from the plane of the speaker. Traces of SPL vs frequency were obtained at 10 microphone locations. Measurements of SPL vs frequency were then made in the chamber of the wind tunnel at various azimuths, elevations and distances, and were compared with those obtained in the EE anechoic chamber. Typical examples of the test results above 250 Hz are shown in Figs. 12 and 13. We not that the results shown in Fig. 12 are favorable and those shown in Fig. 13 are not favorable. The results of the comparison for various positions are shown in Fig. 14. The coordinates used are shown in Fig. 15. The circle under the r column means near perfect agreement was obtained above 250 Hz at that microphone location. The cross means the agreement is not good above 250 Hz.

Before the extensive anechoic treatment, the regions in the FDL, MIT facility suitable for testing for the frequency ranges above 250 Hz were as shown in Figs. 16, 17 and 18. From these results, we know that the reflection-free space in our chamber was limited and that further anechoic treatment was required. Various modifications have been made to improve the anechoic property of the surface. The most effective one is the fiberglas board-block combination known as Cremer's technique.[25] This combination consists of two layers of fiberglas board, one layer of large fiberglas blocks and one layer of small blocks. The anechoic chamber was covered with these fiberglas block units. Each unit consists of two 2' x 4' x 2", 3 lb. #1000 spun glass boards, on top of which one layer of 4" x 4" x 3" ultra-acoustic blocks and

and thereon one layer of 2" x 2" x 3" blocks have been glued. Each unit was wrapped with a suitable non-flammable cloth (for health and safety reasons) and was attached to the chamber ceiling, walls and floor. A total of 70 units have been made and installed. Fig. 19 shows the anechoic chamber after this treatment. The treated areas are shown in Figs. 20, 21 and 22. The anechoic property of the chamber after treatment is shown in Figs. 23 to 27. We can see that the free field extends to a much larger region than that before the treatment. The three-dimensional view of the free field is shown in Figs. 28, 29 and 30. The accurate acoustic measurement in the chamber is thus ensured free of the reflections from the chamber surface. The lowest frequency above which the free field condition is obtained is reduced from the designed 250 Hz down to 160 Hz. The fiberglas block units proved to be very effective for the anechoic treatment of the FDL, MIT tunnel.

ii) Flow Visualization in the Anechoic Chamber

The flow field of FDL, MIT's 5' x 7 1/2' open jet wind tunnel was studied by applying flow visualization techniques. A smoke probe was positioned at various locations to make an extensive survey of the flow field at a 15 mph tunnel speed. The survey at other velocities showed the same general flow pattern. The flow pattern observed is sketched in Figs. 31 and 32. The main jet flow is uniform and steady. As shown, the flow between the shear layer and ceiling is essentially one large eddy and two small ones. Near the floor, an eddy exists in front of the fiberglas box and one behind it. About half of the flow impinging on the cowl spilled out. The spilled flow adjacent to the cowl circulates to the back of it and is sucked into the diffuser section through the slot between the cowl and the inlet of the diffuser section.

About 2/3 of the flow above the top part of the cowl tends to circulate towards the right (looking upstream) and then into the cowl slot. About 1/3 of the flow tends (not as strong) to circulate towards the left and eventually into the slot. As shown in Figs. 31 and 32, the flow close to the left part of the cowl tends to circulate and flows into the slot. The flow further from the cowl circulates as a big eddy and back into the main jet flow.

The cowl is basically a rectangular ring with a half circle cross section. Three layers of material are used in constructing it. The facing material is 18 x 16 (number of wires per square inch) anodized aluminum window screen. A layer of felt is in back of the window screen. Behind the felt, 1 x 1 mesh wires were used as shape supporting material.

Based on this smoke study, it is believed that the sucking effect of the cowl slot tends to release the local pressure generated around the cowl which cuts the pressure reinforcement cycle and in turn the instability of the tunnel flow. The porous surface with felt as backing material of the cowl is effective in avoiding edge tone. The disturbance which is generated at the nozzle tip reaches the porous cowl and is randomized and attenuated. Consequently, the feed back loop cannot be closed and the edge tone is avoided.

iii) Flow Reingestion Considerations

Because of the finite size of the wind tunnel, reingestion is always a problem in hover or at low forward flight speeds. This problem also exists for a hard-walled tunnel, but the actual details and the conditions for which it will occur are, in general, different. It is possible that certain

modifications will postpone problems of reingestion in an open-jet tunnel (for example, a diffuser system mounted on the floor or a cloth curtain mounted somewhere between the rotor plan and the floor.) This problem may be investigated using flow visualization to identify operating conditions for which the wake is smoothly convected into the diffuser. As an example, we used this technique to study reingestion problems with our two-bladed rotor at a tip angle of attack of 5°. Under these conditions, we found that there was a minimum advance ratio below which the reingestion could occur and meaningful experimental results might be difficult to obtain. Some typical examples of smoke pictures are shown in Fig. 33. The wake of the rotor was washed into the cowl for advance ratio larger than .057.

The configurations of 3, 4, 6, 8-blade rotor were also studied. The blade tip angle of attack of each blade was set to be 5°. The effect of rotor blade number on the minimum advance ratio without reingestion is shown in Fig. 34. The shaft was tilted forward 5° and 10° for a 2 and 4 bladed rotor, respectively. Fig. 35 shows the effect of shaft tilt angle on the minimum advance ratio without reingestion. Therefore, for each rotor configuration above the minimum advance ratio, reingestion did not interfere with the proper simulation of the rotor flow field. The rotor's wake angle relative to the free stream velocity can be approximated by the expression c_t/μ^2. Fig. 36 shows the wake angle vs advance ratio. Fig. 37 shows the wake angle vs the minimum advance ratio without reingestion for different number of blades.

The flow through the rotor disk was studied using flow visualization techniques for various rotor configurations. Some interesting vortex systems can be seen in the pictures taken. For example, Fig. 38 shows the

flow of a 2-bladed rotor of 5° blade tip setting for different shaft tilt angles. The vortex system is more distinct for increasing shaft tilt angle. This is because of the greater vortex strength and less dissipation due to less blade-vortex interaction for the larger shaft tilt angle used in these studies. This may explain why the higher harmonic content of the rotational noise spectrum decreases as the disk is tilted forward.[21] The helix vortex system at different stages after its shedding from the rotor blade can be clearly seen in these pictures, especially in the third picture of Fig. 38.

iv) Shear Layer Effect on Transmitting Sound

The presence of turbulence and non-uniform flow near the jet boundary will scatter and refract the sound field from a source in the free stream. This effect has been studied by using Aeolian tones as the sound source. Three cylinders of diameter 0.375, 0.18, and 0.09 inches were suspended horizontally in the middle plane of the wind tunnel test section to generate pure tones of frequency 550 Hz, 1.1 kHz and 2.3 kHz, respectively, at 50 mph tunnel speed. A 1/2 inch B & K condenser microphone was mounted on a frame and at a distance of 56 inches from the cylinders. The microphone along with the frame transverses an arc in the middle vertical plane. The measured results in comparison with the theoretical directivity pattern of stationary dipole and convection dipole without shear layer effect are shown in Figs. 39, 40 and 41. The results show that at the running Mach number (.067, 50 mph) and microphone angular location, the effect of the shear layer on sound transmitting through it is insignificant. The analytical studies by Amiet[27] support our measured results. In general, the effect of shear layer is believed to be significant for high Mach number and large microphone angular location.

IV. MACH NUMBER SCALING FORMULA

The helicopter rotor (rotational) noise is strongly dependent on the blade tip Mach number in addition to the other parameters. Most model rotor systems (including the FDL, MIT system) cannot simulate the tip Mach numbers of real helicopters. A theoretical Mach number scaling formula is, therefore, necessary in order to apply model rotor noise data to a full scale helicopter. A Mach number scaling formula has been developed and will be discussed as follows. The detail derivation can be found in Appendix A. The scaling formula derived may only be applied below the critical tip Mach number (i.e., the flow field is subsonic everywhere) which is the operation range of most helicopter rotors.

Our approach is based on the existing theoretical rotor noise work.[13] The following assumptions are involved in our derivation:

(1) A limited range of a loading harmonic acting on the rotor contribute significantly to each sound harmonic.

(2) Comparing the relative magnitudes of the Bessel functions occurring in the theoretical rotor noise expression, the $J_{n+\lambda}(nM\frac{y}{r})$ terms can be neglected in respect to $J_{n-\lambda}(nM\frac{y}{r})$ terms.

(3) The thrust dominates the air loading over the drag and radial components for a typical helicopter rotor.

(4) The unsteady blade lift coefficient is a function of advance ratio, Strouhal frequency, blade geometry, the incidence and the normalized radial location from the rotor hub.

The Mach number scaling formula is derived as

$$P(\vec{x}_2, n, M_{t2}) = P(\vec{x}_1, n, M_{t1})\left(\frac{M_{t2}}{M_{t1}}\right)^6 \left(\frac{c_2}{c_1}\right)^2 \left(\frac{r_1}{r_2}\right)^2 \left(\frac{\sin\alpha_2}{\sin\alpha_1}\right)^2$$

under the condition that $M_{t1} \cos\alpha_1 = M_{t2} \cos\alpha_2$, in addition that advance ratio, the observing azimuthal angle, blade geometry (including number of blades), and the incidences are the same in both cases, where

$P(\vec{x}_2, n, M_{t2})$ is the nth harmonic sound power at tip Mach number M_{t2} and observed at location $\vec{x}_2(\vec{r}_2, \alpha_2, \phi_2)$

$P(\vec{x}_1, n, M_{t1})$ is the nth harmonic sound power at tip Mach number M_{t1} and observed at location $\vec{x}_1(\vec{r}_1, \alpha_1, \phi_1)$

M_t is the blade tip Mach number

n is the harmonic number. n = mB. B is the number of blades m = 1, 2, 3 ...

c is the chord of the blade

γ, α, ϕ are the coordinates of the observer location and refer to Figure 42.

Subscripts 1, 2 refer to the rotor's operation at tip Mach number M_{t1}, M_{t2} and observer location x_1, x_2, respectively

$P(\vec{x}_1, n, M_{t1})$ can be measured by using our model rotor facility. The Mach number scaling formula can then be used to scale the measured model rotor noise data to that of the real helicopter rotor, $P(x_2, n, M_{t2})$ under the conditions outlined under the scaling formula. The harmonic number n of the measured model rotor noise data and the scaled helicopter rotor data are identical, but the frequencies are not the same because of the different angular velocity in both cases. The derived expression is, in general, not valid at near transonic Mach numbers. The upper Mach number range at which this scaling formula may apply requires additional experimental study and verification.

V. DEVELOPMENT OF THE DYNAMOMETER

i) Design of the Dynamometer

A dynamometer which was designed to measure the steady and low harmonics of the rotor thrust was developed. Fig. 44 shows the parts and the assembly of the dynamometer. The rotor hub floats on two sets of flexures of 1/6 inch thickness. This floating rotor hub can take any number of blades up to 8. Each flexure consists of four spokes and both flexures can be pre-loaded by tightening the nuts at the end of each spoke.

When no pre-loading is applied to the flexures, longitudinal natural frequency of the system is expected to be 300 cps or higher. Since bending and torsional modes are higher than the longitudinal natural frequency, these modes do not enter into the consideration of the stability of the system. When the model rotor is operated with eight blades at 1000 rpm, the fundamental blade passage frequency is 133 cps. This frequency is much lower than the lowest natural frequency of the system. In addition, the natural frequency of the system can be increased by pre-loading the flexures. Thus, it is expected that the system will be free of resonance.

Four semi-conductor strain gages were mounted on the lower flexure, two gages on each of two opposite spokes. These four gages form a temperature compensating bridge. BLH SPB 3-20-35 semi-conductor strain gages are used. The nominal resistance of one gage is 350 ohms and the nominal gage factor is 118. The choice of this kind of gage is based on the following three considerations:

(1) The total resistance of the gage bridge should be kept as low as possible. If the resistance of the bridge is high, then the wires connecting the bridge output terminal and read-out instrument will pick up the external

noise easily unless a very careful shielding is applied.

(2) The output signal voltage is proportional to the input excitation voltage. In order to have a higher signal, one needs a higher excitation voltage, the gage resistance should be high in order to keep the Joule heating low so that the gage will not be overheated. At 250 milliwatts, maximum power should dissipate from the gage mounted on a good heat sink as is recommended by BLH. The designed power dissipation of our system is 1/3 of the maximum limit.

(3) The gage filament length should be so long that a small defect on the flexure surface will not be sensed, while short enough that it will fit in the limited space.

These considerations led us to choose BLH SPB 3-20-35 semi-conductor strain gages and an excitation voltage of 6 volts. The strain gage mounting method and the strain gage balance system is illustrated in Fig. 45 where V is the excitation voltage of the bridge and ΔE is the signal voltage. If the thrust produced by the rotor is 48 lb. (this is the maximum theoretical thrust expected in the proposed work), the stress on the sections of the flexure spokes on which the strain gages are mounted is calculated to be 13.8×10^3 psia. The yield point of the metal used (17-4 PH steel) is 180×10^3 psi. The maximum dynamometer operating stress is, therefore, less than or equal to 7.7% of the material yield point. Even if the flexures are preloaded with 100 lbs of tension, the system is still operating at or less than 9.5% of the yield point. Hysteresis of the steel used is expected to be negligible.

The dynamometer was designed to mount on the top of the shaft of the existing model rotor system. The measurement system block diagram is shown in Figure 46.

ii) Measurement of Natural Frequency

The natural frequency of the dynamometer was determined experimentally. Fig. 47 shows the arrangement for the measurement. The dynamometer was mounted on an aluminum bar which was bolted down to the leads of two electric magnetic shakers, which were connected to an oscillator. A bridge balancing unit was used to adjust the strain gage balance exciting voltage to 6 v DC and to balance the gage bridge. The output of the dynamometer was connected to an oscilloscope. By slowly scanning the frequency output of the oscillator and observing the dynamometer output shown on the oscilloscope, the natural frequency of the dynamometer could be determined by noticing that when the shaking frequency approaches the natural frequency, the signal amplitude on the oscilloscope increases drastically.

The observed fundamental natural frequency was measured as 365 Hz. The first and second harmonics are 500 Hz and 655 Hz, respectively. The measured value of the first natural frequency (365 Hz) is close to and better than the designed value of 300 Hz. For a 2-bladed rotor at 1000 rpm, the fundamental blade passage frequency is 33 Hz. The dynamometer can measure the thrust up to the 10th harmonic without the difficulty of resonance. While for an 8-bladed rotor at 1000 rpm, up to 2nd thrust harmonic can be measured.

iii) Static Calibration of the Dynamometer

The dynamometer was mounted on a test stand and the circuit for the strain gage bridge was passed through the sliprings in order to best approximate the operating configuration. The apparatus for the calibration is shown in Figure 48. The excitation voltage to the strain gage bridge was adjusted to 6 v DC. It was found that since the semi-conductor strain gages used are very light sensitive, the dynamometer had to be wrapped with black paper in

order that no light could reach the strain gage. The dynamometer was loaded with a dead weight which was increased in units of 5 lbs. to 40 lbs. after which it was unloaded in units of 5 lbs. in order to check for hysteresis. The strain gage output was read in millivolts from a digital voltmeter at every 5 lbs. increment. The system had to be loaded and unloaded several times until the system was "worked in" so that hysteresis effects became negligible. Figure 49 shows the variation of the strain gage bridge output with weight when hysteresis was considered negligible. The average slope for the test runs was found to be .557 mv/lb. These runs were made at a temperature of 85°F. Runs were also made at higher temperatures. This was done by covering the test stand with fiberglas blankets and placing a heat lamp under the dynamometer. The temperature was regulated by changing the distance of the lamp to the dynamometer. Runs were made at 90°F and 101°F and it was found that the slope of the plots (mv/lb) remained constant within the temperature range tested (as should be expected since the bridge was designed to be temperature compensating).

VI. LIST OF THE WORK DONE ON HELICOPTER NOISE IN OUR GROUP

1. "A Correlation of Vortex Noise Data from Helicopter Main Rotors," Sheila E. Widnall, J. Aircraft, Vol. 6, No. 3, May, 1969. The work was supported by ARO, Durham, under Contract DA-31-124-ARO-D-471.

2. "Helicopter Noise Due to Blade/Vortex Interaction," Sheila E. Widnall, J. Acoust. Soc. Amer. 50, No. 1 (Part 2), 1971. The work was supported by ARO, Durham, under Contract No. DA-31-124-ARO-D-471.

3. "Theoretical and Experimental Studies of Helicopter Noise Due to Blade/Vortex Interaction," Sheila E. Widnall, Sing Chu and Albert Lee, Helicopter Noise Symposium, sponsored by ARO-Durham, September, 1971. The work was supported by ARO, Durham, under Contract No. DA-31-124-ARO-D-471.

4. "Rotational Noise Characteristics of Helicopters," David Kiang and Chen Y. Ng, FTL TM 71-8, M.I.T., December, 1971.

5. "The Development of a Wind Tunnel Facility for the Study of V/STOL Noise," Paul Bauer and Sheila E. Widnall, FTL Report R-72-6, M.I.T., August, 1972. The work was supported by ARO-Durham, under Contract No. DAHC04-69-C-0086.

6. "Blown Flap Noise," Martin Haas, FTL Report R-72-5, M.I.T., June, 1972. The work was supported by DOT under Contract No. DOT-TSC-93.

7. "Experimental Studies of Rotational Noise in Forward Flight," Sheila E. Widnall, Paul Bauer and Albert Lee, Proceedings of the American Helicopter Society, Mideast Region Symposium, Essington, Pennsylvania, October, 1972. The work was supported by ARO-Durham, under Contract No. DAHC04-69-C-0086 and DOT under Contract No. DOT-TSC-93.

8. "Some Aspects of V/STOL Noise," Proceedings of the DOT Conference on University Research in Transportation Noise, Stanford University, March, 1973, Sheila E. Widnall, Sing Chu, Albert Lee et al. The work was supported under Contract DOT-TSC-93 and the Army Research Office.

VII. CONCLUSIONS

The low-noise, open-jet anechoic wind tunnel is essential for the study of helicopter rotor noise. The free field of our anechoic chamber was extended substantially by fiberglas block treatment and the cut-off frequency is reduced to 160 Hz. This fiberglas block treatment is effective and is, therefore, recommended for anechoic chamber treatment. The Mach number scaling formula derived is necessary for extrapolating the model rotor rotational noise data to the full size helicopter. The dynamometer system developed in this program is useful in measuring the important steady and unsteady thrusts. The effects of turbulence and velocity shear near the jet boundary on acoustic wave propagation has been determined for our operating conditions. Flow field patterns in the anechoic chamber have been mapped. In conclusion, our facilities and equipment are unique and very suitable for helicopter rotor noise study in which aerodynamic events and acoustic radiation are measured simultaneously.

APPENDIX A

The Derivation of Mach Number Scaling Formula for Rotor Noise

The scaling formula derived may only be applied below the critical tip Mach number (i.e., the flow field is subsonic everywhere) which is the operation range for most helicopters.

The expression of the complex Fourier coefficient of sound radiation C_n in the far field due to a rotating fluctuation point force acting at a distance R from the rotor hub is[13]

$$C_n = \sum_{\lambda=0}^{\infty} \frac{i^{-(n-\lambda)}}{4\pi} \left\{ \frac{n\Omega x}{a_o r^2} [ia_{\lambda T}(J_{n-\lambda} + (-)^{\lambda} J_{n+\lambda}) - b_{\lambda T}(J_{n-\lambda} - (-)^{\lambda} J_{n+\lambda})] - \frac{i\, a_{\lambda D}}{Rr} ((n-\lambda)J_{n-\lambda} + (-)^{\lambda} (n+\lambda)J_{n+\lambda}) + \frac{b_{\lambda D}}{Rr} ((n-\lambda)J_{n-\lambda} - (-)^{\lambda} (n+\lambda)J_{n+\lambda}) + \frac{n\Omega y}{a_o r^2} [a_{\lambda C} (J'_{n-\lambda} + (-)^{\lambda} J'_{n+\lambda}) + i\, b_{\lambda C} (J'_{n-\lambda} - (-)^{\lambda} J'_{n+\lambda})] \right\} \qquad (1)$$

The argument of the Bessel functions in Eq.(1) is $nM\frac{y}{r}$. The coordinates are shown in Fig. 42 where

$a_{\lambda T}$, $b_{\lambda T}$ = the Fourier coefficients of the thrust of harmonic λ

$a_{\lambda D}$, $b_{\lambda D}$ = the Fourier coefficients of the drag of harmonic λ

$a_{\lambda C}$, $b_{\lambda C}$ = the Fourier coefficients of the radial force, of harmonic λ

$J_{n-\lambda}$, $J_{n+\lambda}$ = the Bessel function of order $n-\lambda$, $n+\lambda$ respectively, the argument is $\frac{nMy}{r}$

$J'_{n-\lambda}$, $J'_{n+\lambda}$ = the derivatives of $J_{n-\lambda}$ and $J_{n+\lambda}$, respectively

a_o = speed of sound

n = the harmonic number of sound n = mB, m = 1, 2, ...

B = the number of blades

In Eq. (1), there are two basic terms, $J_{n+\lambda}$ and $J_{n-\lambda}$. The typical value of m, B, M and $\frac{y}{r}$ are 4, 4, .5 and .5, respectively. The typical value of $nM\frac{y}{r}$ is 4. The typical values of n and λ are much larger than one except for the steady and low harmonic loading, i.e., $\lambda = 0$ or small integer. It will be shown later that the range of air loading for which λ contributes significantly to the sound radiation is $n(1 - K M \frac{y}{r}) < \lambda < n(1 + K M \frac{y}{r})$ where $K > 1$, typically $K = 1.36$. Therefore, the values of n and λ are much larger than one typically. Thus, $J_{n+\lambda} << J_{n-\lambda}$ and $J_{n+\lambda}$ terms can be neglected.

Only a limited range of air loading harmonics λ contributes significantly to each sound harmonic n. This can be understood by examining the behavior of the Bessel function $J_{n-\lambda}$. As the λ increases, the order of the Bessel function $n-\lambda$ will decrease, eventually becoming negative. Since $|J_p| = |J_{-p}|$ if p is integer, the contribution of each harmonic loading λ to the n^{th} sound harmonic is symmetrical about $\lambda = n$. As the argument of the Bessel function, $nM\frac{y}{r}$, is decreasing, the range of $|n-\lambda|$ in which the magnitude of $J_{n-\lambda}$ differs from zero is reduced.

When $|n-\lambda| >> 1$,

$$J_{n-\lambda}(nM\frac{y}{r}) \sim \frac{1}{\sqrt{2\pi\,|n-\lambda|}}\left[\frac{enM\frac{y}{r}}{2|n-\lambda|}\right]^{|n-\lambda|}$$

If $\frac{enM\frac{y}{r}}{2|n-\lambda|} \leq 1$, then $J_{n-\lambda}(nM\frac{y}{r}) \to 0$ as $|n-\lambda| \to$ large.

i.e.,

$$|n-\lambda| \geq \frac{enM\frac{y}{r}}{2} \equiv KnM\frac{y}{r}$$

where

$$K = \frac{e}{2} = 1.36 \quad (e = 2.718\ldots)$$

The above argument is not applicable when $|n-\lambda|$ is not much larger than one. In Fig. 43, we plot the curve $|n-\lambda| = f(nM\frac{y}{r})$, dividing the magnitude of $J_{n-\lambda}(nM\frac{y}{r})$ larger than 0.00 from that smaller than 0.00. The line of $n-\lambda = KnM\frac{y}{r}$ is also shown in Fig. 41. It is obvious that the expression $KnM\frac{y}{r}$ is a good approximation for $f(nM\frac{y}{r})$. Consequently, the range of the loading harmonic λ which contributes significantly to the sound harmonic n can be written as

$$n[1 - f(nM\frac{y}{r})] < \lambda < n[1 + f(nM\frac{y}{r})]$$

The typical proportion of the force components of a typical helicopter rotor is 10 : 1 : 1. By examining Eq. (1), it is observed that in the inefficient region of radiation (i.e., out of the range $n - KnM\frac{y}{r} < \lambda < n + KnM\frac{y}{r}$, the effects of all three components are about equal. However, over the efficient radiation range, the thrust term dominates. For most practical purposes, it would appear to be a good approximation to consider the thrust term only. Some numerical calculations on the noise radiation due to each force component can be found in Ref. (13) and support this simplification.

Based on the above discussion, for practical purposes, Eq. (1) can

be simplified as

$$C_n = \sum_{\lambda = n - f(nM\frac{y}{r})}^{\lambda = n + f(nM\frac{y}{r})} \frac{i^{-(n-\lambda)}}{4\pi} \left\{ \frac{n\Delta x}{a_o r^2} \left[i\, a_{\lambda T} - b_{\lambda T} \right] J_{n-\lambda}\left(nM\frac{y}{r}\right) \right\} \quad (2)$$

If we want to calculate the sound radiation by using Eq. (1) or Eq. (2), we need more detailed information on the loading harmonics which is not known up to this point. In the scaling formula derived below, we do not have to know this information. It is reasonable to assume that the unsteady blade lift coefficient is a function of advance ratio μ, Strouhal frequency λ, blade geometry G, incidence $\bar{\alpha}$ and the normalized radial location $\bar{t}$ where the unsteady blade lift acts.

$$C_{\lambda T} = C_{\lambda T}(\mu, \lambda, G, \bar{\alpha}, \bar{t}) \quad (3)$$

In the case of a helicopter rotor, the observed sound is the result of the continuous distributed loading along the blade instead of the point loading. Therefore, the power spectral density of the sound $P(\vec{x}, n)$ observed at location $\vec{x}$ is

$$P(\vec{x}, n) \lim_{T \to \infty} \frac{1}{T} \int dT \int_{\eta} \int_{\eta'} C_n(\vec{x}, \eta)\, C_n^*(\vec{x}, \eta')\, d\eta\, d\eta' \quad (4)$$

where C_n^* is the complex conjugate of C_n.

The radial distance η can be normalized as $\bar{t} = \frac{\eta}{b}$, where b is the span of the blade.

The air loading in Eq. (2) is

$$\sqrt{a_\lambda^2 + b_\lambda^2} \equiv \frac{1}{2}\rho(n\Omega)^2 C_{\lambda T} C$$

$$= \rho(b\Omega)^2 C \gamma_T(\mu, \lambda, G, \bar{\alpha}, \bar{t}) \qquad (5)$$

where C is the chord of the blade

$$\gamma_T = \frac{1}{2}\bar{t}^2 C_{\lambda T}$$

Substituting Eq. (2) and (5) into Eq. (4), we have

$$P(\vec{x}, n) = \frac{1}{2}\left[\frac{1}{4\pi}\frac{nb\Omega x}{a_o r^2}\right]^2 [\rho b^2\Omega^2 C]^2 \sum_{\substack{\lambda,\lambda' = n+f(nM_t\frac{y}{r}) \\ \lambda,\lambda' = n-f(nM_t\frac{y}{r})}} \int_0^1\int_0^1 \gamma_T(\mu, \lambda, G, \bar{\alpha}, \bar{t})$$

$$\cdot \gamma_T(\mu, \lambda', G, \bar{\alpha}, \bar{t}') e^{i[\phi_\lambda \bar{t} - \phi_{\lambda'}\bar{t}']} J_{n-\lambda}(nM_t\bar{t}\frac{y}{r}) J_{n-\lambda}(nM_t\bar{t}'\frac{y}{r}) d\bar{t}\, d\bar{t}' \qquad (6)$$

where M_t is the blade tip Mach number.

The phase $e^{i[\phi_\lambda \bar{t} - \phi_{\lambda'}\bar{t}']}$ is independent of the tip Mach number M_t and the sound observing location.

In Eq. (6), the upper and lower range of summation and the quantities behind it depend on n and $M_t \frac{y}{r}$ in addition to μ, G, $\bar{\alpha}$. Let $P(\vec{x}_1, n, M_{t1})$ be the n^{th} harmonic sound power measured at tip Mach number M_t and at location $\vec{x}_1$. Using the measured $P(\vec{x}_1, n, M_{t1})$, we want to predict the sound power $P(\vec{x}_2, n, M_{t2})$ at tip Mach number M_{t2} and location $\vec{x}_2$. If $M_{t1}(\frac{y}{r})_1 = M_{t2}(\frac{y}{r})_2$, the factor multiplying $[\rho b^2\Omega^2 C]^2$ in Eq. (6) are identical at different Mach numbers and observing locations. Using Eq. (6), we have

$$P(\vec{x}_2, n, M_{t2}) = P(\vec{x}_1, n, M_{t1})\left(\frac{M_{t2}}{M_{t1}}\right)^6\left(\frac{C_2}{C_1}\right)^2\left(\frac{r_1}{r_2}\right)^2\left(\frac{\sin\alpha_2}{\sin\alpha_1}\right)^2 \qquad (7)$$

providing $M_{t1}(\frac{y}{r})_1 = M_{t2}(\frac{y}{r})_2$ and μ, G, α are the same in both cases (noting $\sin\alpha = \frac{x}{r}$, $\cos\alpha = \frac{y}{r}$).

Eq. (7) is applicable for the hovering helicopter. For the forward flight case, r in Eq. (6) should be replaced by $r(1 - M_{or})$ as suggested in Ref. (13), where M_{or} is the component of the forward flight Mach number M_o in the direction of observer:

$$M_{or} = M_o \cos\beta = \mu M_t \cos\beta = - \mu M_t \cos\phi \cos\alpha \tag{8}$$

The factors $\frac{x}{r^2}$ and $M_t \frac{y}{r}$ in Eq. (7) should be replaced by

$$\begin{aligned} \frac{x}{r^2} &\Rightarrow \frac{x}{r^2(1 + \mu M_t \cos\phi \cos\alpha)^2} = \frac{\sin\alpha}{r(1 + \mu M_t \cos\alpha \cos\phi)^2} \\ M_t \frac{y}{r} &\Rightarrow \frac{M_t\, y}{r(1 + \mu M_t \cos\phi \cos\alpha)} = \frac{M_t \cos\alpha}{r(1 + \mu M_t \cos\alpha \cos\phi)} \end{aligned} \tag{9}$$

Using Eq. (9), Eq. (6) becomes

$$\begin{aligned} P(\vec{x}, n) = \frac{1}{2}\Big\{\frac{1}{4\pi} & \frac{nM_t \sin\alpha}{r(1 + \mu M_t \cos\alpha \cos\phi)^2}\Big\}^2 [\rho\, a_o^2\, M_t^2\, C] \\ & \sum_{\lambda,\,\lambda'} = n + f(n \frac{M_t \cos\alpha}{1+\mu M_t \cos\alpha \cos\phi}) \\ & \sum_{\lambda,\,\lambda'} = n - f(n \frac{M_t \cos\alpha}{1+\mu M_t \cos\alpha \cos\phi}) \\ & \int_0 \int_0 \gamma_T(\mu, \lambda, G, \bar{\alpha}, \bar{t})\, \gamma_T(\mu, \lambda', G, \bar{\alpha}, \bar{t}')\, e^{i(\phi_{\lambda}\bar{t} - \phi_{\lambda'}\bar{t}')} \\ & J_{n-\lambda}(\frac{nM_t \cos\alpha\, \bar{t}}{1+\mu M_t \cos\alpha \cos\phi})\, J_{n-\lambda'}(\frac{nM_t \cos\alpha\, \bar{t}'}{1+\mu M_t \cos\alpha \cos\phi})\, d\bar{t}\, d\bar{t}' \end{aligned} \tag{10}$$

Examining Eq. (10), the same Mach number formula for the forward flight case is obtained as Eq. (7) for the hovering case, providing $M_{t1} \cos\alpha_1 = M_{t2} \cos\alpha_2$, the sound harmonic number, the azumuthal angle ϕ, the advance ratio μ, the blade geometry G (including the number of blades) and the incidence angle $\bar{\alpha}$ are the same in both cases. In addition, the fluids must be similar.

REFERENCES

1. C. R. Cox, "Rotor Noise Measurements in Wind Tunnels," Proc. Third CAL/AVLABS Symposium, 18-20 June 1969, Buffalo, New York.

2. C. R. Cox and R. R. Lynn, "A Study of the Origin and Means of Reducing Helicopter Noise," Bell Helicopter Company; USATCREC Technical Report 62-73, U. S. Army Transportation Research Command, Fort Eustis, Virginia, November, 1962.

3. Conference on Helicopter and V/STOL Noise Generation and Suppression, U. S. Army, National Academy of Sciences, National Academy of Engineering Conference, Washington, D. C., July 30-31, 1968.

4. S. E. Widnall, "Helicopter Noise Due to Blade-Vortex Interaction," Journal of the Acoustical Society of America, 50, No. 1, Part 2, p. 354, July, 1970.

5. S. E. Widnall, S. Chu, A. Lee, "Theoretical and Experimental Studies of Helicopter Noise due to Blade-Vortex Interaction", Helicopter Noise Symposium Sponsored by ARO-Durham, September 28-30, 1971.

6. R. H. Lyon, "Radiation of Sound by Airfoils that Accelerate near the Speed of Sound," J. Acoust. Soc. Amer. 49, 894-905, 1971.

7. R. H. Lyon, W. D. Mark and R. W. Pyle, Jr., "Synthesis of Helicopter Rotor Tips for Less Noise," Helicopter Noise Symposium, sponsored by ARO-Durham, September 28-30, 1974.

8. R. E. A. Arndt, and D. C. Borgman, "Noise Radiation from Helicopter Rotors Operating at High Tip Mach Numbers," presented at 16th Annual National Forum of the Am. Helicopter Soc., Washington, D. C., June, 1970, Amer. Helicopter Soc. Preprint No. 402.

9. W. E. Bausch and R. G. Schlegel, "An Experimental Study of Helicopter Rotor Impulsive Noise," Helicopter Noise Symposium, sponsored by ARO-Durham, September 28-30, 1971.

10. S. G. Sadler, "Determination of the Aerodynamic Characteristics of Vortex Shedding from Lifting Airfoils for Application to the Analysis of Helicopter Noise," Helicopter Noise Symposium, sponsored by ARO-Durham, September 28-30, 1971.

11. J. Scheiman and D. A. Hilton, "Rotating Blade Vortex Noise With and Without Axial Velocity," Helicopter Noise Symposium, sponsored by ARO-Durham, September 28-30, 1971.

12. R. W. Paterson, P. G. Vogt, R. K. Amiet and M. R. Fink, "Vortex Shedding Noise of an Isolated Airfoil," Helicopter Noise Symposium, sponsored by ARO-Durham, September 28-30, 1971.

13. M. V. Lowson and J. B. Ollerhead, "Studies of Helicopter Rotor Noise," Wyle Laboratories; USSAVLABS Technical Report 68-60, U. S. Army Aviation Material Laboratories, Fort Eustis, Virginia, January, 1969, AD 684394.

14. S. E. Wright, "Sound Radiation from a Lifting Rotor Generated by Asymmetric Disk Loading," Jl. Sound, Vib., Vol. 9, No. 2, 1969, pp. 223-240.

15. R. G. Schlegel, R. J. King, and H. R. Mull, "Helicopter Rotor Noise Generation and Propagation," Sikorsky Aircraft, USAAVLABS Technical Report 66-4, U. S. Army Aviation Material Laboratories, Fort Eustis, Virginia, October, 1966, AD 645884.

16. S. G. Sadler and R. G. Loewy, "A Theory for Predicting the Rotational and Vortex Noise of Lifting Rotors in Hover and Forward Flight," Rochester Applied Science Associates, Inc., NASA Contractor Report 1333, National Aeronautics and Space Administration, Washington, D. C., May, 1969.

17. R. J. King and R. G. Schlegel, "Prediction Methods and Trends for Helicopter Rotor Noise," Proc. Third CAL/AVLABS Symposium, 18-20 June, 1969, Buffalo, New York.

18. S. E. Wright and J. W. Leverton, "Helicopter Rotor Noise Generation," Proc. Third CAL/AVLABS Symposium, 18-20 June 1969, Buffalo, New York.

19. S. E. Widnall, "The Stability of a Helical Vortex Filament," J. Fluid Mech. 54, Part 4, pp. 641-663, 1972.

20. P. Bauer and S. E. Widnall, "The Development of a Wind Tunnel Facility for the Study of V/STOL Noise, " FTL Report R-72-6, MIT, August, 1972.

21. S. E. Widnall, P. Bauer and Albert Lee, "Experimental Results of Rotational Noise in Forward Flight." Proceedings of the American Helicopter Society, Mideast Region Symposium, Essington, Pennsylvania (Oct. 1972).

22. Martin Haas, "Blown Flap Noise," FTL Report R-72-5, MIT, June, 1972.

23. L. T. Clark, "The Radiation of Sound from an Airfoil Immersed in a Laminar Flow," ASME Paper No. 71-G-4, ASME 6th Annual Gas Turbine Conference and Products Show, Houston, Texas, March, 1971.

24. M. V. Lowson, "Rotor Noise Mechanisms," MIT Interdepartmental Acoustic Seminar, September, 1972.

25. L. Cremer, "Theorie Der Luftschall-Dampfung Im Rechteckkanal Mit Schluckender Wand Und Das Sich Dabei Ergebende Hochste Dampfungsmass," Acustica 3, No. 2, 1953, pp. 249-263.

26. S. E. Widnall, "Wind Tunnel Studies of Helicopter Rotational Noise In Forward Flight," presented to the Acoustical Society of America Meeting, Miami (November, 1972).

27. R.K., Amiet, "Propagation of Sound Through a Two-Dimensional Shear Layer with Application to Measurements in the Acoustic Research Tunnel," Report UAR-L40, March 1972, United Aircraft Research Lab., East Hartford, Conn.

Figure 1 View of test section in low noise acoustic wind tunnel.

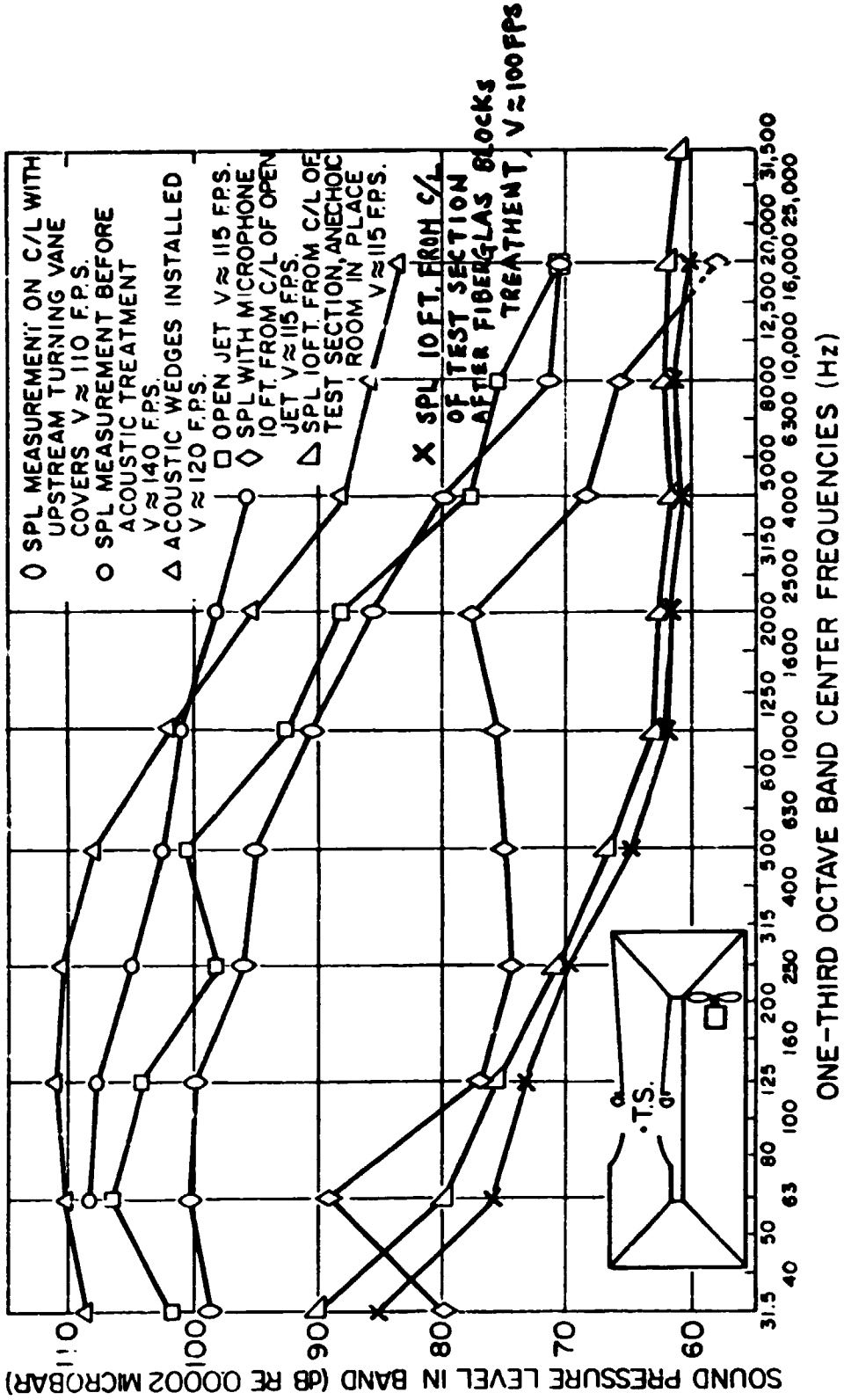

FIG. 2 SPL MEASUREMENTS OF BACKGROUND NOISE IN TEST SECTION CORRECTED TO 1/3 OCTAVE BANDWIDTH

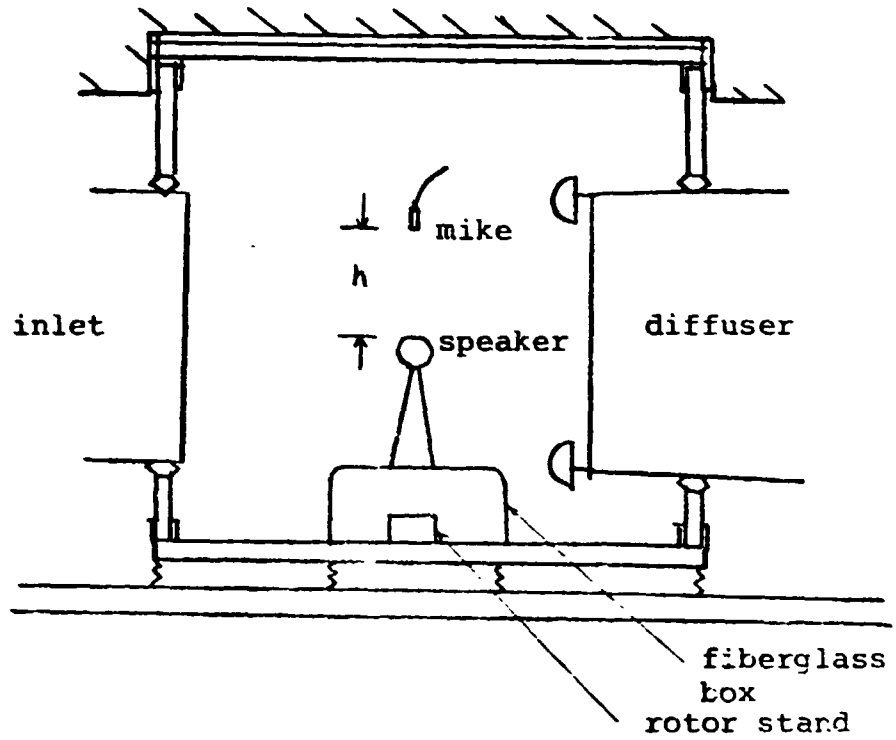

Fig. 3 The configuration for the testing of the acoustic property of the anechoic chamber

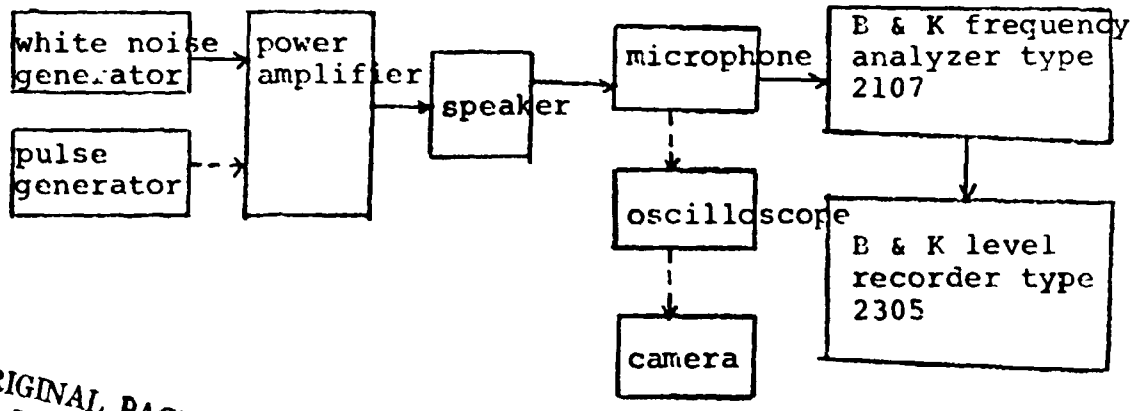

Fig. 4 Instrumentation set-up

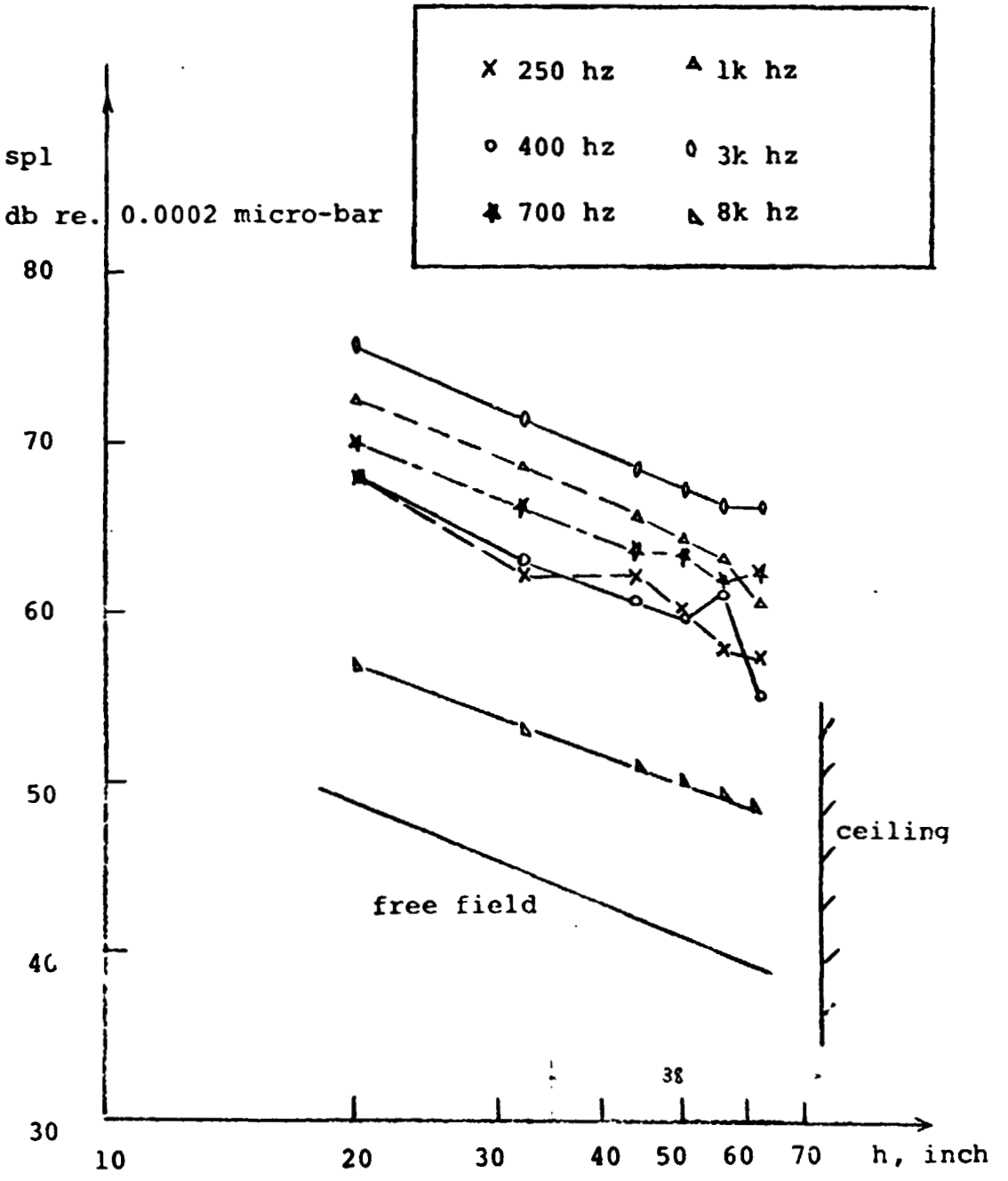

Fig. 5 Acoustic property of the anechoic chamber ceiling

The noise source is mounted at the rotor shaft tip location before fiberglass blocks treatment

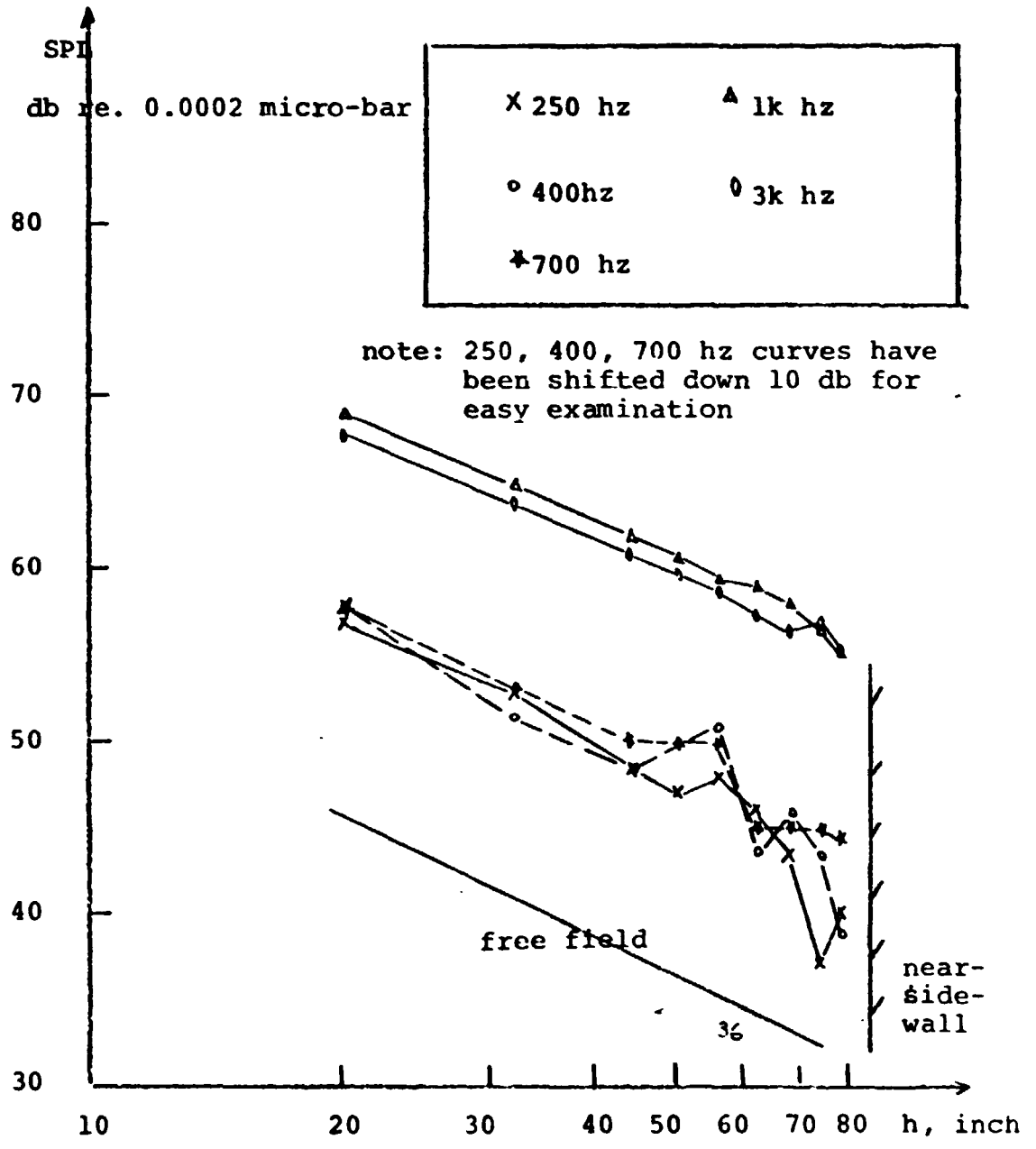

Fig. 6 Acoustic property of the anechoic chamber near-side wall. The noise source is mounted at the rotor shaft tip location (before fiberglass blocks treatment)

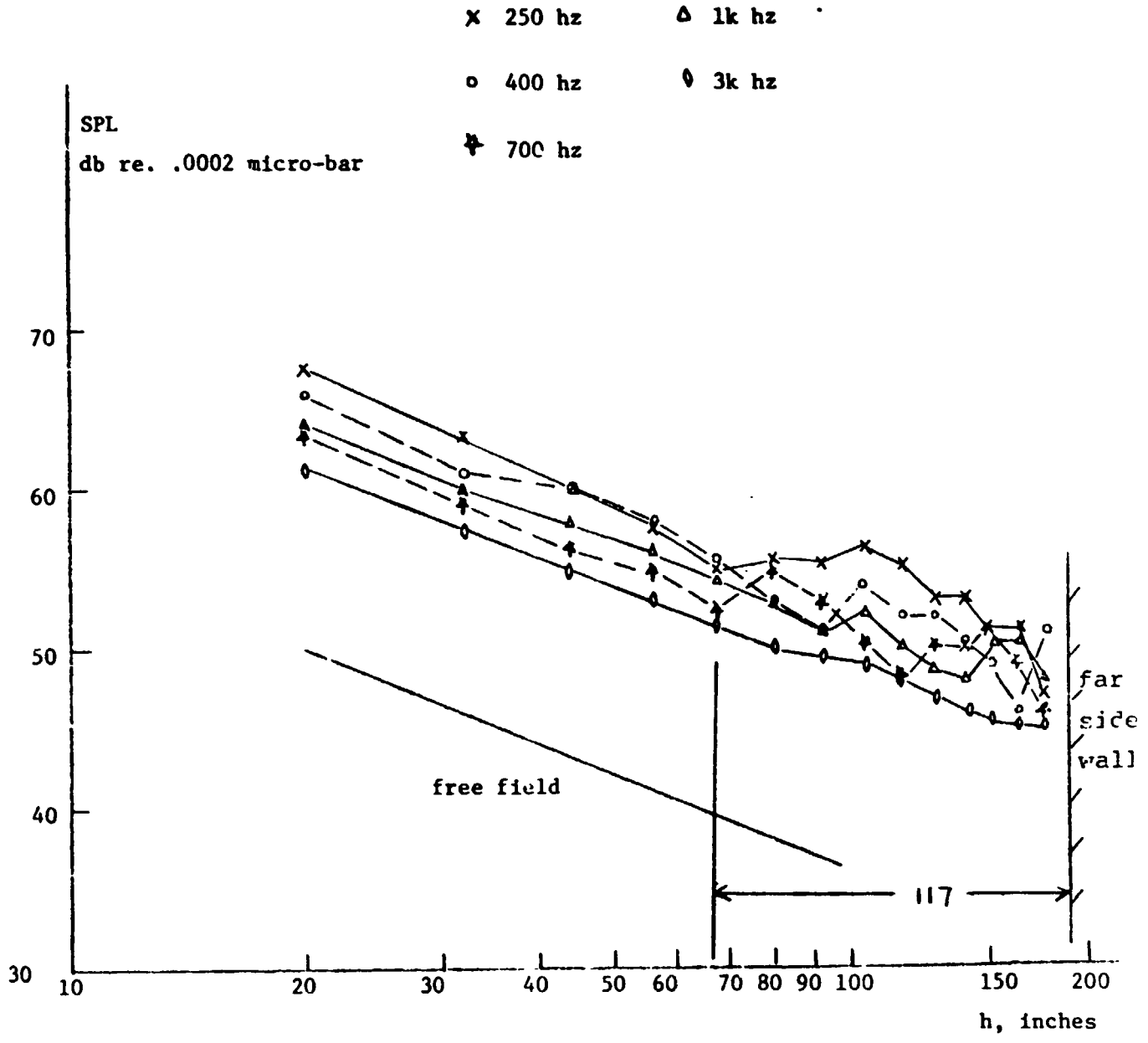

fig. 7 Acoustic property of the far sidewall

The noise source is mounted at the rotor shaft tip location

(before fiberglass blocks treatment)

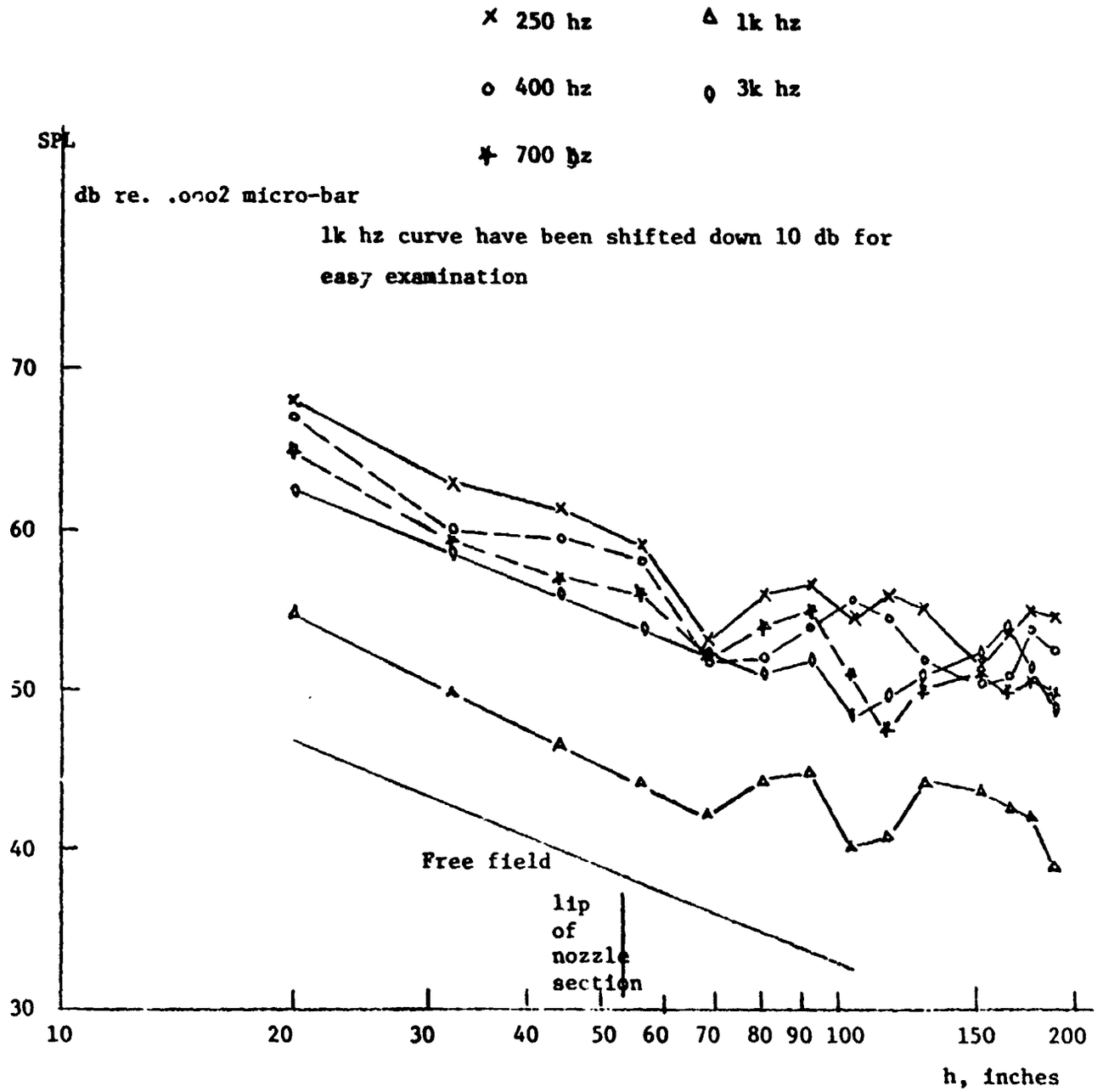

Fig. 8 Acoustic property of the nozzle section

The noise source is mounted at the rotor shaft tip location

(before fiberglass blocks treatment)

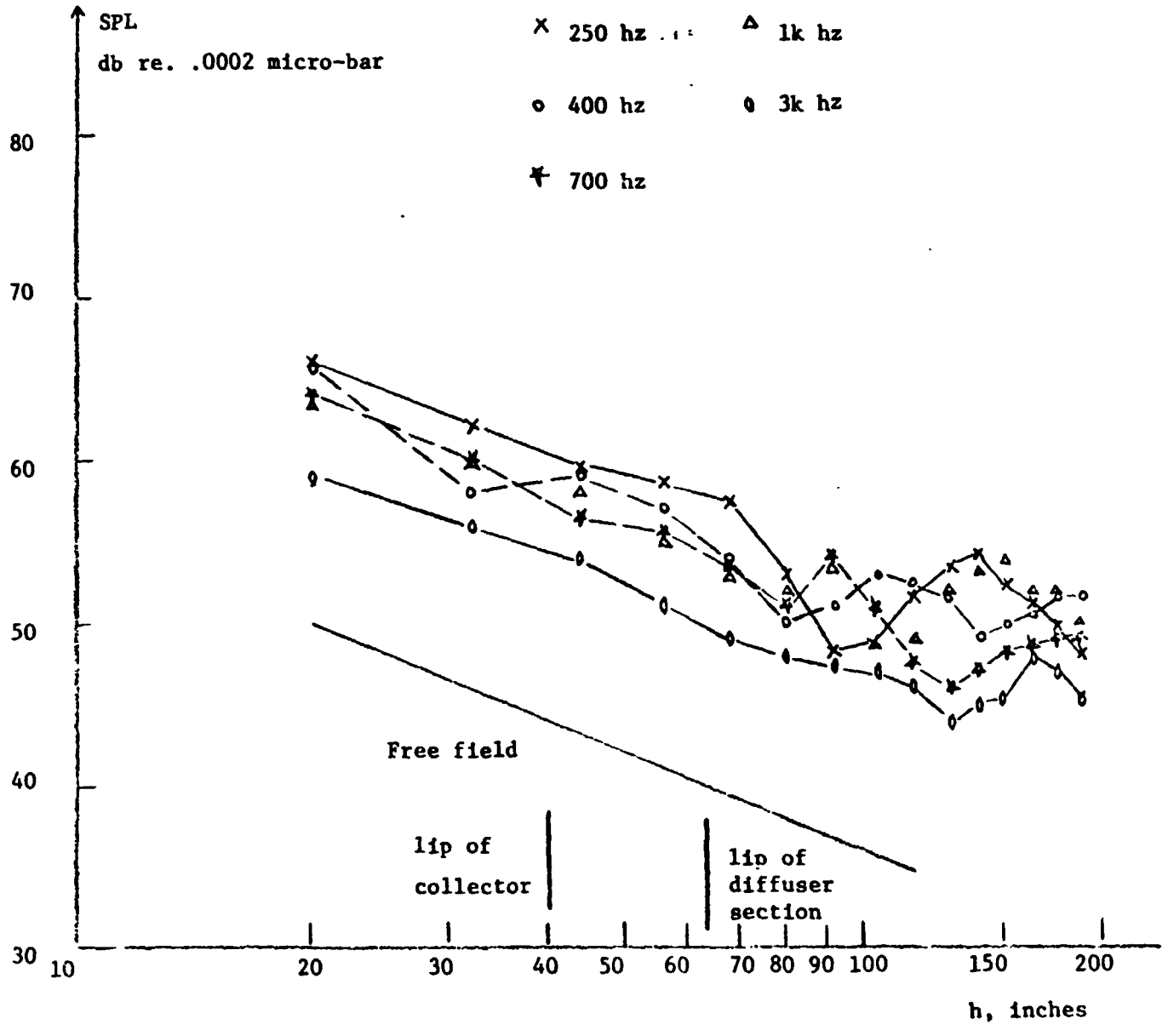

Fig. 9 Acoustic property of the diffuser section

The noise source is mounted at the rotor shaft tip location

(before fiberglass blocks treatment)

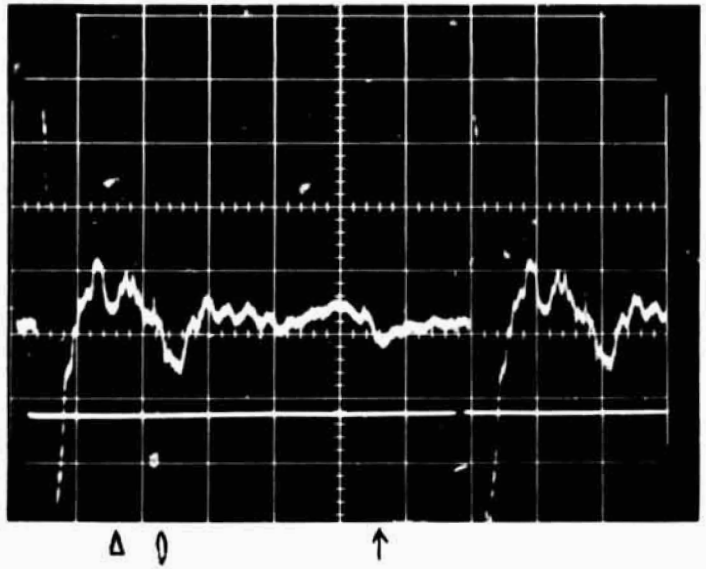

h = 20 inches

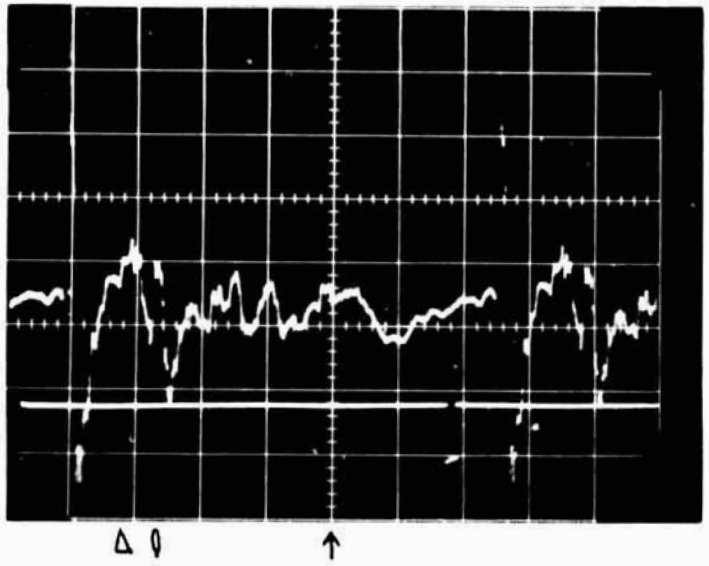

h = 56 inches

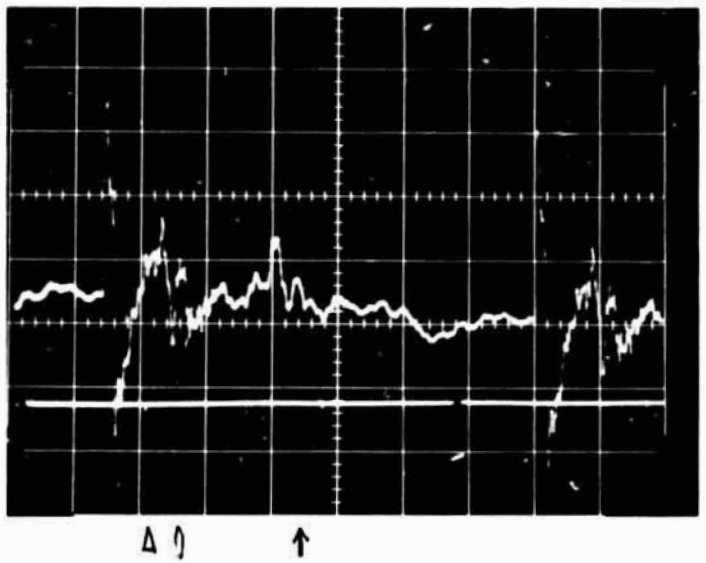

h = 92 inches

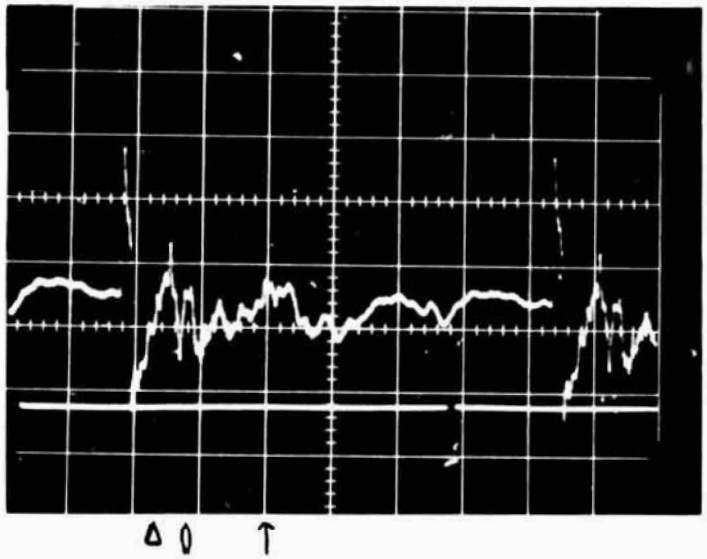

h = 116 inches

Fig. 10 Real-time testing on anechoic chamber far side wall before additional fiberglas blocks treatment
↑, 0, Δ : reflection from chamber far side wall, ceiling, and floor, respectively

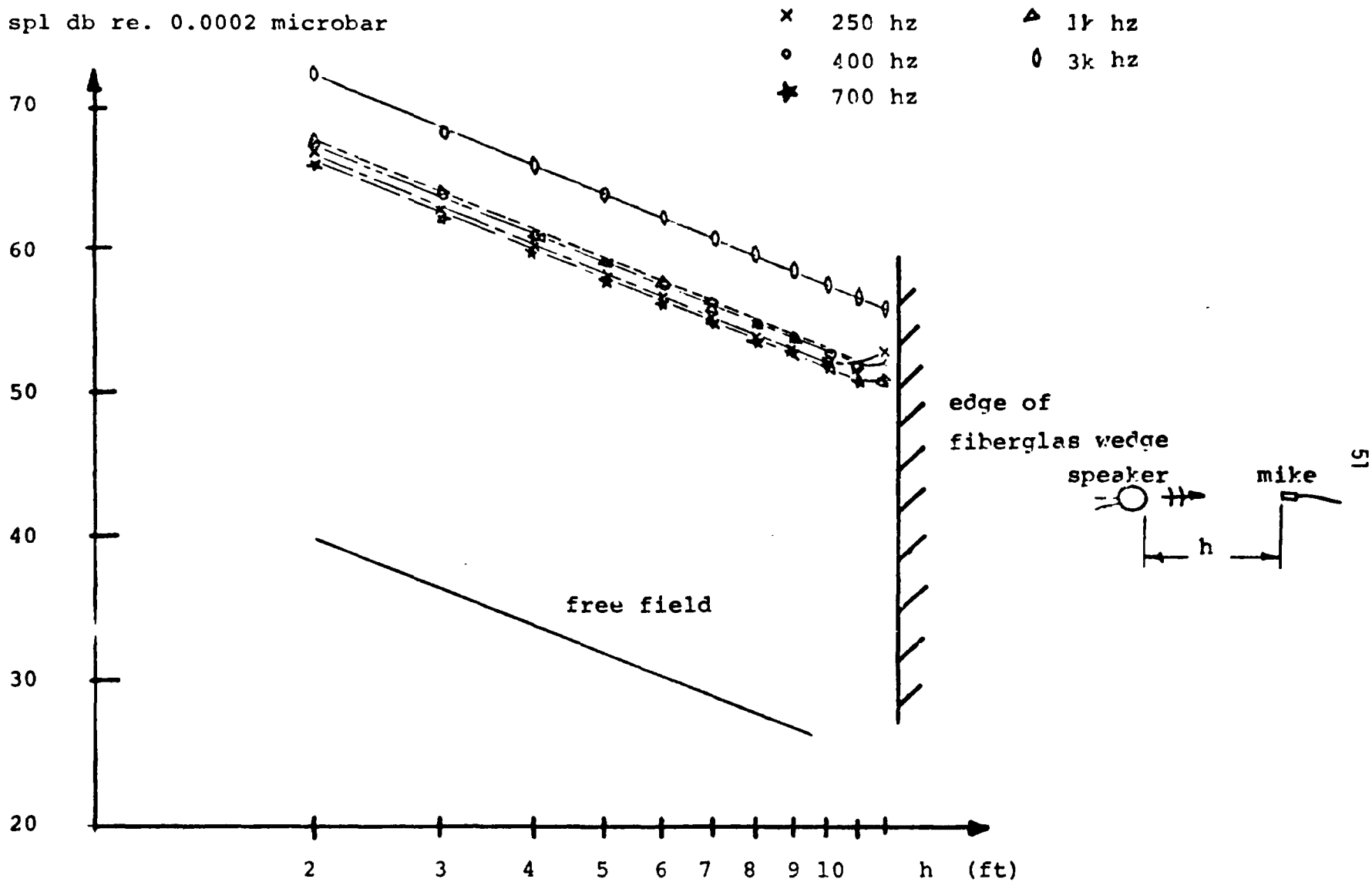

Fig. 11 The anechoic property of E.E. anechoic chamber

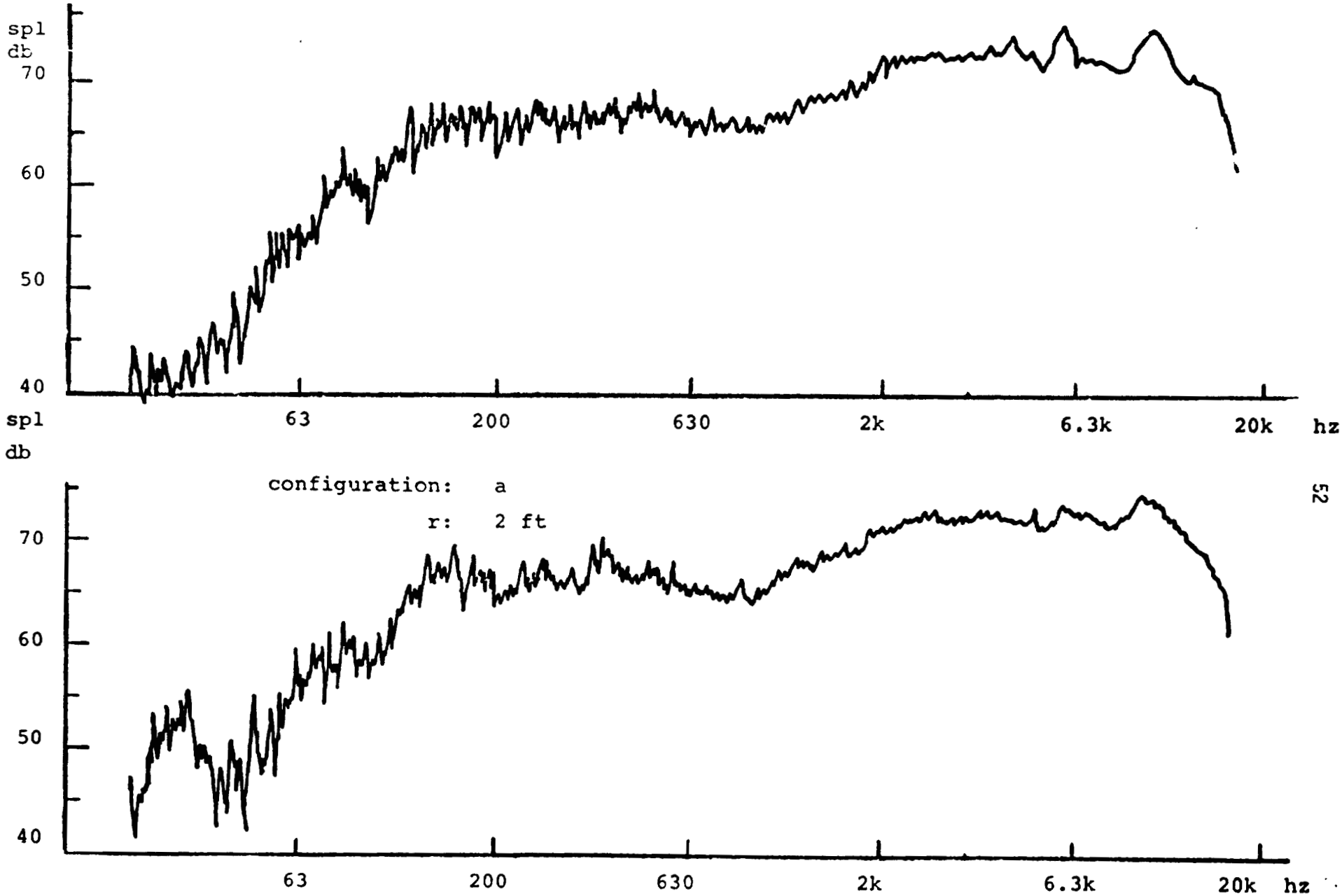

Fig. 12 comparison of spl vs frequency trace obtained in M.I.T. E.E. anechoic chamber (top) with that in anechoic tunnel (bottom)

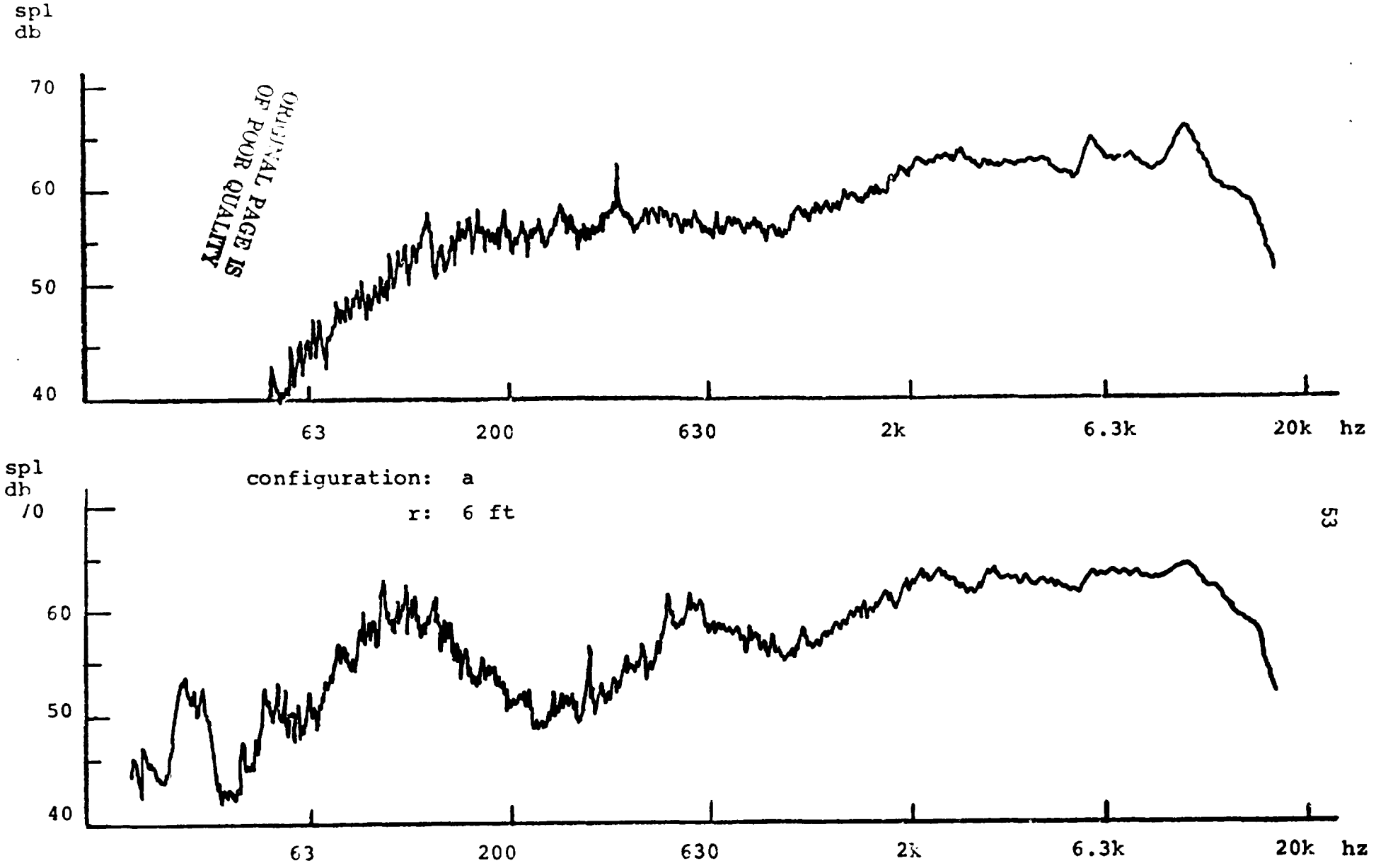

Fig. 13 comparison od spl vs frequency trace obtained in M.I.T. E.E. anechoic chamber (top) with that in anechoic tunnel (bottom)

0: nearly perfect

x: Off

above 250 hz

configuration	degree	degree	r (ft)						
		0	2	3	4	5	6	7	
			0	0	x	x			
	-90	90	2	4	6	8	10	12	
			0	0	x	x	x	x	
a	-125	45	2	3	4	5	6		
			0	0	0	x	x		
b	-60	45	2	3	4	5	6		
			0	0	0	x	x		
c	-90	45	2	3	4	5	6		
			0	0	0	x	x		
d	90	45	2	3	4	5	6	7	8
			0	0	0	x	x	x	x
e	30	45	2	3	4	5	6		
			0	0	0	0	x		
f	120	45	2	3	4	5	6	7	
			0	0	0	0	x	x	
g	180	45	2	3	4	5			
			0	0	0	x			
h	0	45	2	3					
			0	0					
	0	90	2	3	4	5	6	7	
			0	0	0	x	x	x	
	90	90	2	3	4	5	6		
			0	0	x	x	x		
	180	90	2	3	4	5			
			0	0	0	x			

Fig. 14 comparison of results obtained in M.I.T. E.E. anechoic chamber with those in tunnel chamber

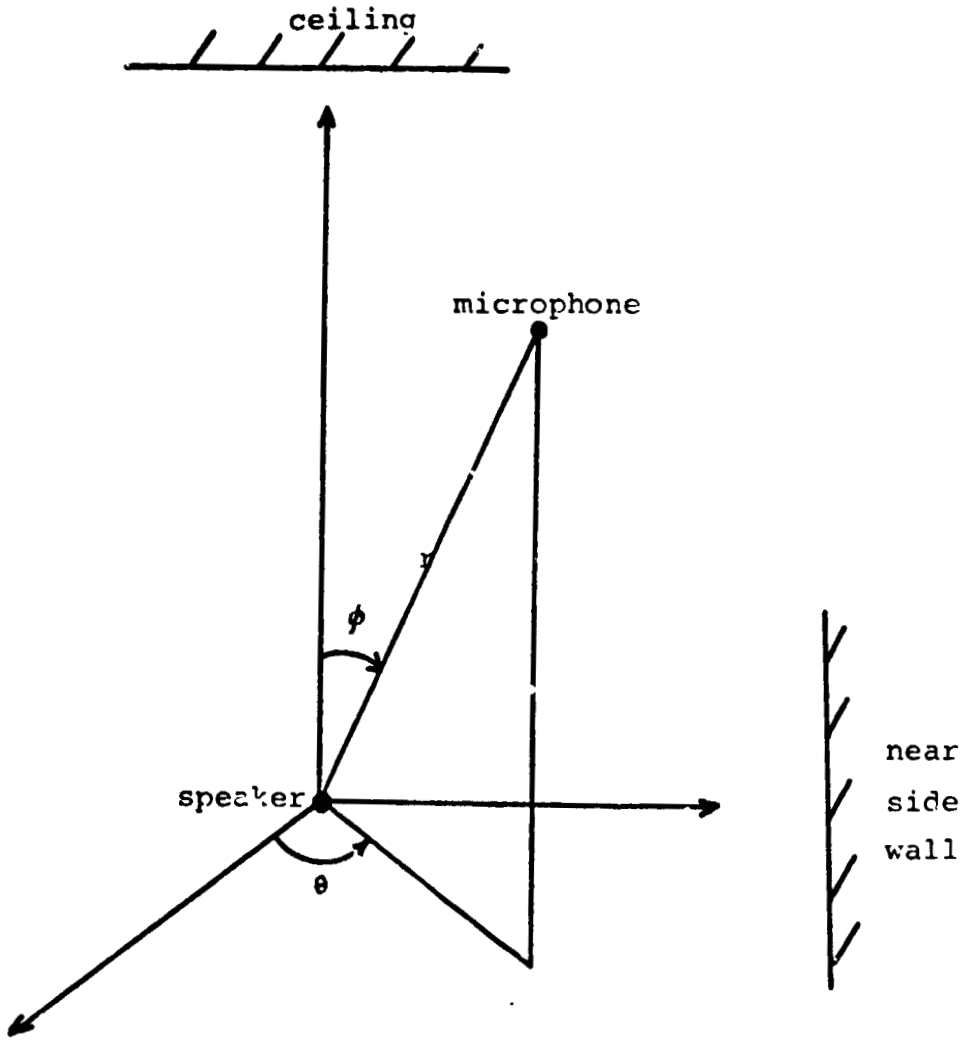

The speaker is mounted at rotor shaft tip location

Fig. 15 coordinate system

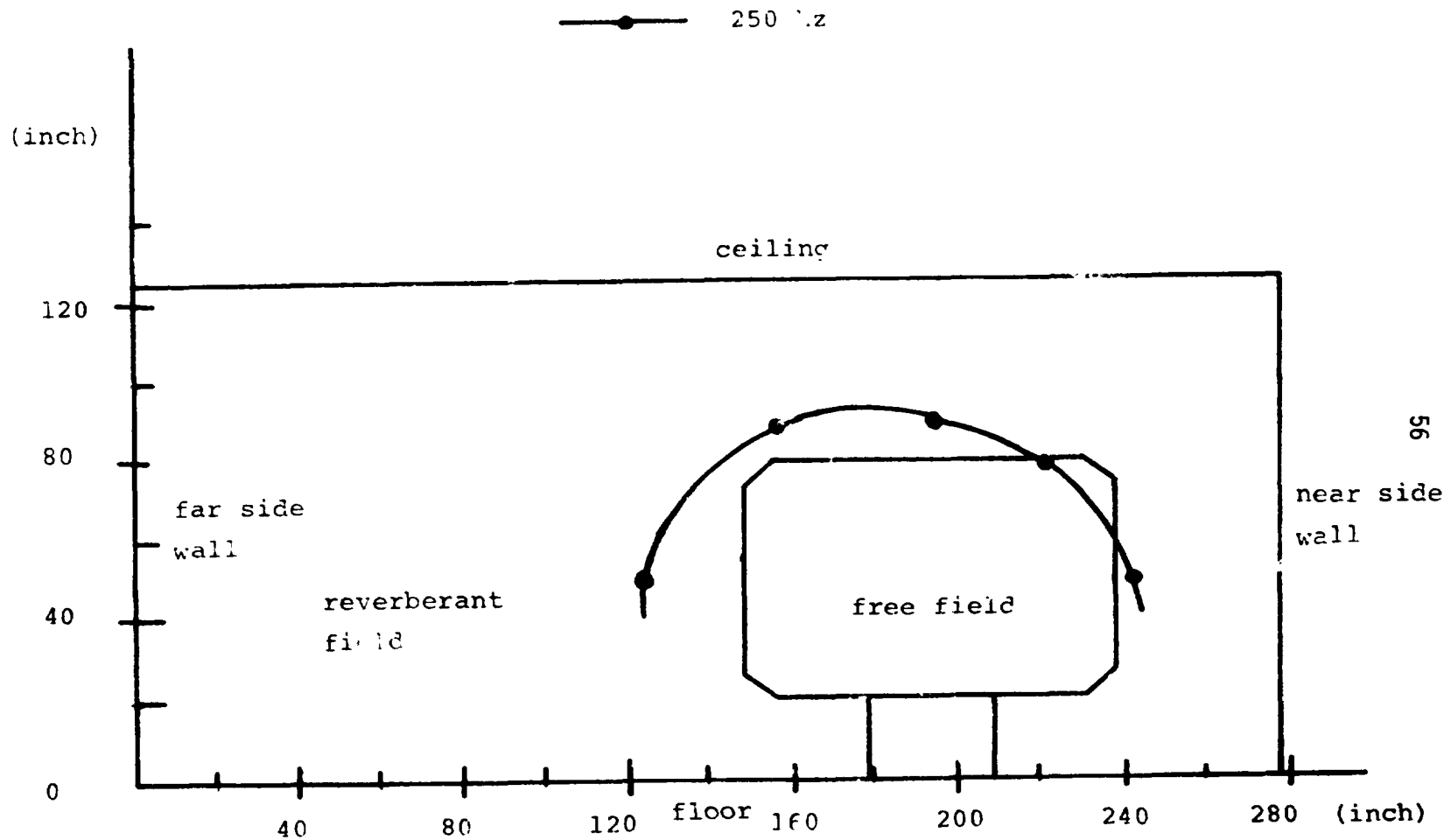

Fig. 16. the front view of acoustic free field before fiberglas blocks treatment

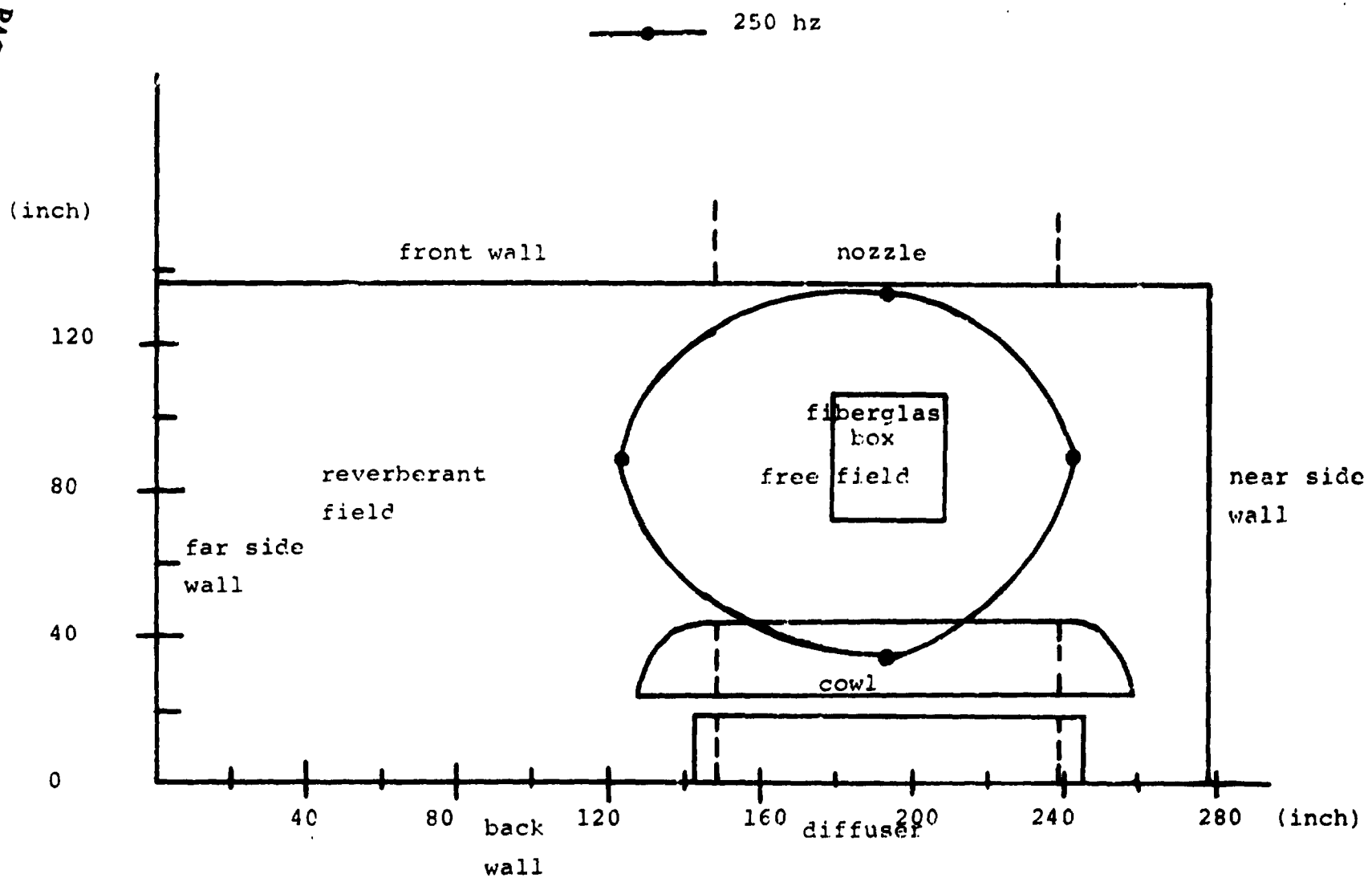

Fig. 17 the top view of acoustic free field before fiberglas blocks treatment

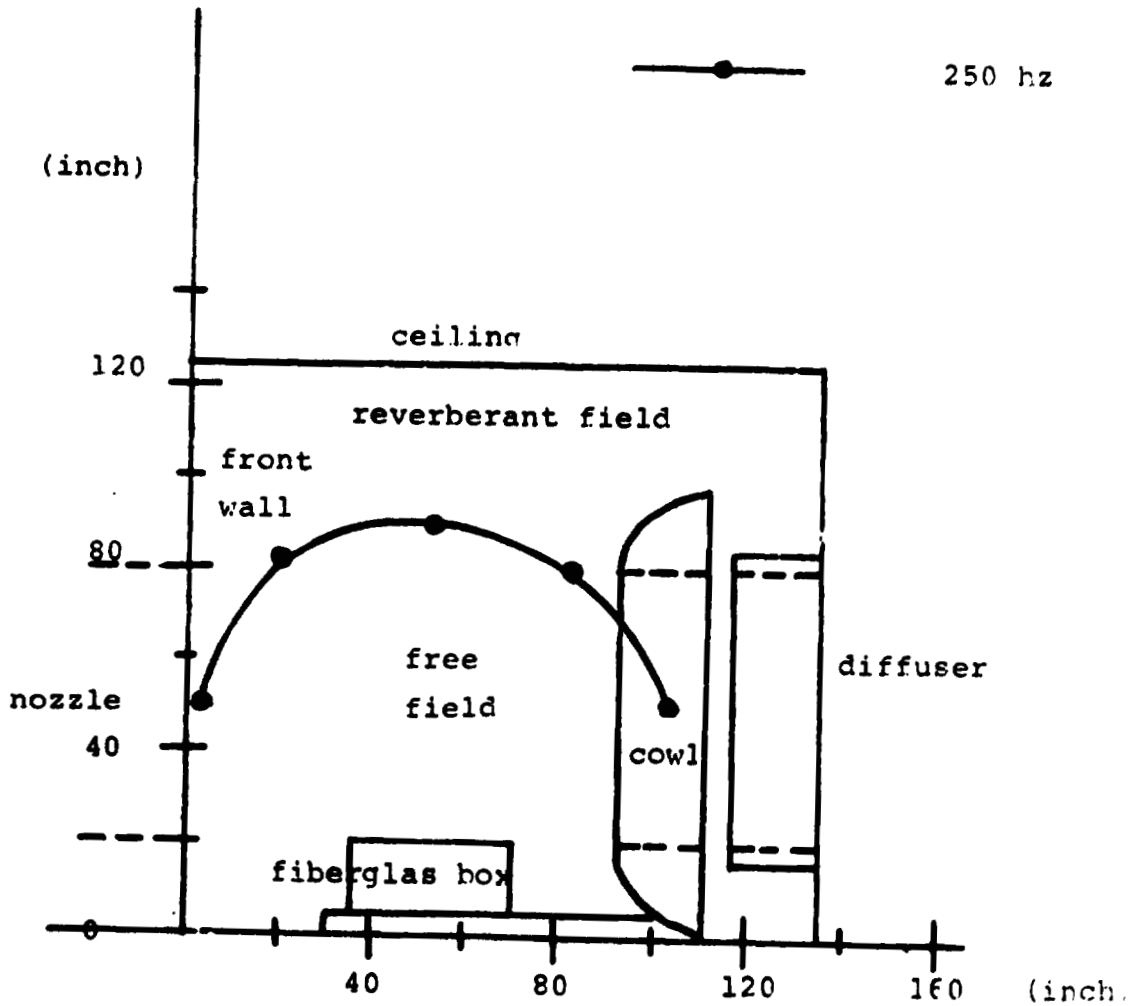

Fig. 18. the side view of acoustic free field before fiberg

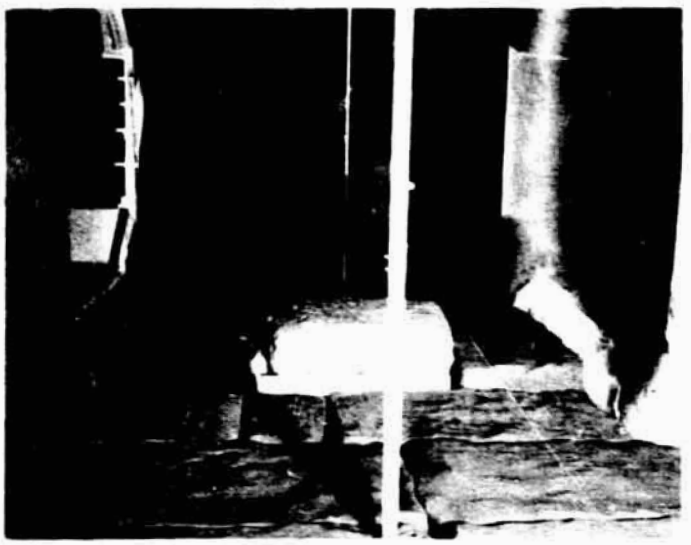

Fig. 19 View of test section in low noise acoustic wind tunnel after fiberglass blocks treatment

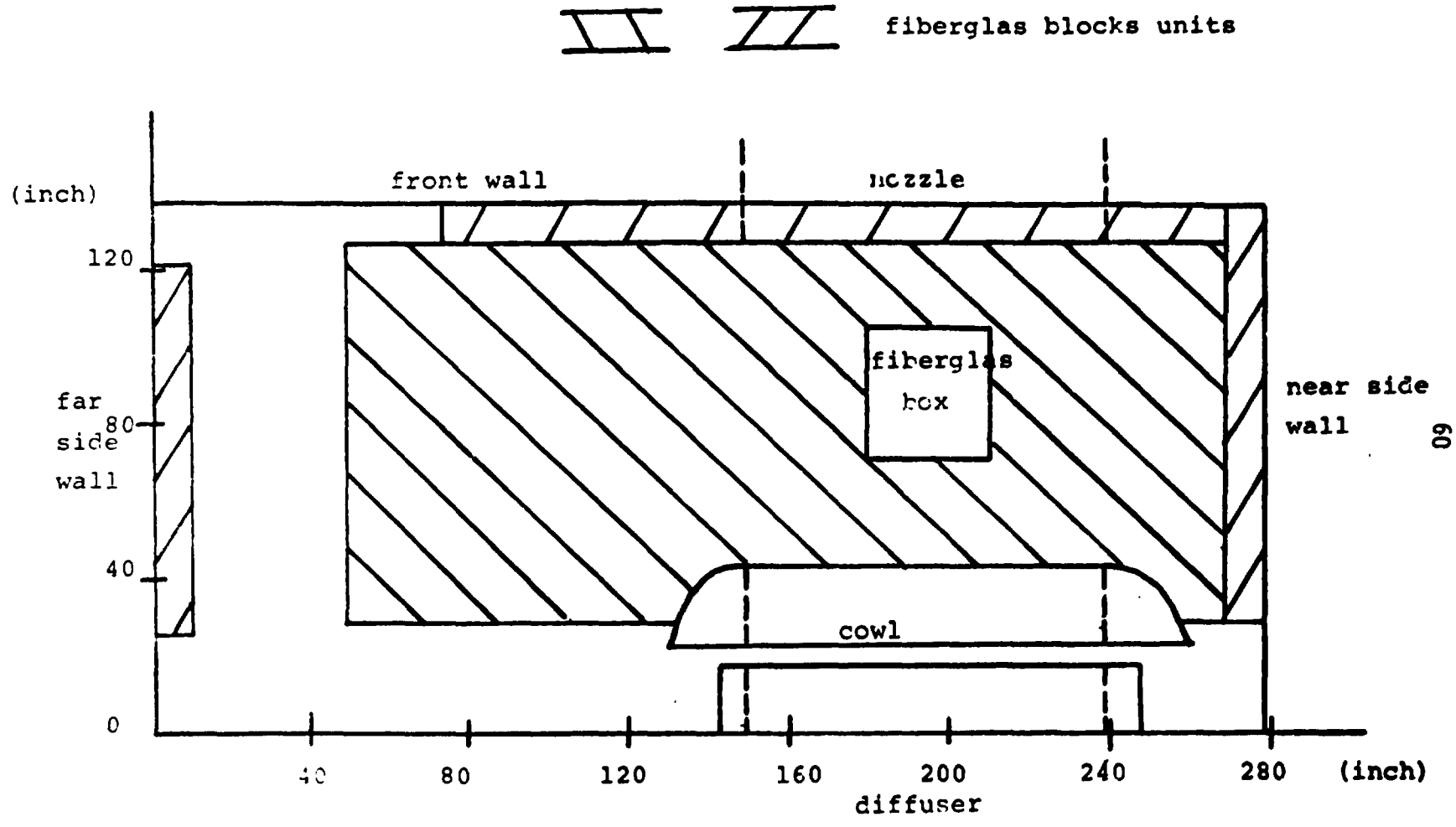

Fig. 20 the top view of fiberglas blocks treated chamber

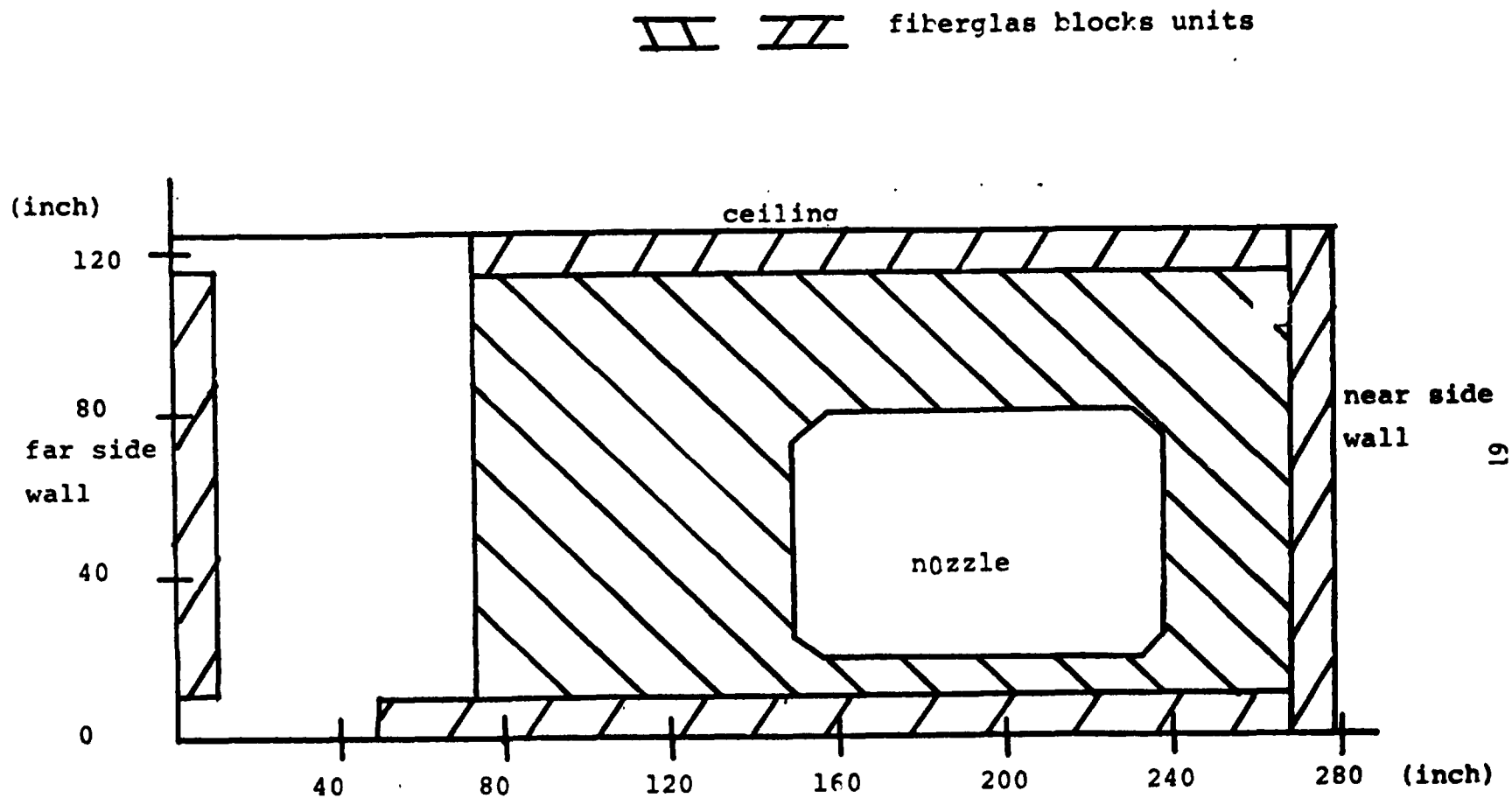

Fig. 21 the front view of fiberglas blocks treated chamber

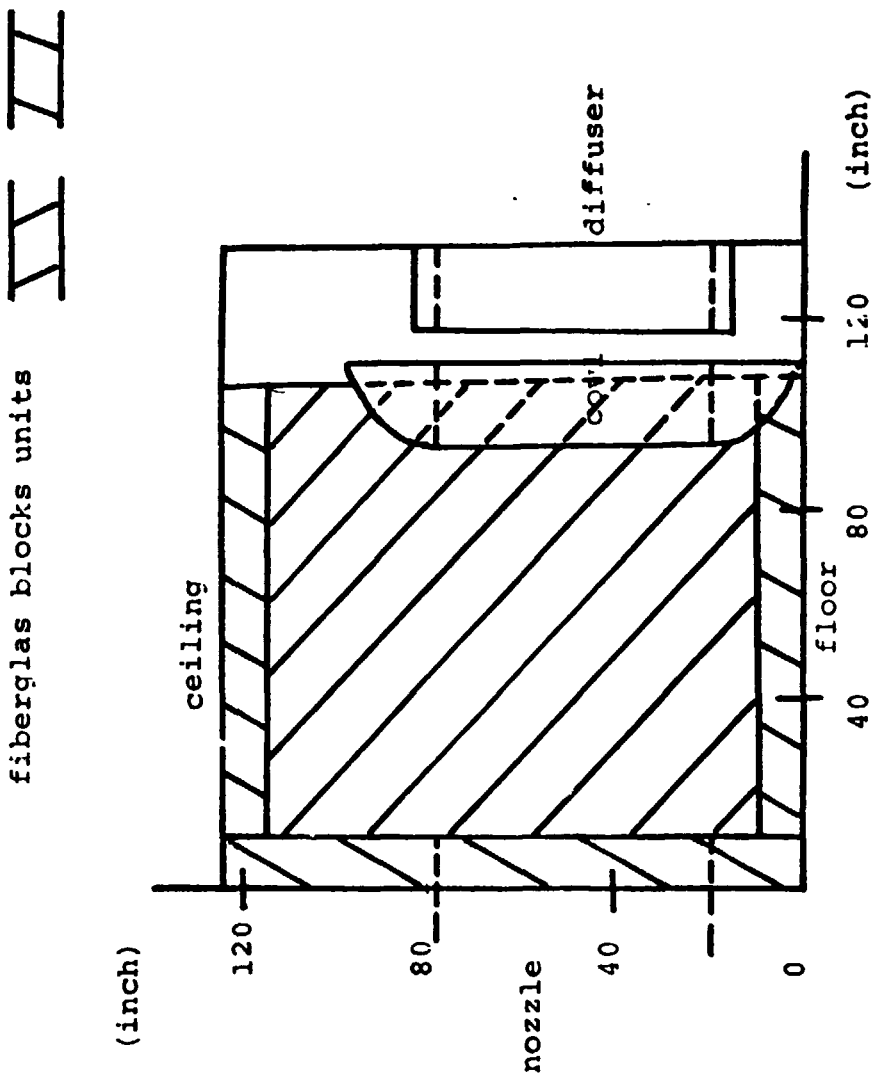

Fig. 22 the side view of fiberglas blocks treated chamber

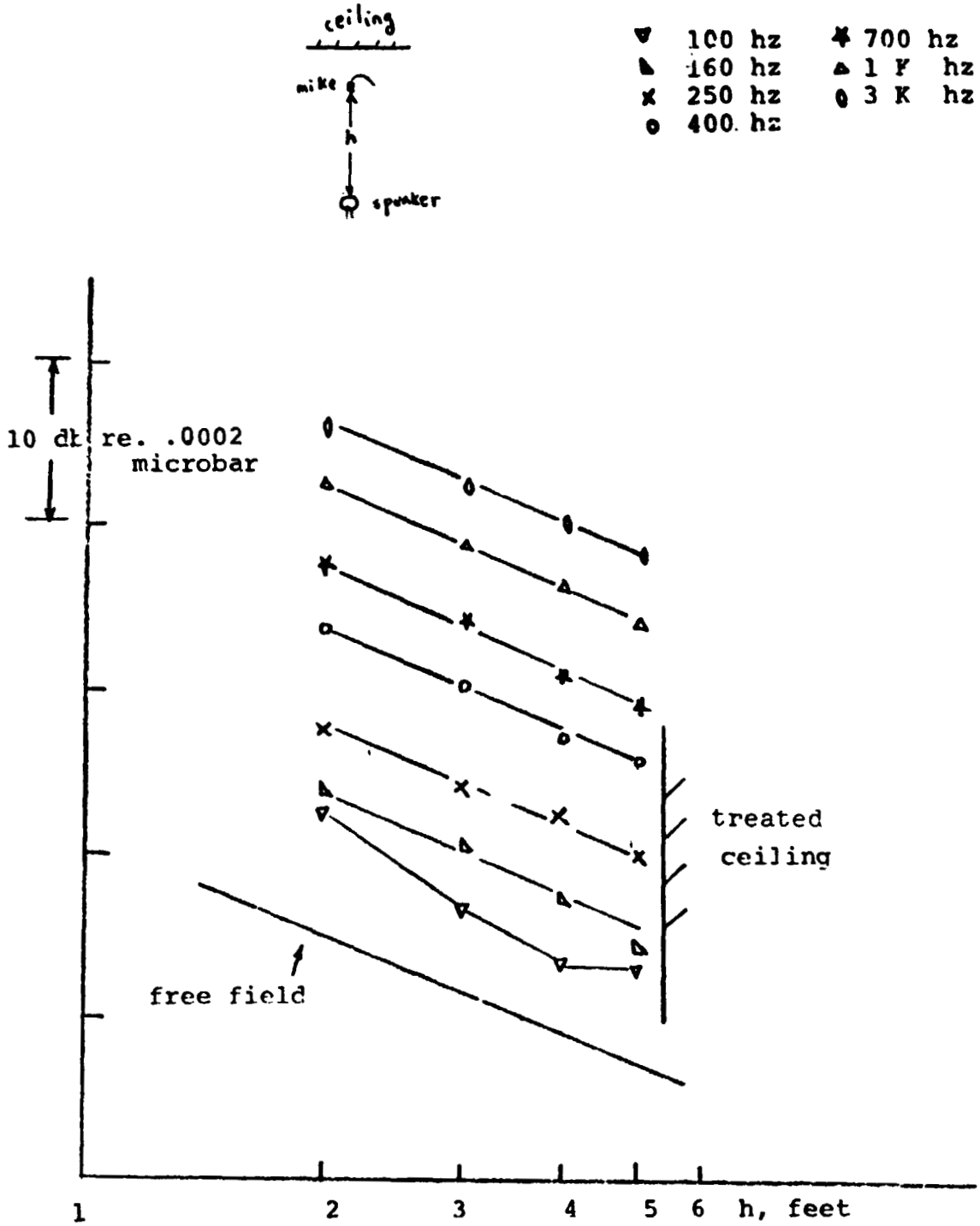

Fig. 23 Acoustic property of the chambers ceiling. The noise source is mounted at the rotor hub location. Measurements made in the treated chamber.

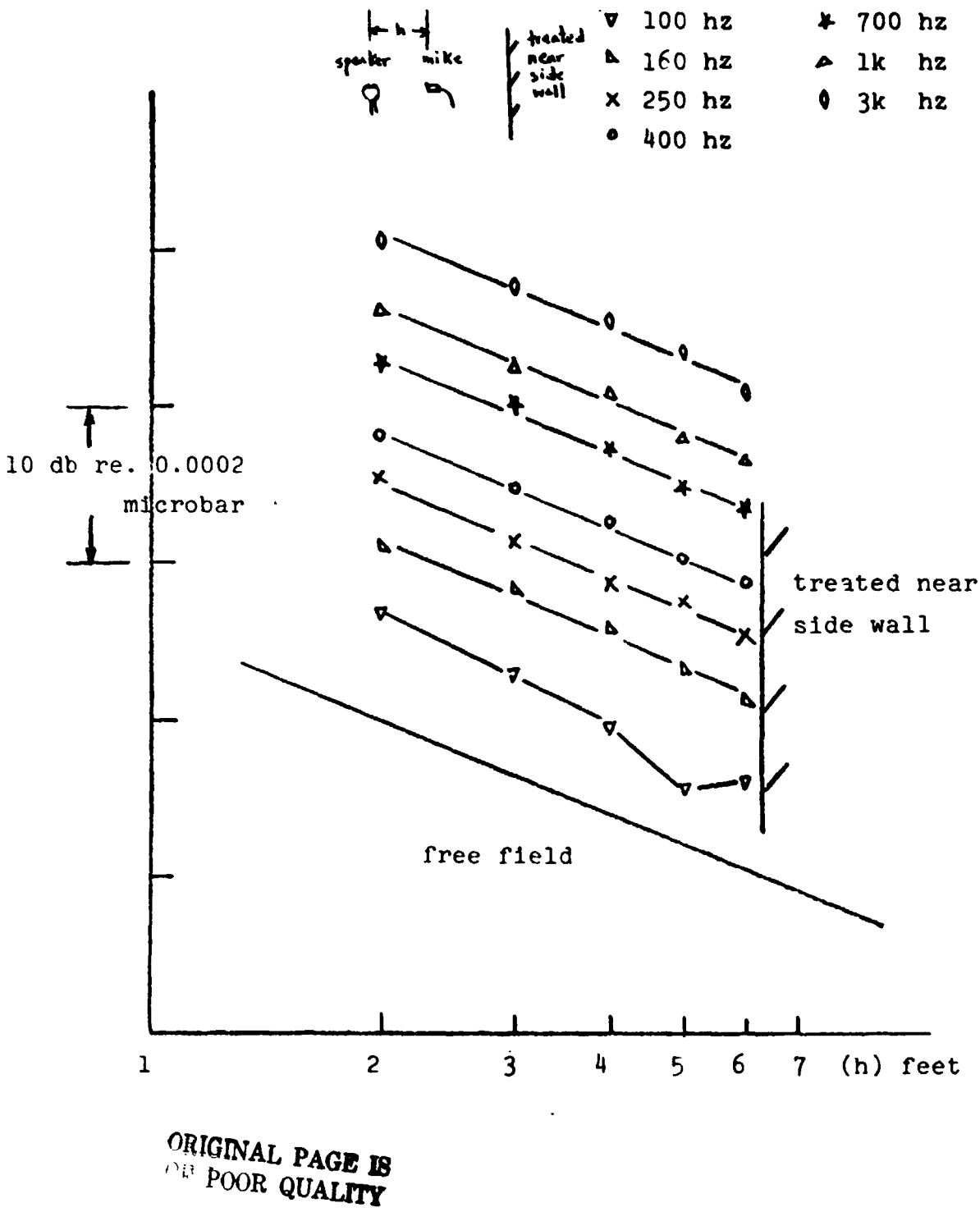

Fig. 24 Acoustic property of the near side wall of the treated chamber. The noise source is mounted at the rotor hub location.

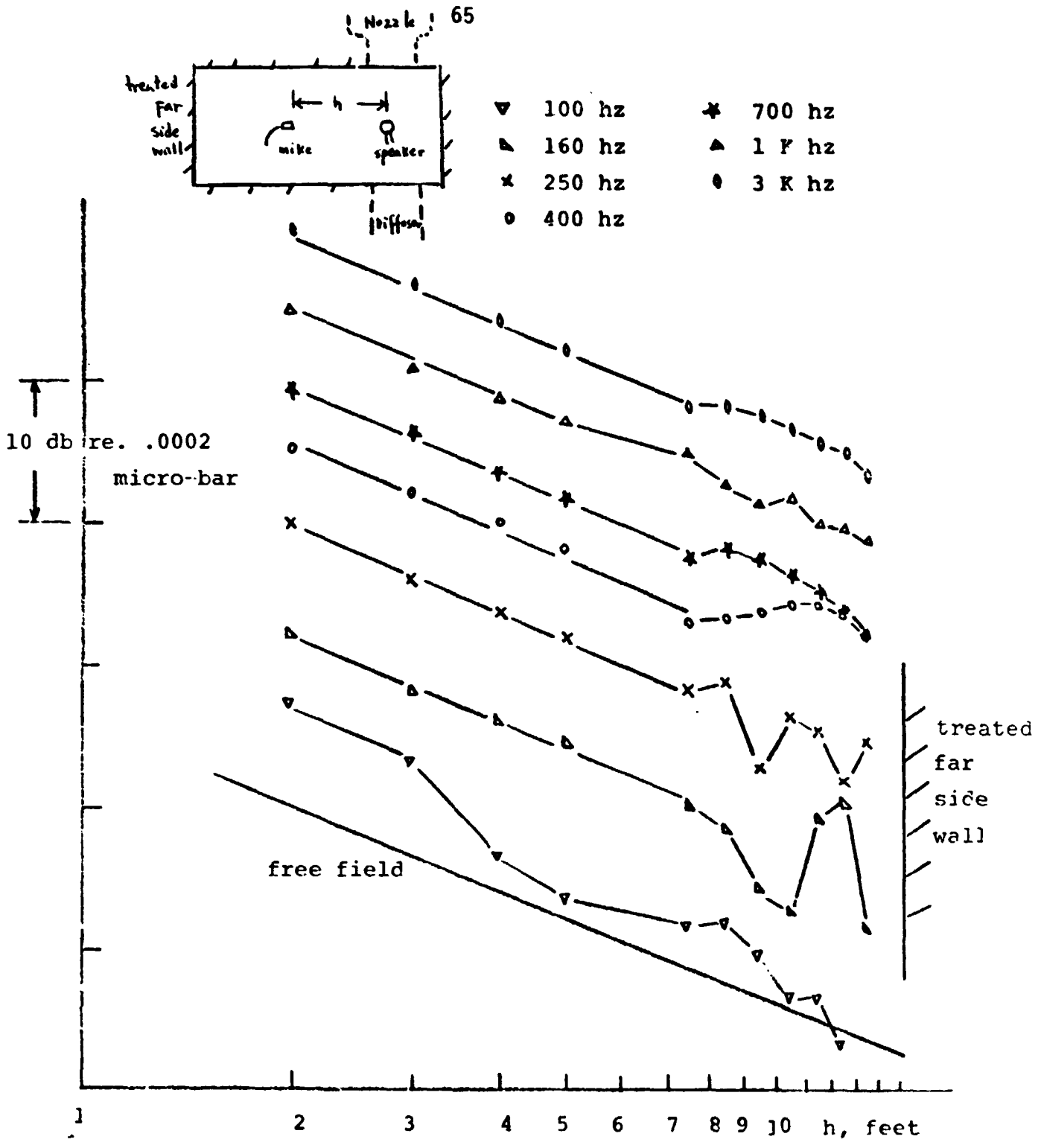

Fig. 25 Acoustic property of the chamber far side wall of treated chamber. The noise source is mounted at the rotor hub location.

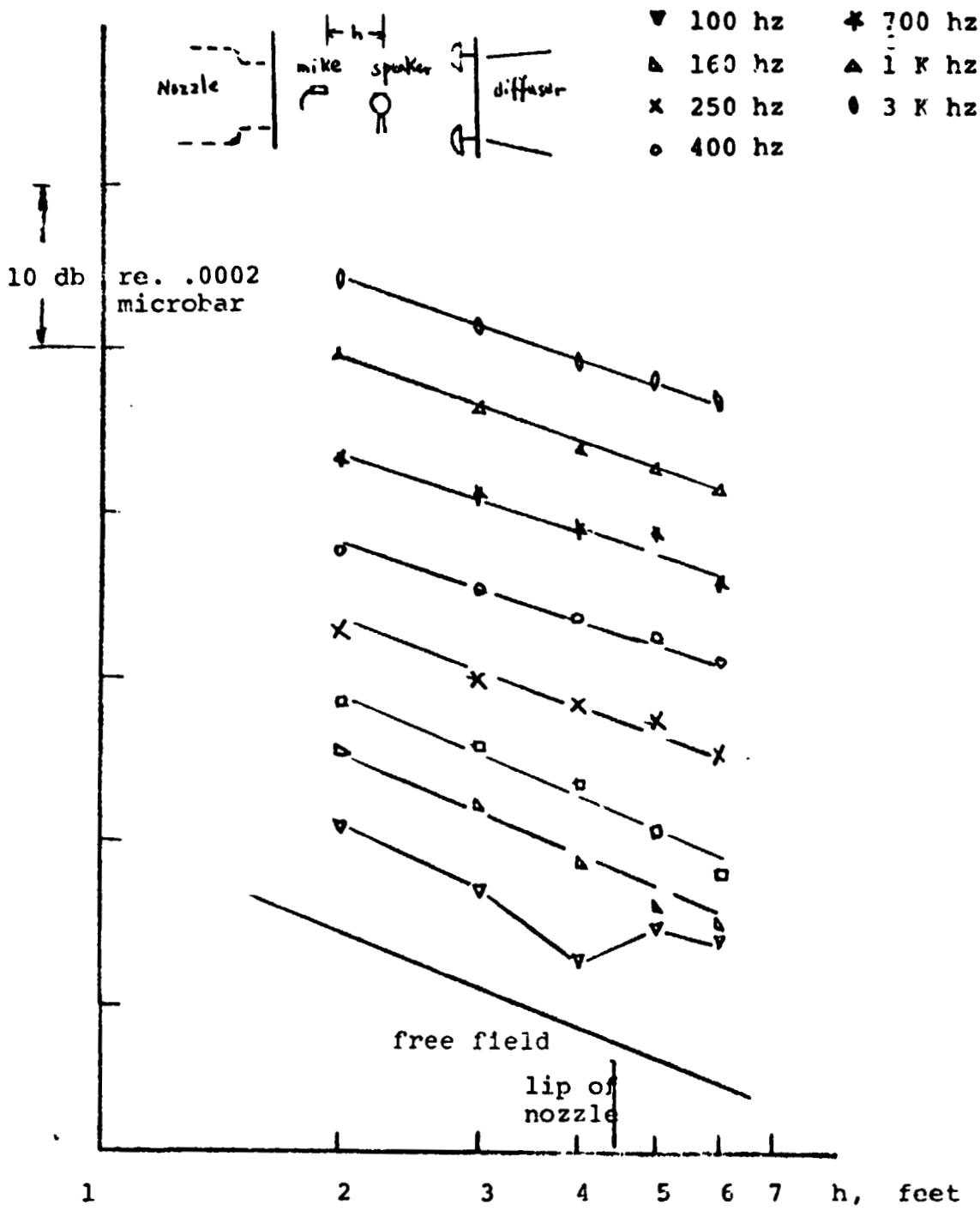

Fig. 26 Acoustic property of the nozzle section of the treated chamber. The noise source is mounted at the rotor hub location.

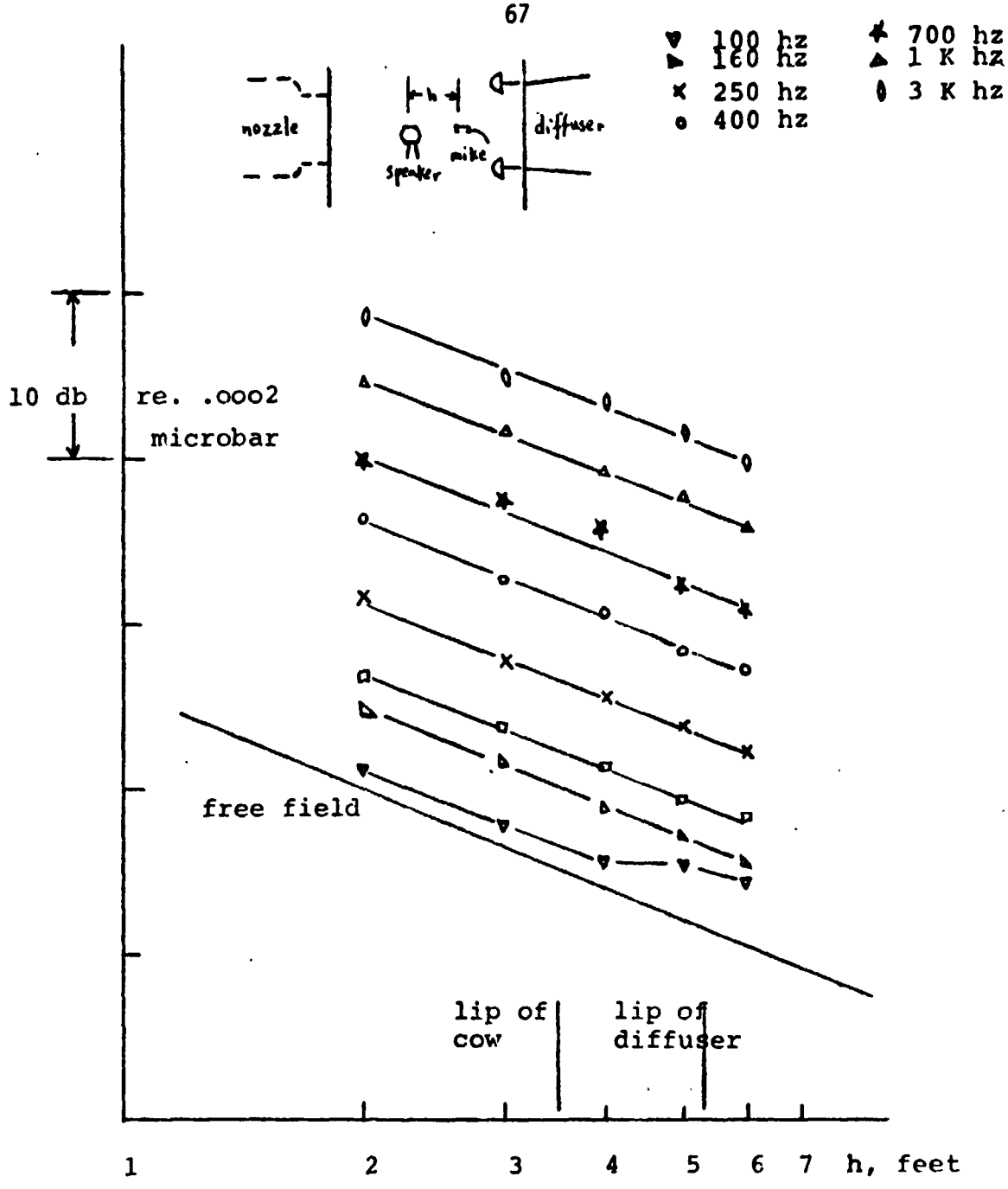

Fig. 27 Acoustic property of the diffuser section of treated chamber. The noise source is mounted at the rotor hub location.

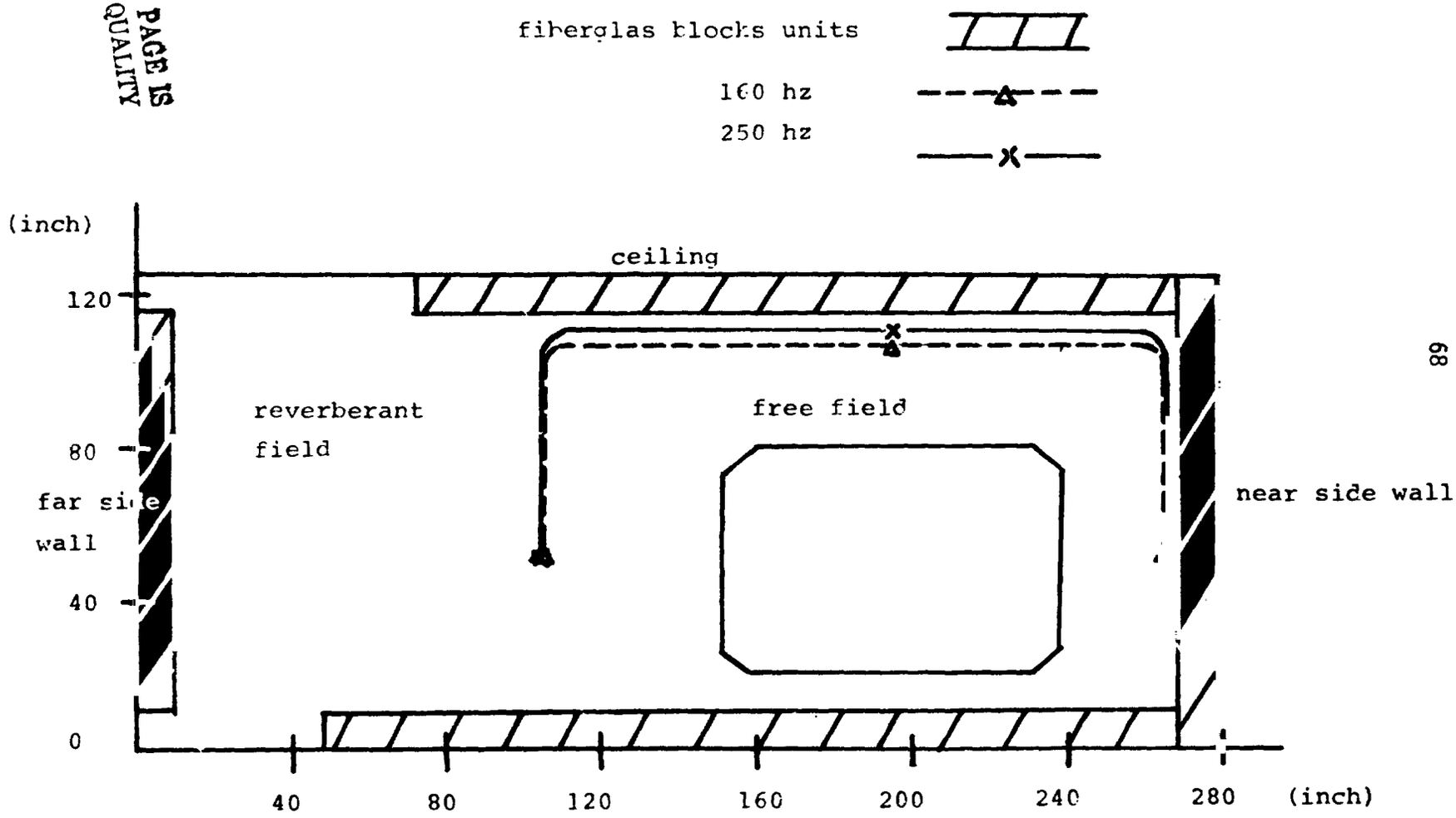

Fig. 28 · the front view of acoustic free field after fiberglas blocks treatment

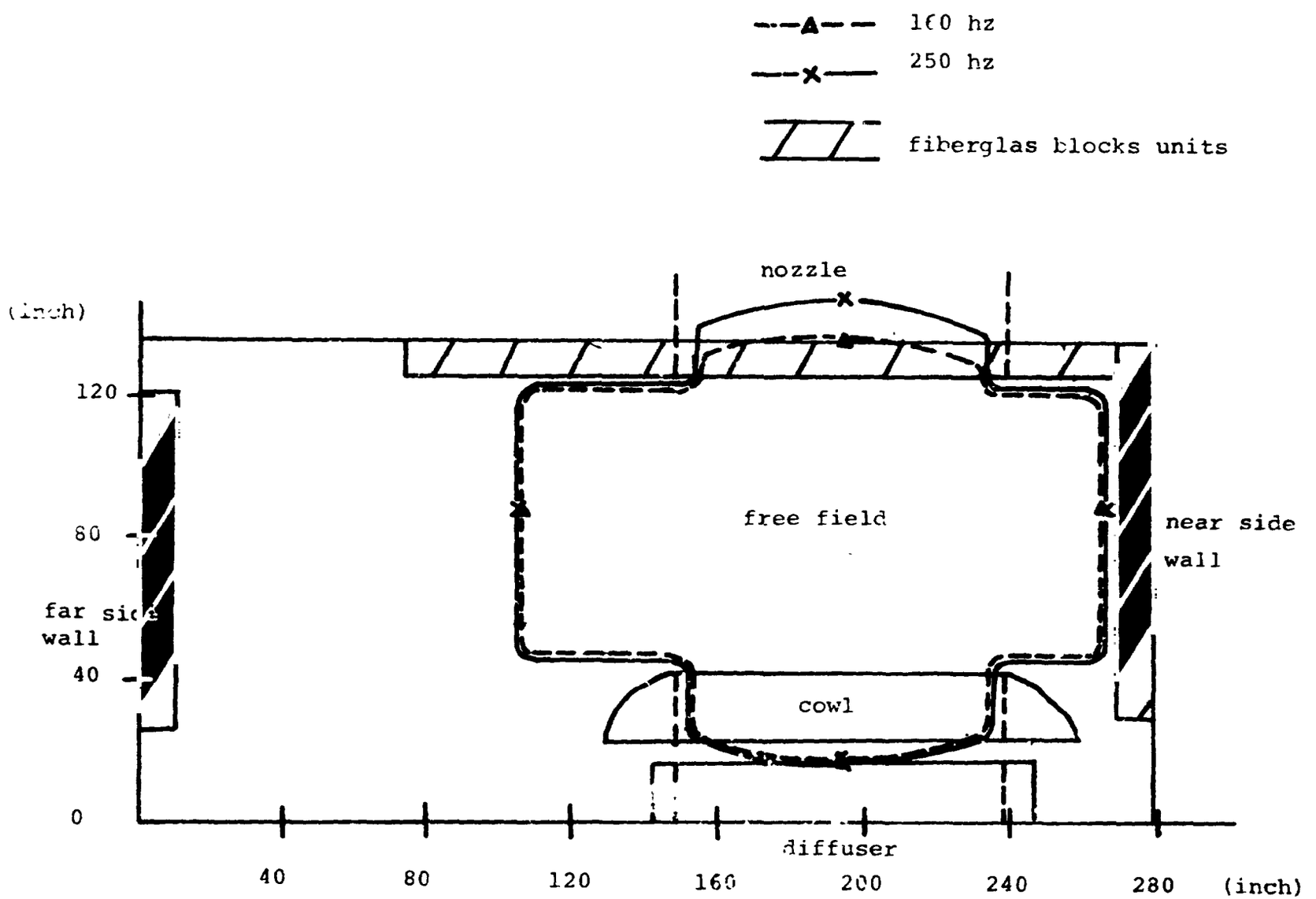

Fig. 29. the top view of acoustic free field after fiberglas blocks treatment

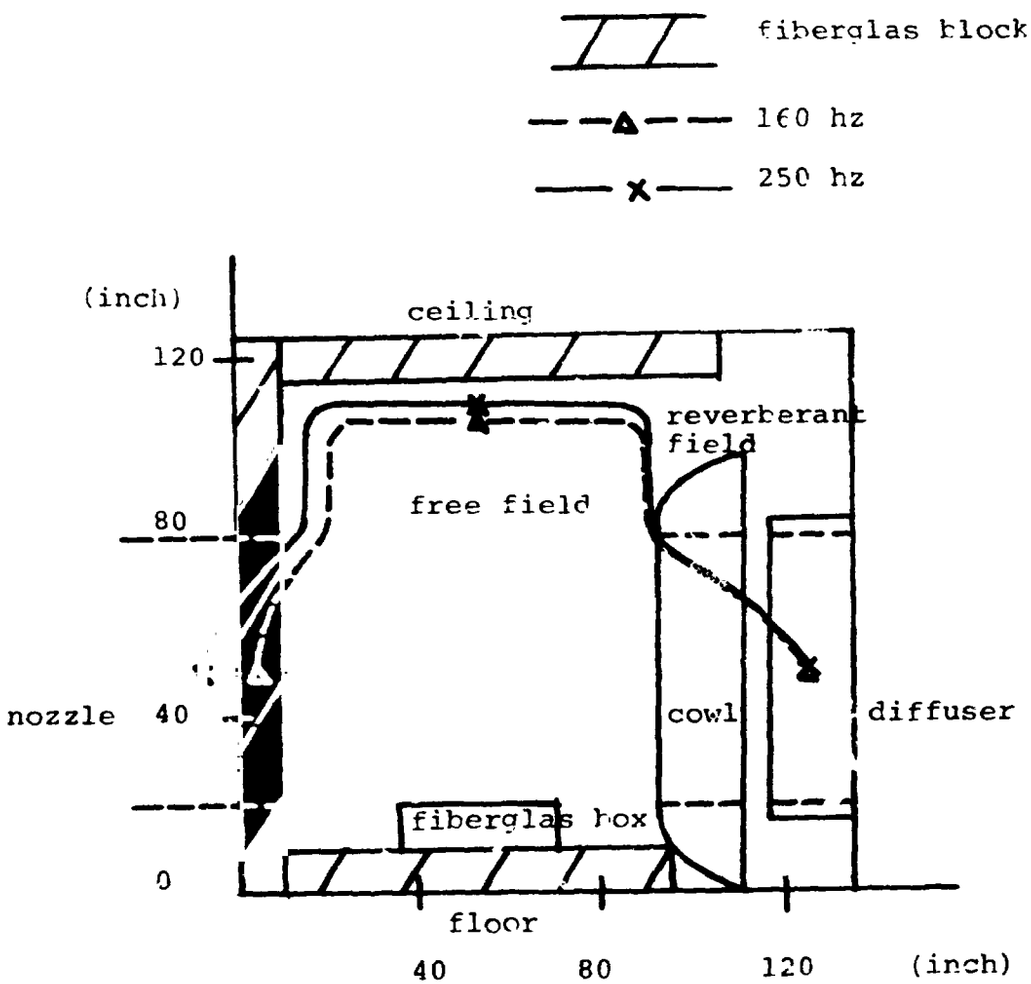

Fig. 30. the side view if acoustic free field after fiberglas blocks treatments

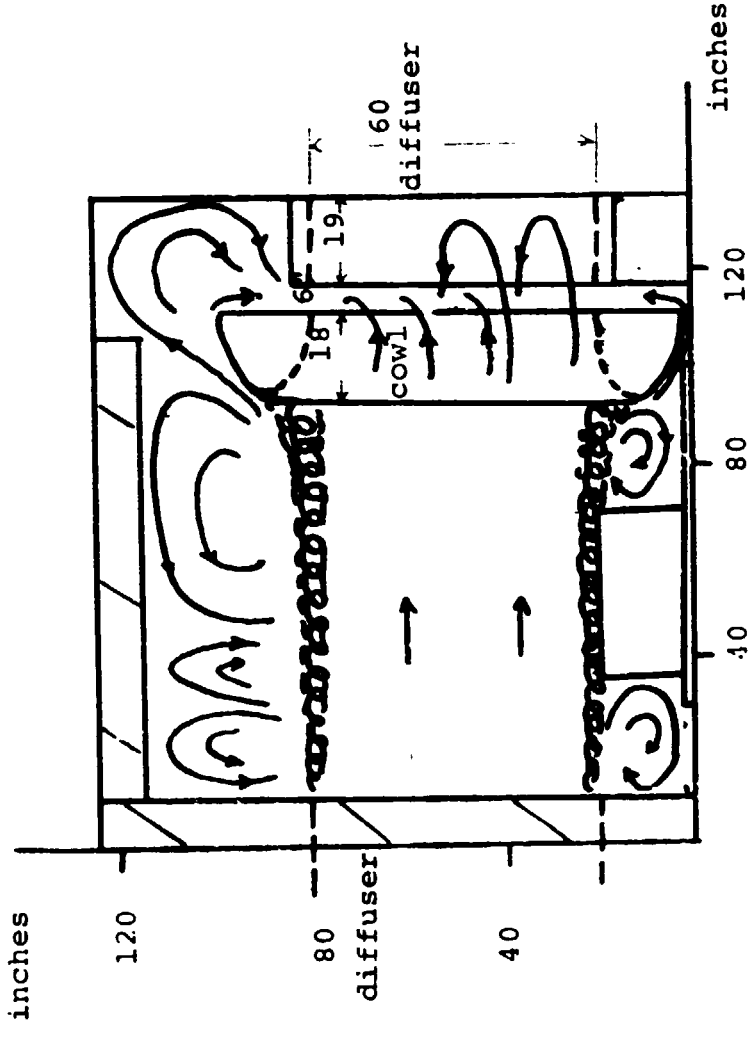

Fig. 32 The side view of the flow field

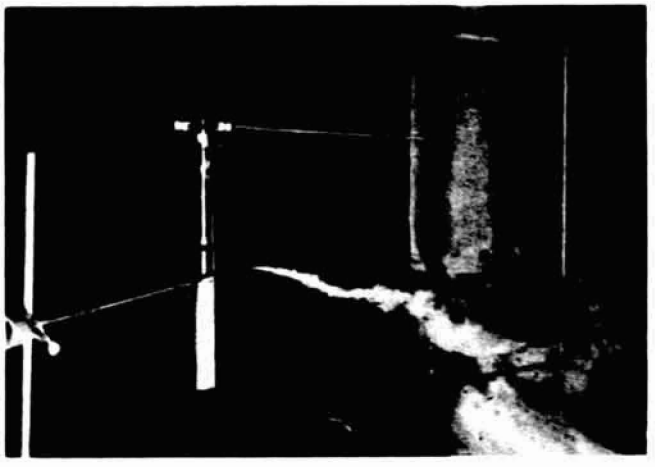

Rotor: 400 rpm
Tunnel Speed: 276.3 fpm (3.14 mph)
Advance Ratio: 0.053

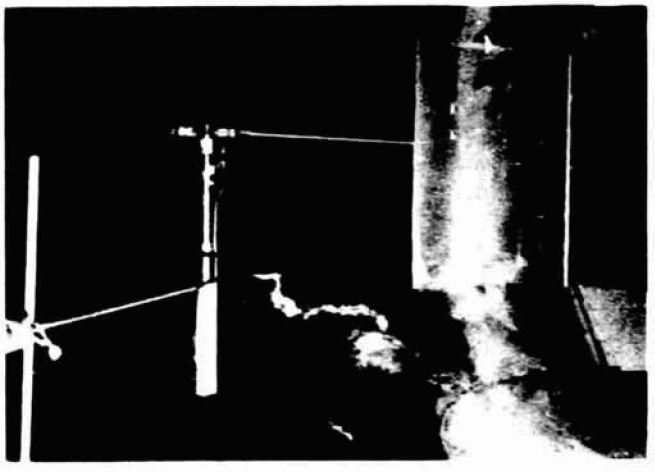

Rotor: 400 rpm
Tunnel Speed: 297.5 fpm (3.38 mph)
Advance Ratio: 0.057

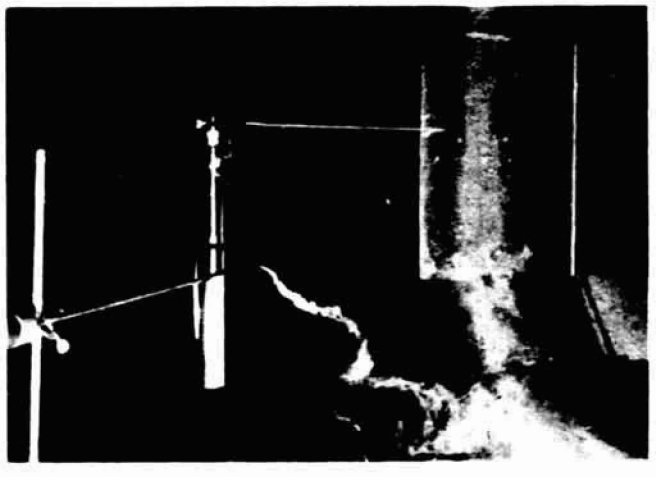

Rotor: 300 rpm
Tunnel Speed: 276.3 fpm (3.14 mph)
Advance Ratio: 0.070

Fig. 33 Flow visualization of rotor flow

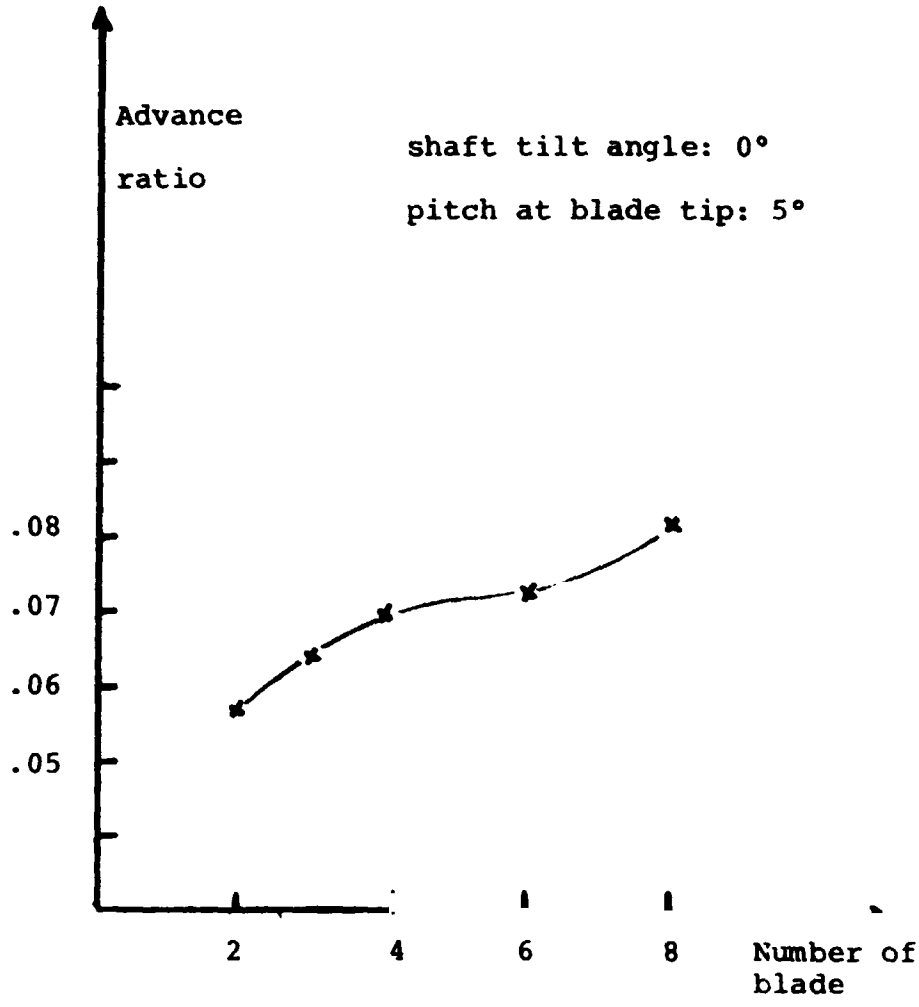

Fig. 34 The effect of blade number on minimum advance ratio without reingestion

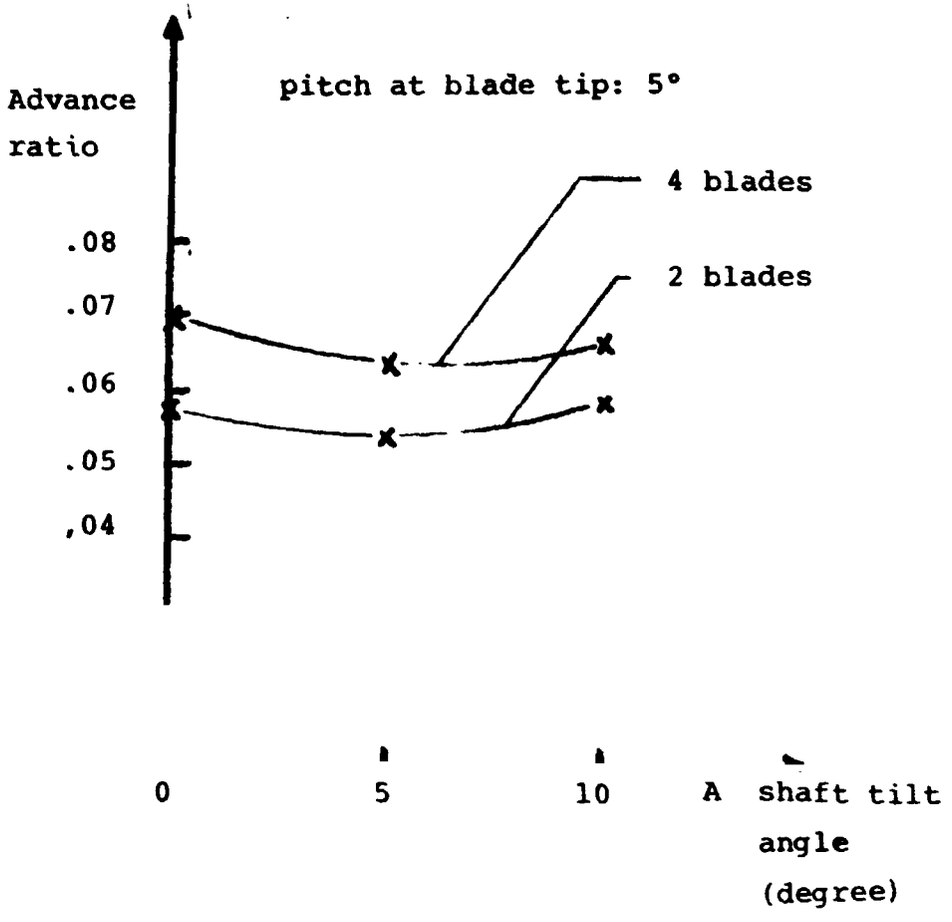

Fig. 35 The effect of shaft tilt angle on minimum advance ratio without reingestion

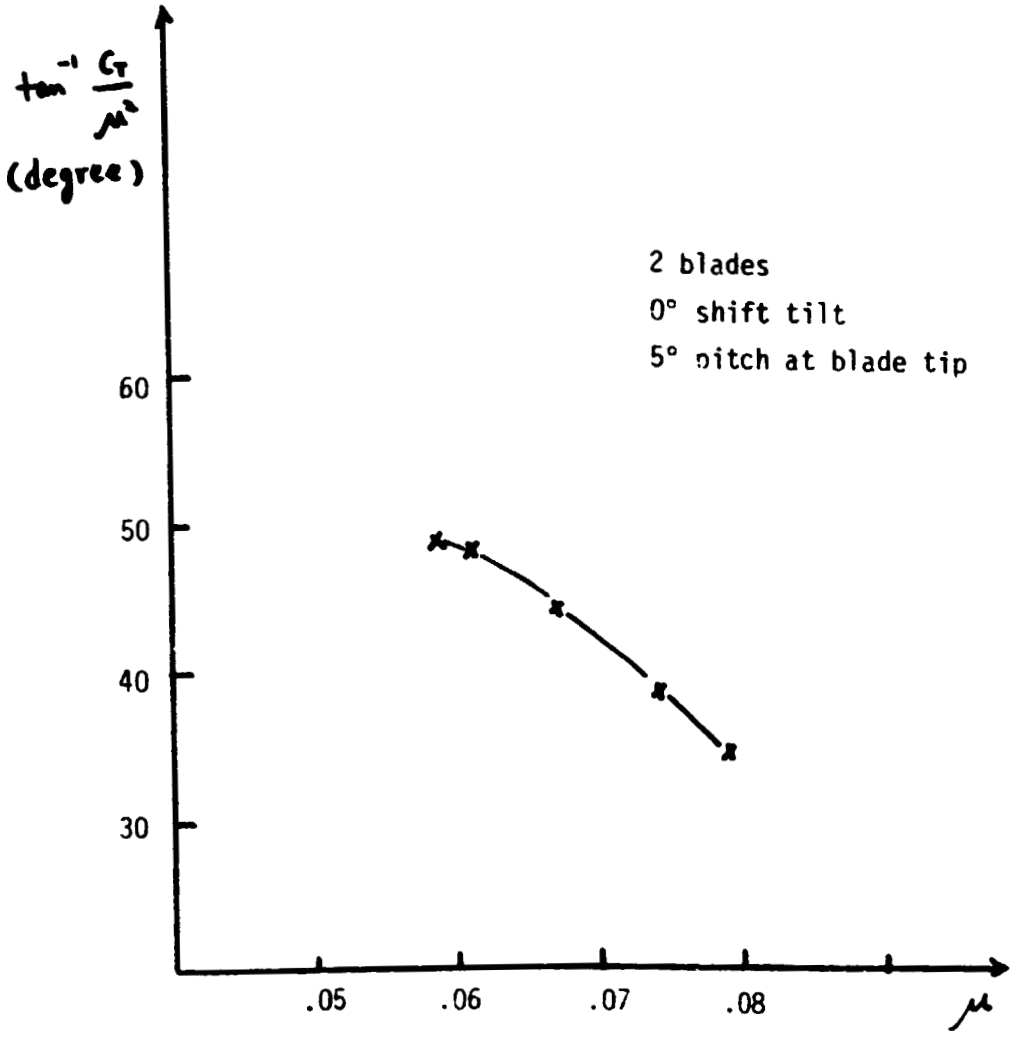

Fig. 36. The wake angle relative to the free stream velocity $\tan^{-1} \frac{C_t}{\mu^2}$ vs. μ.

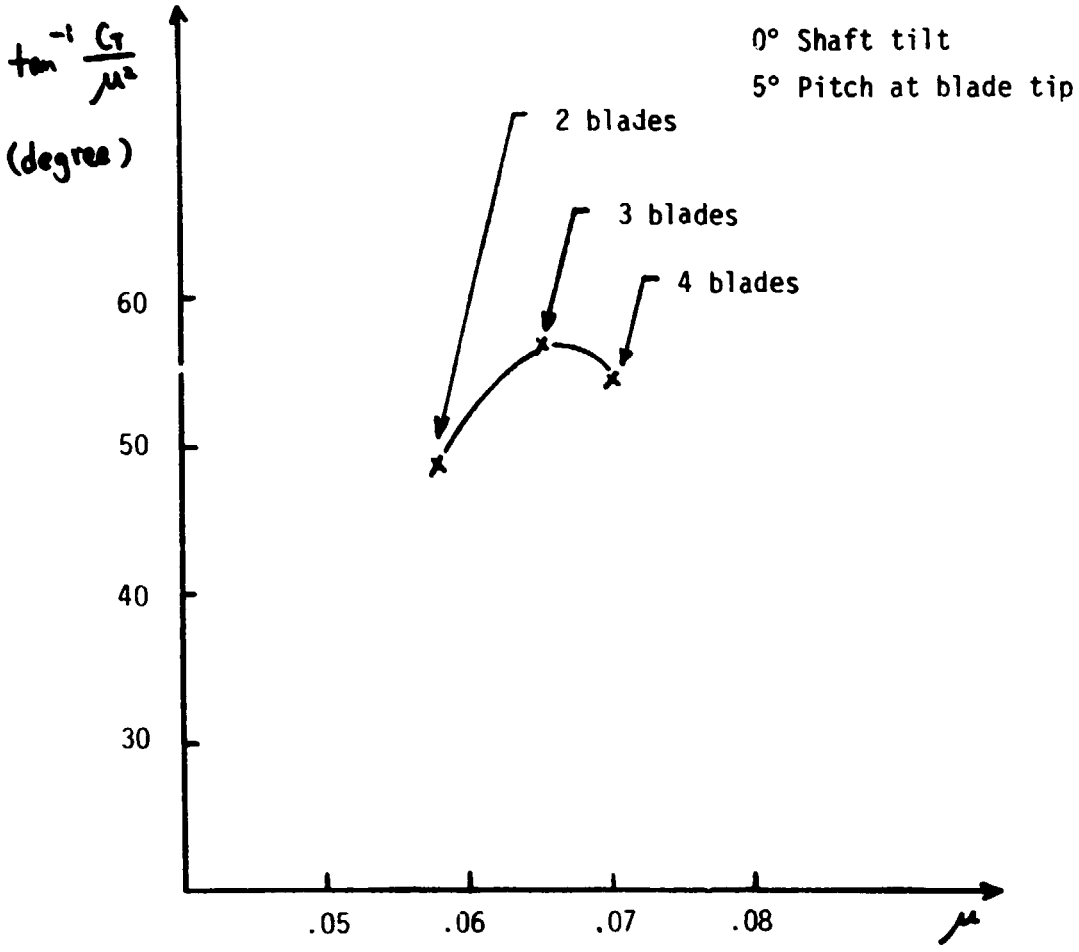

Fig. 37. The wake angle relative to the free stream vs the minimum advance ratio without reingestion

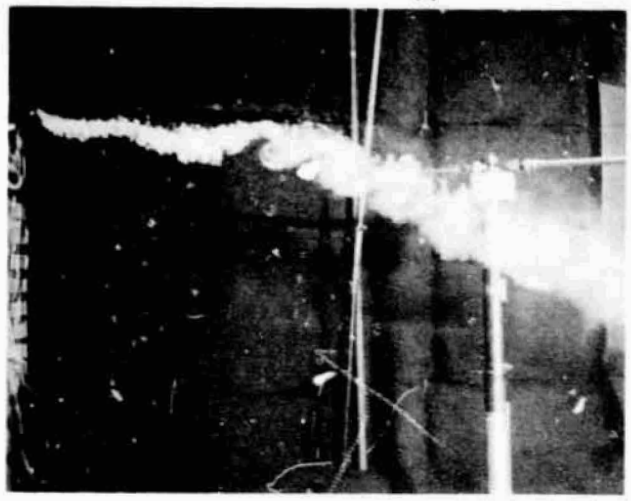

(a)

tip speed: 83.8 fps

tunnel speed: 283 fpm

advance ratio: .057

tilt angle: 0°

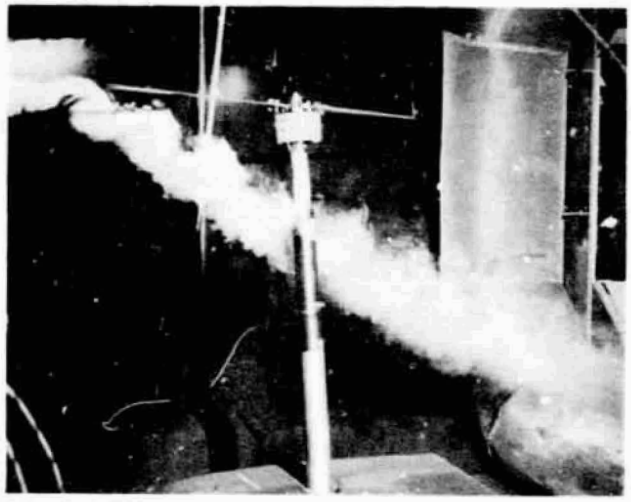

(b)

tip speed: 62.8 fps

tunnel speed : 203 fpm

advance ratio: .054

tilt angle: 5°

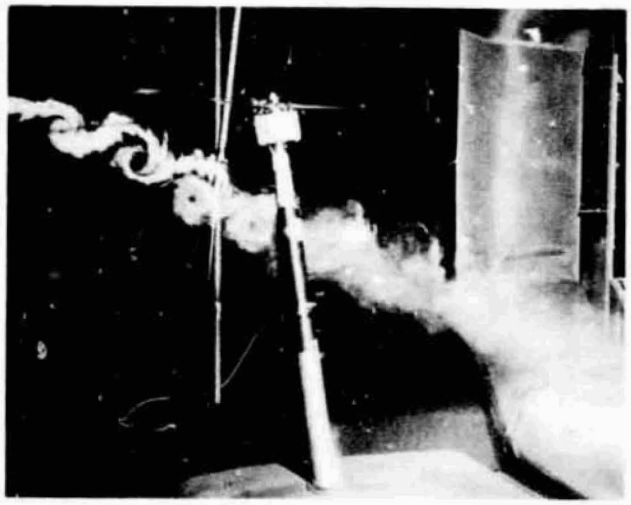

(c)

tip speed: 96.3 fps

tunnel speed : 340 fpm

advance ratio: .059

tilt angle: 10°

Fig. 38 Visualization of flow through rotor disk

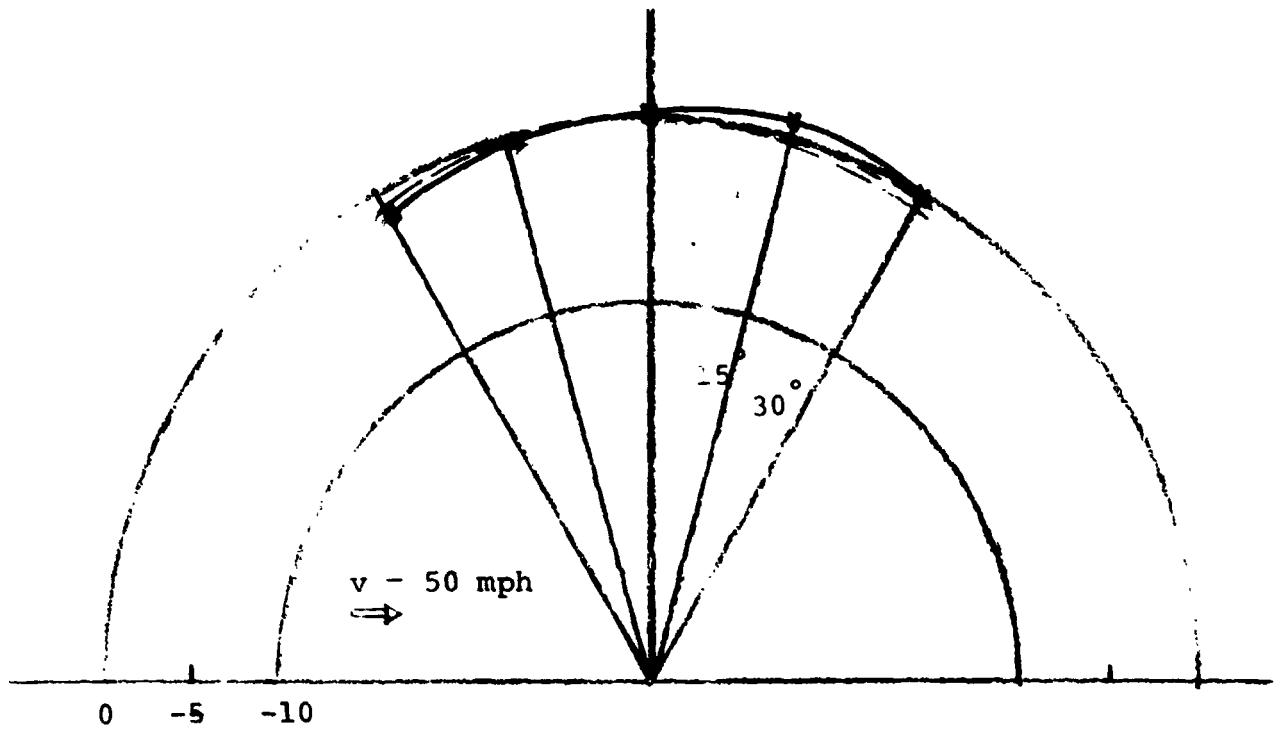

M = .067 theoretical dipole

M =.067 measured

M = 0 theoretical dipole

Aeolian tone source, diameter of cylinder d = .375

frequency = 550 Hz

Fig. 39 The Shear layer on vertical dipole

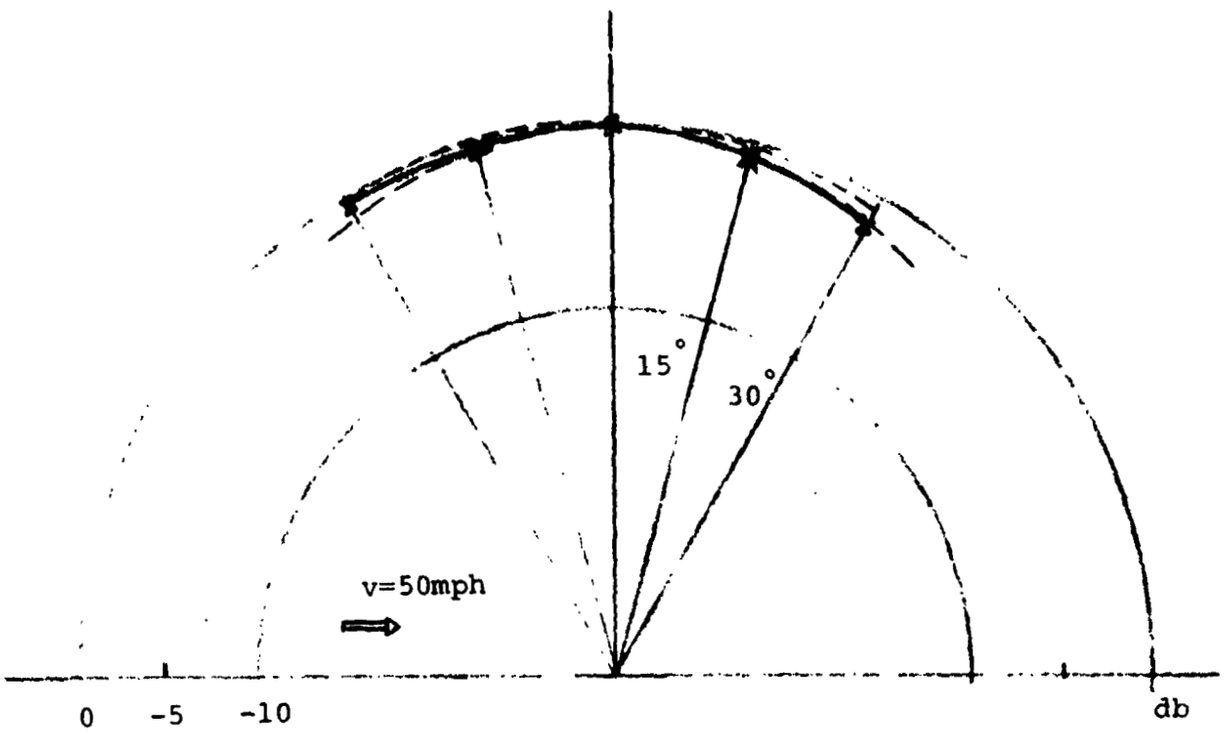

- - - M = .067 theoretical dipole

—x— M = .067 measured at distance 55 inches

-- --- M = 0 theoretical dipole

Aeolian tone source; diameter of cylinder d = .18

frequency = 1.1 K Hz

Fig. 40 Shear layer effect on vertical dipole

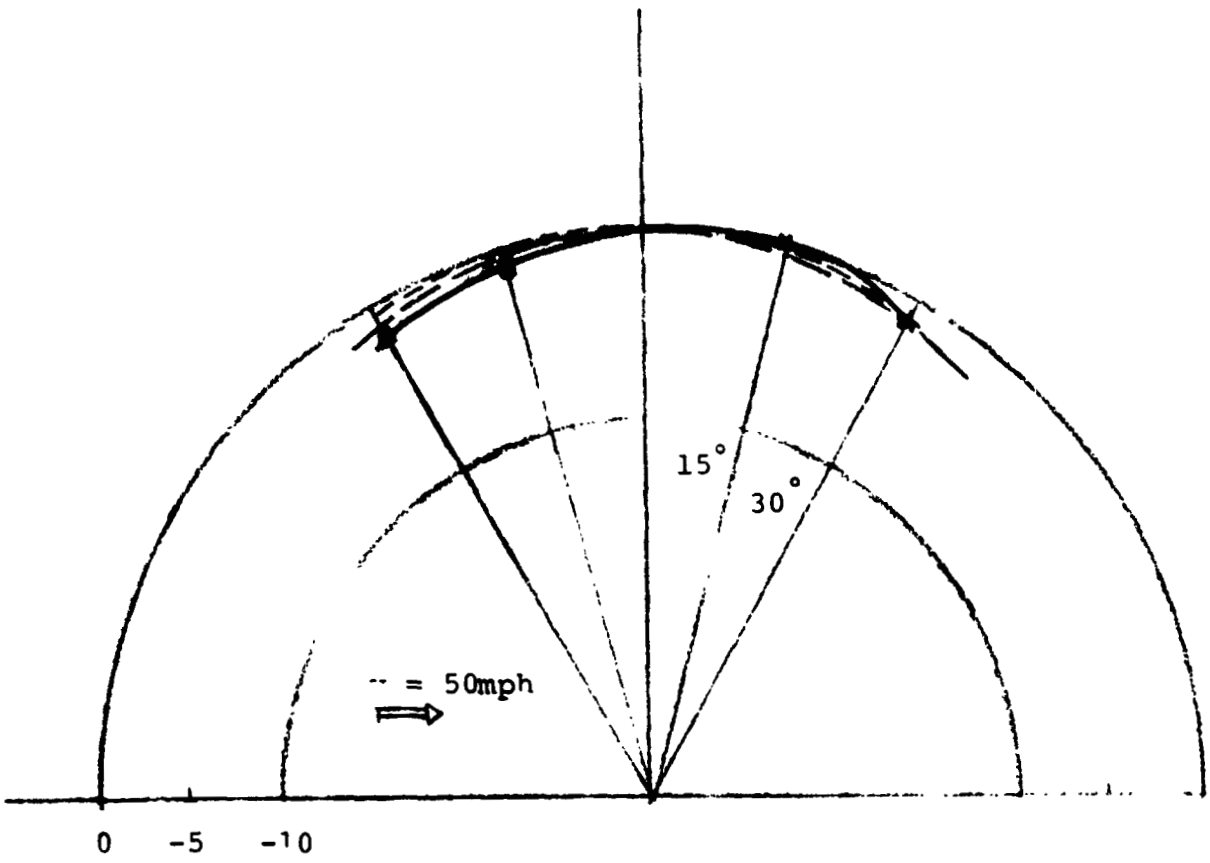

M = .067 theoretical dipole

M = .067 measured

M = 0 theoretical dipole

Aeolian tone source, diameter of cylinder d = .09 inch

frequency = 2.3 K Hz

Fig. 41 The Shear layer effect on vertical dipole

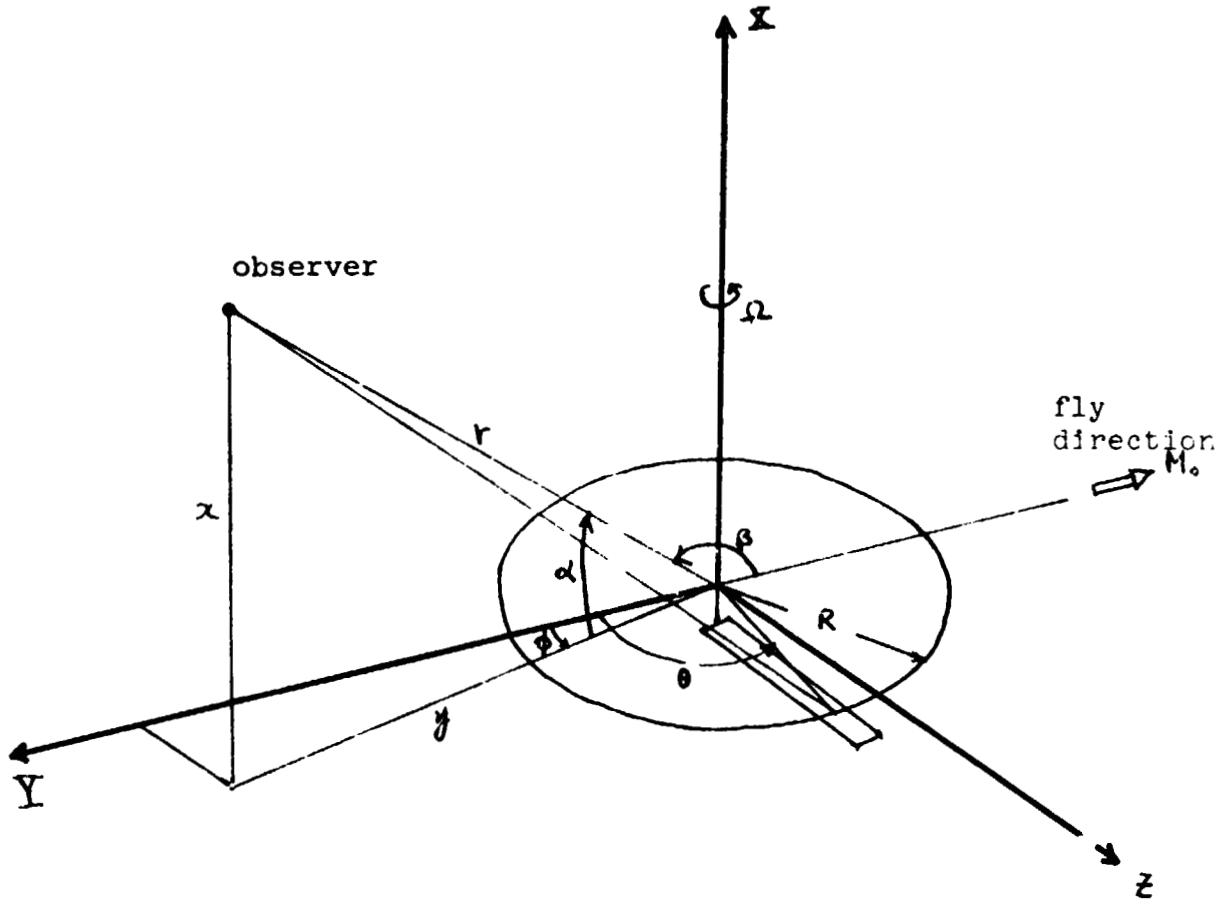

Fig. 42 . Coordinates used in Mach number scaling formula

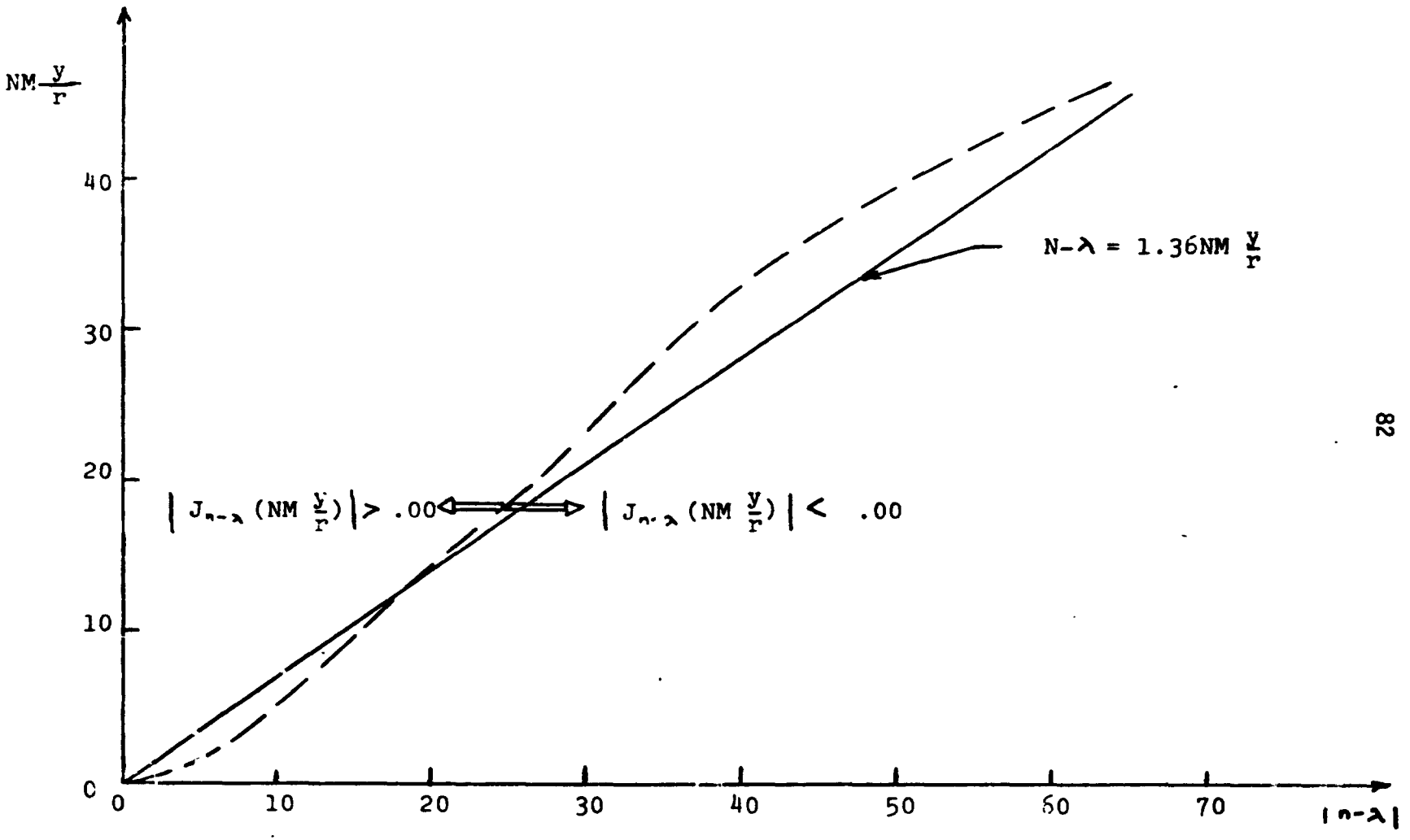

Fig 43 The curves dviding the magnitude of $J_{n-\lambda}(NM\frac{y}{r})$

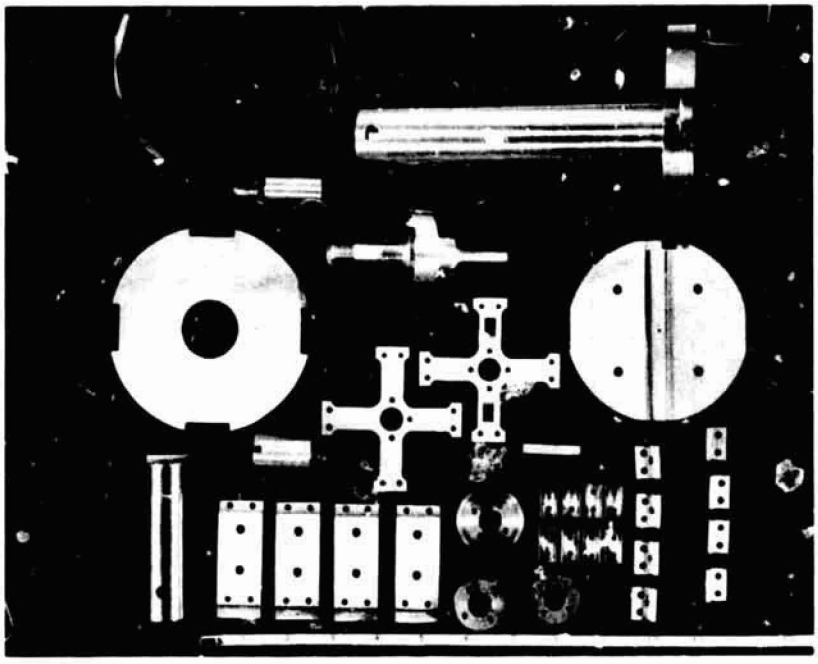

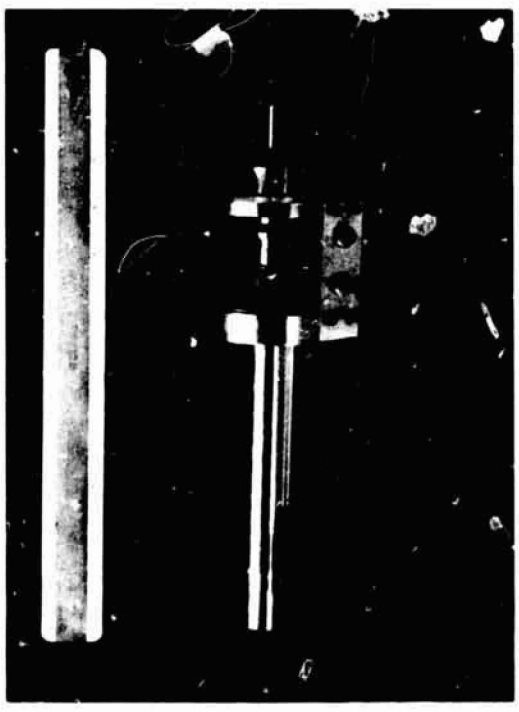

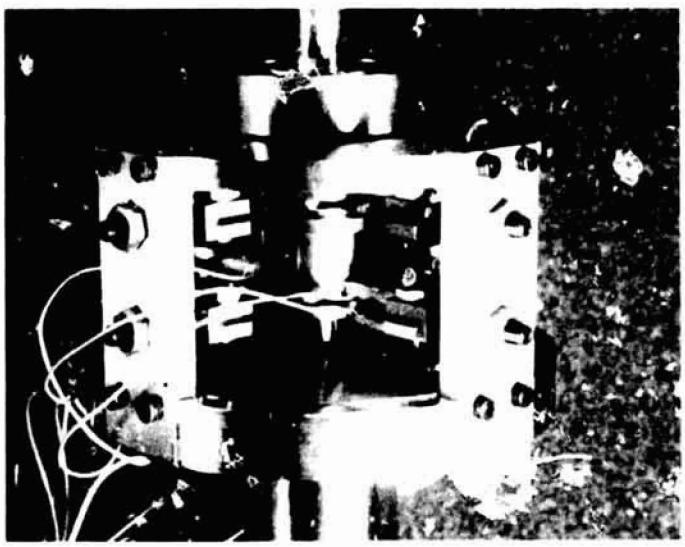

Fig. 44 Dynamometer parts and assembly

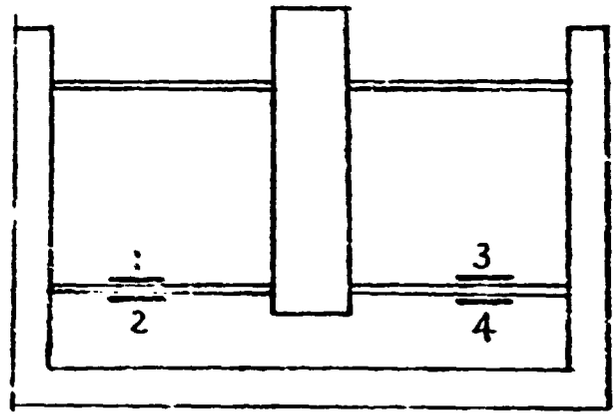

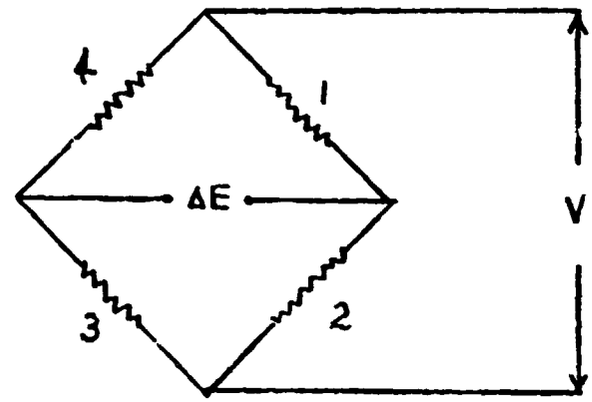

ig. 45 strain gage bridge

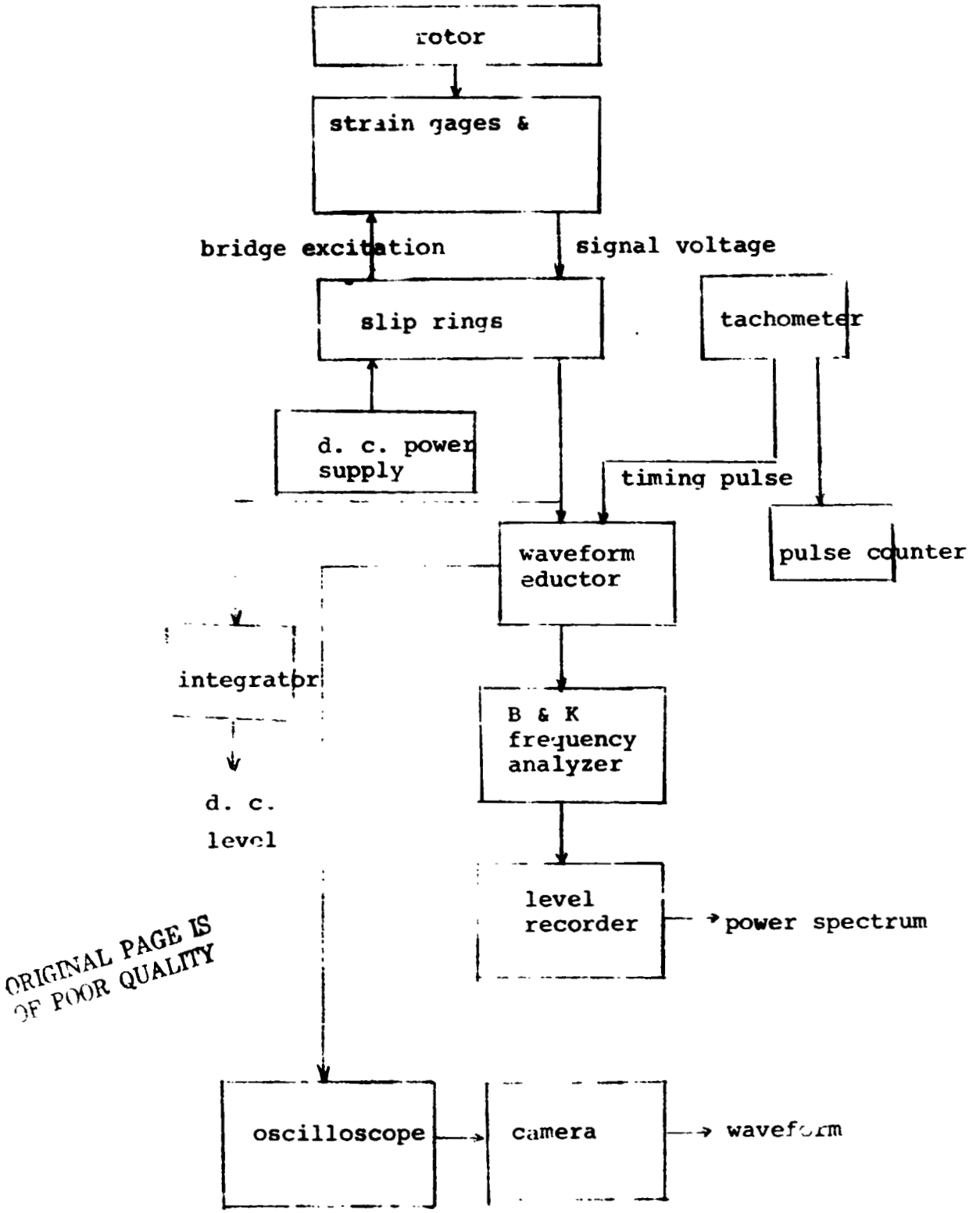

Fig. 46 measurement system block diagram

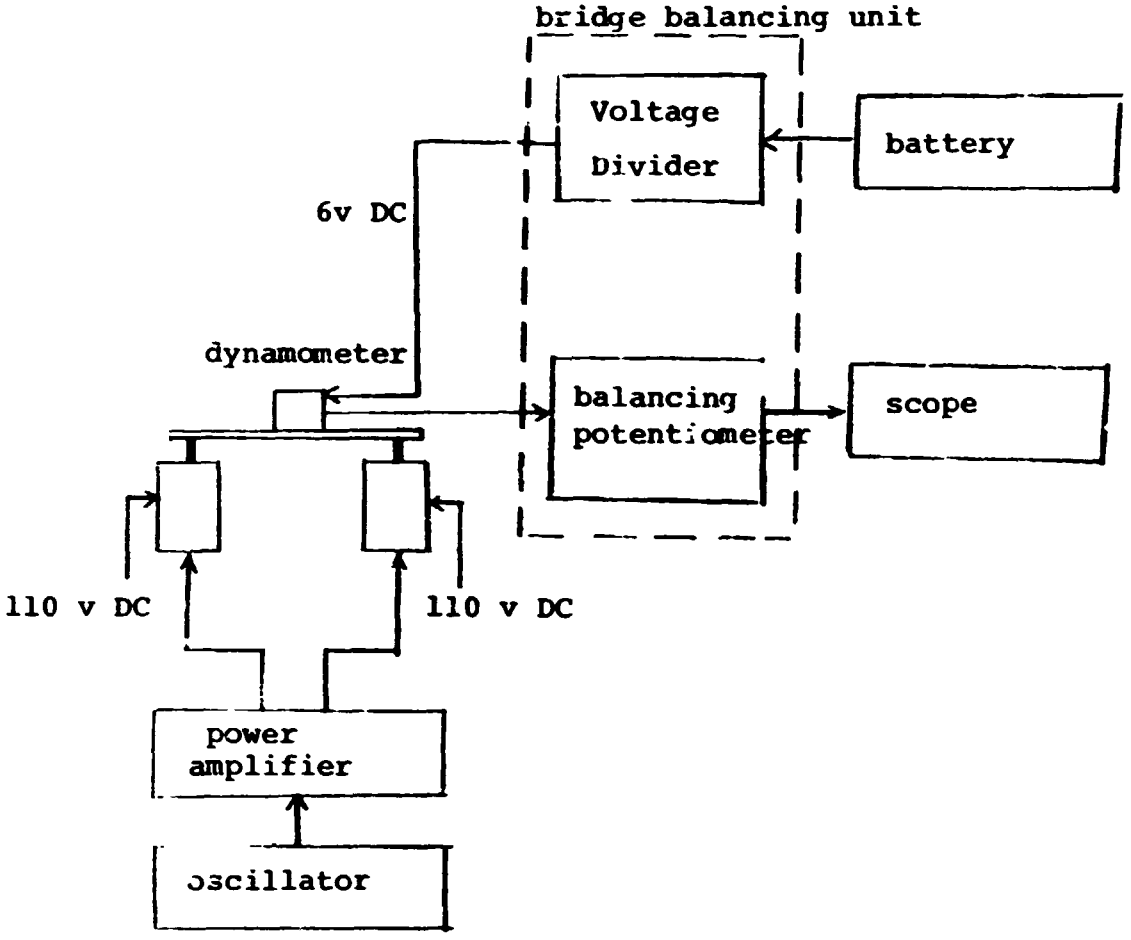

Fig 47 The arrangement for measuring natural frequency of dynamometer

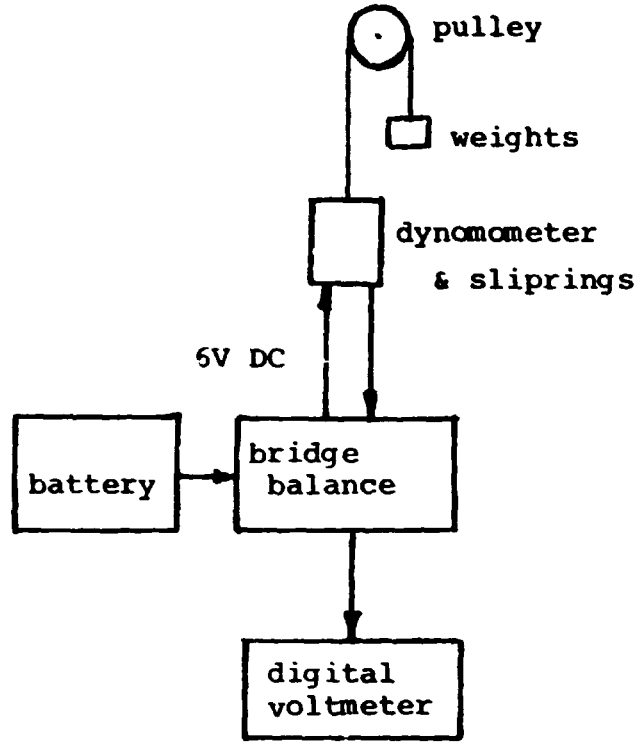

Figure 48 Block Diagram of Dynomometer Calibration Setup

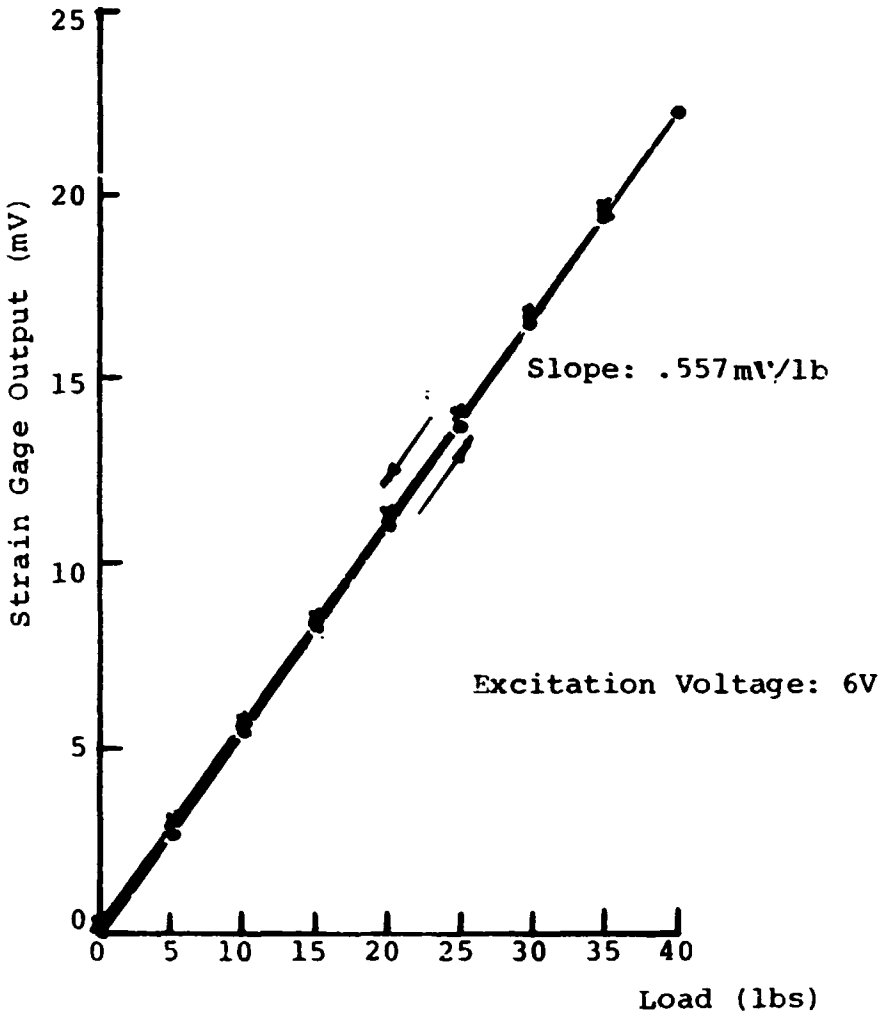

Figure 49 Static Calibration Curve for the Dynomometer: Strain Gage Output vs. Applied Load

TABLE OF CONTENTS